The Development of Photonic Crystal Optics and Wide-field Raman Imaging Spectrometers for Trace Explosive Detection

by

Kyle T. Hufziger

B.S., Chemistry, Villanova University, 2012

Submitted to the Graduate Faculty of

the Dietrich School of Arts and Sciences in partial fulfillment

of the requirements of the degree of

Doctor of Philosophy

University of Pittsburgh

2019

UNIVERSITY OF PITTSBURGH

DIETRICH SCHOOL OF ARTS AND SCIENCES

This dissertation was presented

by

Kyle T. Hufziger

It was defended on

March 14th, 2019

and approved by

Dr. Sean Garrett-Roe, Associate Professor, Department of Chemistry, University of Pittsburgh

Dr. David Waldeck, Professor, Department of Chemistry, University of Pittsburgh

Dr. Sachin Velankar, Associate Professor, Mechanical Engineering and Materials Science, University of Pittsburgh

Dissertation Advisor: Dr. Sanford Asher, Distinguished Professor of Chemistry, Department of Chemistry, University of Pittsburgh

The Development of Photonic Crystal Optics and Wide-field Raman Imaging Spectrometers for Trace Explosive Detection

Kyle T. Hufziger, PhD

University of Pittsburgh, 2019

There is currently an urgent, unmet need for sensitive and specific instruments that can detect trace explosive residues from a distance, allowing suspicious objects to be remotely screened for the presence of explosives before the approach of law enforcement or military personnel. UV resonance Raman spectroscopy is a powerful technique that enables precise determination of the chemical identity of samples excited by monochromatic light. Furthermore, Raman spectroscopy is well suited for standoff detection, which makes this technique ideal as a method to screen for trace quantities of explosives from a distance. However, UV spectroscopies are hampered by the lack of commercially available optical devices that function in the deep UV spectral region from 200-300 nm due to the fact that many materials absorb light strongly at these wavelengths. Building deep UV spectroscopic instrumentation capable of standoff trace explosive detection therefore requires the development of optics that function in this spectral region.

In this work, we developed deep UV photonic crystal optical devices and deep UV resonance Raman imaging spectrometers based on those devices for standoff trace explosive detection purposes. We first developed a novel, proof of concept wide-field Raman imaging spectrometer in the visible spectral region to demonstrate the utility of photonic crystals as wide-field Raman imaging optics. Using knowledge gained during those studies, we then developed a deep UV wide-field Raman imaging spectrometer that utilized 229 nm excitation and a deep UV

diffracting photonic crystal to image, detect, and chemically differentiate 10 μg/cm^2 quantities of solid explosive at 2.3 m standoff. These studies demonstrated the feasibility and promise of deep UV wide-field imaging and deep UV diffracting photonic crystal optics. Finally, we developed the first deep UV diffracting inverse opal photonic crystal to increase the mechanical durability and shelf life of photonic crystal optical devices, opening the door for the development of field usable deep UV wide-field imaging instrumentation for standoff trace explosive detection.

Table of Contents

Title Page ..... **i**
Abstract ..... **iv**
List of Figures ..... **ix**
List of Equations ..... **xiv**
Preface ..... **xv**
1.0 Chapter 1: Introduction **1**
1.1 Scope of Introduction 1
1.2 Motivation and Background 1
1.3 Raman Spectroscopy 5
1.4 Photonic Crystals 10
1.4.1 Polymer Nanoparticles 12
1.4.2 Silica Nanoparticles 14
1.4.3 Nanoparticle Interactions 16
1.4.4 Self-Assembly 20
1.4.5 Photonic Crystal Diffraction and Bragg's Law 29
1.5 Explosive Detection 35
1.5.1 Non-standoff Explosive Detection 35
1.5.2 Standoff Explosive Detection 40
1.5.3 Advantages of UV Excitation for Raman Spectroscopy 49
1.5.4 Standoff UV Raman Spectroscopy 51
1.6 Motivation for Deep UV Diffracting Photonic Crystal Development 55
2.0 Chapter 2: Raman Hyperspectral Imaging Spectrometer Utilizing Crystalline Colloidal Array Photonic Crystal Diffraction **59**
2.1 Introduction 59
2.2 Experimental 61
2.2.1 Synthesis of Monodisperse Polystyrene Nanoparticles 61
2.2.2 Characterization Techniques 62
2.2.3 Raman Instrumentation 63
2.3 Results and Discussion 64
2.3.1 Photonic Crystal Diffraction 64

2.3.2 Spectrometer Design 67
2.3.3 Raman Diffraction 69
2.3.4 Raman Imaging 70
2.4 Conclusion 72
2.4.1 Acknowledgements 72
3.0 Chapter 3: Ultraviolet Raman Wide-field Hyperspectral Imaging Spectrometer for Standoff Trace Explosive Detection 73
3.1 Introduction 73
3.2 Experimental 77
3.2.1 Monodisperse Silica Nanoparticle Synthesis and Functionalization 77
3.2.2 Nanoparticle and Photonic Crystal Diffraction Characterization 80
3.2.3 Trace Explosive Sample Preparation 80
3.2.4 Raman Measurements 82
3.3 Results and Discussion 83
3.3.1 Photonic Crystal Diffraction 83
3.3.2 UV Wide-Field Imaging Spectrometer Design 89
3.3.3 Raman Wide-Field Imaging 91
3.4 Conclusion 97
3.4.1 Acknowledgements 98
4.0 Chapter 4: Solid Deep Ultraviolet Diffracting Inverse Opal Photonic Crystals 99
4.1 Introduction 99
4.2 Experimental 103
4.2.1 3D Close-Packed PSNP/SiO_2 PC Self-Assembly and IO PC Formation 103
4.2.2 Nanoparticle and PC Characterization 106
4.3 Results and Fabrication 108
4.3.1 Fabrication Parameters and SEM Analysis 108
4.3.2 PC Diffraction via UV-Visible Spectroscopy 112
4.3.3 IO PC LDLS Diffraction 116
4.3.4 IO PC 229 nm Diffraction 118
4.4 Conclusion 124
4.4.1 Acknowledgements 124
4.5 Supporting Information 125
4.5.1 Polystyrene Nanosphere Synthesis 125
4.5.2 Calculation of Photonic Crystal Parameters 131

5.0 Chapter 5: Summary of the Development of Photonic Crystal Optics and Wide-field Raman Imaging Spectrometers for Trace Explosive Detection 133

Bibliography 137

List of Figures

Figure 1.1 – Number of terrorist attacks world-wide per year, where the red portion of each column indicates the number of attacks carried out using explosives, bombs, and dynamites. Figure data is compiled from the Global Terrorism Database.[3] 2

Figure 1.2 – Energy level diagram depicting Rayleigh scattering, Stokes Raman scattering, and resonance Stokes Raman scattering, where the solid lines indicate real vibronic states of the molecule and the dotted lines indicate virtual states. 6

Figure 1.3 – Deep UV absorption spectrum of several explosive molecules of interest, including PETN, HMX, TNT, and RDX, dissolved in CH_3CN, as well as NH_4NO_3 (AN) dissolved in water. Figure adapted from Tuschel *et al*.[26] 9

Figure 1.4 – Non-close packed FCC unit cell of spheres (red), looking along the (111) plane normal. A blue, semi-transparent cube whose corners intersect with the centers of the spheres at the corners of the unit cell is included as an aide for the eye. 23

Figure 1.5 – Close packed FCC unit cell of spheres, looking along the (111) plane normal..... 24

Figure 1.6 – Side-on schematic of a vertical deposition process, where a hydrophilic solid substrate is dipped into a solution (blue) containing nanoparticles (grey circles). Relatively rapid evaporation from the meniscus results in a convective flow of solvent and nanoparticles from the bulk solution into the meniscus, forming a close packed FCC array. Figure adapted from Hufziger *et al*.[107] 25

Figure 1.7 – Schematic of the immersion capillary force. Nanoparticles that are closely confined between a substrate and a solvent (blue)-gas interface will deform the solvent surface, producing a strong attractive immersion capillary force that draws adjacent particles together. Figure adapted from Prevo *et al*.[101] 26

Figure 1.8 – Inverse close-packed FCC structure looking along the (111) plane normal, where the interstices in Figure 1.5 have been completely filled with a polymer (blue) and the nanospheres have been removed, leaving behind empty void space. Sphere to sphere contact excludes monomer during the polymerization process, resulting in small "windows" between spherical air-voids left behind after nanoparticle removal, which are visible as small circles in this schematic. 28

Figure 1.9 – Non-close-packed FCC unit cell of red spheres. A (111) Miller index lattice plane originating in this unit cell, in addition to a (111) plane originating from an above FCC cell (not shown), are depicted as the left and right purple triangles, respectively. The origin in this case is the sphere in the lower back left corner of the unit cell, and the three reference axis run along the edges of the cubic unit cell outwards from the origin. 30

Figure 1.10 – Depiction of the Bragg condition, where the lattice planes, such as the (111) planes shown in Figure 1.9, are depicted as blue lines separated by the distance d_{hkl}. Light, depicted by red arrows, is incident from the left and is diffracted by these lattice planes towards the right. Figure adapted from Kittel.[127] 32

Figure 1.11 – Photograph of a non-close-packed FCC photonic crystal composed of highly charged ~100 nm diameter polystyrene nanospheres injected between two fused silica plates, showing bright green (111) Bragg diffraction. 33

Figure 1.12 – (a) Example of an IMS measurement. First, molecules are introduced into the reaction region to be ionized before being introduced into the drift region to be separated by mass, charge, and collision cross section before being detected. (b) Example spectra of several explosives detected by an ion mobility spectrometer. Figure adapted from Eiceman *et al*. and Hilton *et al*.[144, 145] 37

Figure 1.13 – (a) Schematic of the Fido fluorescence quenching explosive sensor originally demonstrated in 2001. (b) Handheld Fido 4A fluorescence quenching instrument. Figure adapted from Cumming *et al*. and Swager *et al*.[4, 158] 39

Figure 1.14 – Cart mounted standoff LIBS instrument utilized for explosive detection. A Nd:YAG laser produced 350 mJ pulses of 1064 nm light to excite samples including TNT, RDX, and C-4 placed on a car door at 30 m standoff. Figure adapted from Lopez-Moreno *et al*.[171] 41

Figure 1.15 – 27 m standoff Raman spectra of RDX with a (a) 99 ms and (b) 100 μs ICCD gate width. The spectra show strong Hg lines from fluorescent ceiling lamps that appear with longer gate widths. Figure adapted from Carter *et al*.[25] 44

Figure 1.16 – (a) White light image of solid 5 mm diameter sulfur, DNT, NH_4NO_3, and TNT samples from left to right. (b) Raman spectral image of the samples depicted at left indicating the sum of the measured Raman band intensities. Color indicates relative Raman intensity from low (blue) to high (red). Sulfur scatters Raman light much more intensely than the three other samples, resulting in a bright red feature. Figure adapted from Östmark *et al*.[14] 45

Figure 1.17 – Spatially offset Raman spectra of solid $NaClO_3$ held within a 1.5 mm thick HDPE container at 12 m standoff. Neat $NaClO_3$ and HDPE are depicted in the top and bottom spectra, respectively. The ratio of $NaClO_3$ to HDPE Raman bands increase with the spatial offset between the collection optic and the exciting beam. Figure adapted from Zachhuber *et al*.[185] 46

Figure 1.18 – Standoff visible Raman spectrometer constructed by Misra *et al*. pointed at samples 120 m away. Figure adapted from Misra *et al*.[24] 48

Figure 1.19 – Normalized Raman intensity for the (a) 1044 cm^{-1} band of solid NH_4NO_3 and (b) 1620 cm^{-1} band of solid TNT as a function of sample thickness and excitation wavelength. Figure adapted from Fountain *et al*.[33] 50

Figure 1.20 – 2.2 m standoff 213 nm UVRR spectra of different amounts of solid $NaNO_3$ powder. Spectra were accumulated for 60 sec and the irradiance is ~30 mW/cm^2. The smoothed (Savitzky-Golay) and raw spectra are overlaid. Figure adapted from Bykov *et al*.[197] 54

Figure 1.21 – 2.2 m standoff 213 nm UVRR spectra of aqueous NH_4NO_3 solutions at different concentrations in a 1 cm path length cuvette. Spectra were accumulated for 10 sec. Figure adapted from Bykov *et al*.[197] 55

Figure 2.1 – TEM micrograph of monodisperse 102.7 ± 4.1 nm diameter polystyrene nanospheres. Scale bar represents 300 nm. 64

Figure 2.2 – Incidence angle dependence of diffraction by a 102.7 nm diameter polystyrene particle photonic crystal measured using an absorption spectrometer. Incidence angles measured relative to the input plate. 66

Figure 2.3 – Diagram of the Raman imaging spectrometer where an Argon laser produces 488 nm light. LLF is a 488 nm laser-line filter, T is the Teflon sample, L1 is a plano convex collection lens, A1 is a 1.5 cm diameter aperture, LPF is a long-pass edge filter used to remove the Rayleigh scattered light, CCA is our crystalline colloidal array photonic crystal mounted on a rotation stage, M1 is a rotatable planar mirror, and M2 is a planar mirror used to direct the diffracted light towards either of the plano convex lenses, L2 or L3. CCD is the Pylon CCD camera and OS is the Ocean Optics spectrometer. The lens focal lengths are $f_{L1} = f_{L2} = 10$ cm, and $f_{L3} = 30$ cm. 68

Figure 2.4 – (a) Teflon Raman spectrum measured with the Raman microscope. (b) Teflon Raman spectrum of light diffracted by the photonic crystal measured by the Ocean Optics spectrometer. Both samples were excited with 488 nm light. 69

Figure 2.5 – (a) Photograph of a Teflon surface with a ~1 mm diameter NaCl filled depression. (b) Raman spectral image of 1200 – 1400 cm^{-1} light diffracted by the photonic crystal showing the NaCl depression. Accumulation time for the Raman image was 5 seconds. 71

Figure 3.1 – Transmission electron micrograph of highly charged 35.5 ± 2.9 nm silica nanoparticles. Scale bar denotes 150 nm. 79

Figure 3.2 – 35.5 ± 2.9 nm silica nanoparticle PC transmission measured using an absorption spectrometer at various PC rotational angles. 85

Figure 3.3 – Photograph of the PC cell. Highly charged, monodisperse nanoparticles are injected through the back plate into a cavity formed by a melted Parafilm spacer, where the particles self-assemble to form the deep UV diffracting PC. 86

Figure 3.4 – (a) Diffraction power of the 229 nm laser beam diffracted by PC in panel (b) as a function of laser glancing angle within the PC dispersion. Incident beam power is ~150 μW. A Gaussian fit is depicted in blue. (b) PC transmission measured in the absorption spectrometer at a 68° glancing angle measured in air (74° within PC after refraction). 88

Figure 3.5 – Schematic of the standoff deep UV hyperspectral Raman imaging spectrometer. NF, 229 nm notch filter; A1, aperture; L1, plano-convex collimating lens; PC, UV diffracting photonic crystal mounted on a rotational stage, CMOS, color camera with 35 mm lens; M, planar mirror mounted on a rotational stage connected to a translational stage; L2, plano-convex focusing lens mounted on a translational stage; A2, aperture; UBF, UV bandpass filter; CCD, PIXIS detector. $f_{L1} = 205$ mm and $f_{L2} = 95$ mm at 229 nm. 90

Figure 3.6 – (a) CMOS image of the 120 μg (920 μg/cm^2) PETN (top) and 120 μg (760 μg/cm^2) AN (bottom) drop-cast films on an aluminum plate at a 2.3 m standoff distance. (b) 229 nm Raman spectra of solid PETN (top, red) and solid AN (bottom, blue). A ~1 nm FWHM diffracted spectral bandwidth at a 16.5° PC angle is depicted by the blue shading. (c and d) Raman images of the trace explosive sample shown in (a) at a 16.5° PC angle after 30 sec and 2 min accumulations, respectively. (e) Expanded 30x microscope image of the sample in panel (a) before irradiation. Scale bar represents 1 mm. (f) 229 nm Raman spectra of solid PETN (top) and solid AN (bottom). A ~1 nm FWHM diffracted spectral bandwidth at a 14° PC angle is depicted

by the red shading. (g and h) Raman images of the trace explosives shown in (a) at a 14° PC angle after 30 sec and 2 min accumulations, respectively. Both rotational angles of incidence are measured in air. 30 sec and 2 min accumulations utilize 8 x 8 and 6 x 6 pixel binning, respectively..... 92

Figure 3.7 – (a, d, and g) CMOS images of 250 μg/cm^2, 100 μg/cm^2, and 10 μg/cm^2 of inkjet printed PETN on smooth aluminum substrates, respectively, at a 2.3 m standoff distance. Red outlines indicate the area illuminated with 229 nm excitation. (b, e, and h) Raman images of the trace explosives shown in panels (a, d, and g) at a 13° PC angle at 30 sec (8 × 8 binning) of accumulation. (c, f, and i) Raman images of the trace explosives shown in panels (a, d, and g), at a PC angle of 13° at 2 min (6 × 6 binning) of accumulation. The PC used here differs from that used in Figure 3.6. At a 13° PC angle, the PC diffracts a Raman spectral region centered at the 1289 cm^{-1} PETN NO_2 symmetric stretch..... 95

Figure 3.8 – (a, d, and g) CMOS images of 250 μg/cm^2, 100 μg/cm^2, and 10 μg/cm^2 of inkjet printed AN on smooth aluminum substrates, respectively, at a 2.3 m standoff distance. Red outlines indicate the areas illuminated with 229 nm excitation. (b, e, and h) Raman images of the trace explosives shown in panels (a, d, and g), at a 16° PC angle at 30 sec (8 × 8 binning) of accumulation. (c, f, and i) Raman images of the trace explosives shown in panels (a, d, and g), at a 16° PC angle at 2 min (6 × 6 binning) accumulations. At a 16° PC angle, the PC diffracts a Raman spectral region centered at the 1044 cm^{-1} AN NO_3^- symmetric stretch. The diffracting PC used here is identical to that used in Figure 3.7..... 96

Figure 4.1 – Photograph, micrograph, and diffraction results obtained from a deep UV diffracting inverse opal photonic crystal..... 101

Figure 4.2 – Schematic of the deep UV diffracting IO PC fabrication method. (A) A clean, hydrophilic fused silica substrate is dipped into a solution, depicted in blue, containing PSNPs, TEOS, ethanol, HCl, and water in a 20 mL vial. The vial is then placed in a hot oven. (B) Self-assembly of the 3D close-packed FCC PSNP structure onto the fused silica substrate proceeds via evaporation driven vertical deposition over several days while TEOS condenses in the PSNP interstices to form an SiO_2 matrix. (C) After drying, the PSNPs are embedded in an SiO_2 matrix that is attached to the fused silica substrate. (D) Piranha solution is used to remove the PSNPs while leaving the SiO_2 intact, yielding an FCC array of voids in the SiO_2 matrix. 104

Figure 4.3 – Photograph and SEM micrographs all originating from the same IO PC. (A) Photograph of an IO PC after piranha solution treatment to remove PSNPs. Arrow indicates strongly diffracting region. (B–D) SEM micrographs of the strongly diffracting region of the IO PC shown in panel A. Each micrograph axis orientation is the same as shown in panel A. (E) SEM micrograph of the same IO PC sample tilted 45°, showing the inner structure of a delaminated region at the edge of the fused silica substrate. SEM micrographs of a similar PSNP/SiO_2 PC sample prior to sphere removal are shown in Figure 4.9..... 111

Figure 4.4 – Absorbance spectra measured using the absorption spectrometer of the PC shown in Figure 4.3. (A) PSNP/SiO_2 PC absorbance spectra measured at five incident angles, showing FCC (111) diffraction at ~336 nm and strong PSNP absorption below 275 nm. (B) Absorbance spectra of the same PC at the same incident angles after piranha treatment, yielding an IO PC. The linear fit of λ_{max}^2 versus $\sin^2(\theta_i)$ (inset plots) enables experimental determination of d_{111} and n_{avg}. Listed angles are the incident light angles in air measured from the PC surface normal (θ_i)..... 114

Figure 4.5 – LDLS diffraction spectrum of the IO PC shown in Figure 4.3 at a 15° incidence angle in air. The primary FCC (111) diffraction peak occurs at ~241 nm. Also evident are a number of Fabry-Perot interference fringes, labeled by arrows. Inset: Fabry-Perot fringe plot. $K = (2n_{avg}\cos(\theta_i)(\lambda_1-\lambda_P)/(\lambda_1\lambda_P))\times10^4$ where $n_{avg} = 1.13$, $\theta_i = 15°$, λ_1 is the wavelength of the longest wavelength interference fringe detectable, in this case at 370 nm, and λ_P is the wavelength of subsequent fringes at shorter wavelengths. 117

Figure 4.6 – (A) Schematic of the 229 nm diffraction experiment layout. (B) Intensity of 229 nm diffraction by the IO PC shown in Figure 4.3 as a function of Bragg glancing angle, θ, within the IO PC. A Gaussian fit is shown in red. 119

Figure 4.7 – (A) Picture of the 229 nm diffracted beam shape on a luminescent paper viewing screen for the IO PC at a 26.5° IO PC incident angle in air, corresponding to the Bragg condition for 229 nm light. (B) Height map of the strongly diffracting region of the IO PC shown in Figure 4.3 measured using an optical profilometer. The color-bar depicts the height of surface features, where red and blue map colors indicate raised features and depressions, respectively. 121

Figure 4.8 – Transmission electron micrograph of 138.3 ± 3.1 nm diameter polystyrene nanoparticles..... 125

Figure 4.9 – Scanning electron micrographs of an as-fabricated PSNP/SiO_2 PC before nanoparticle removal at high (A) and low (B) magnification. This PC was fabricated under identical conditions to the IO PC depicted in Figure 4.3..... 127

Figure 4.10 – Photographs and absorbance spectra measured using an absorption spectrometer of a PSNP/SiO_2 PC at normal incidence before (black) and after (red) THF treatment. This PC was fabricated under identical conditions to the IO PC depicted in Figure 4.3. This sample was fully immersed in 21.0 mL THF (Fisher Chemical T397) and placed on a mixer for 2 days, replacing the solvent after 1 day, before drying in air. After THF treatment, PC FCC (111) diffraction, indicated by the red arrows, blueshifts slightly but becomes extremely weak, likely due to heterogeneous and incomplete removal of PSNPs from the SiO_2 matrix by THF. 128

Figure 4.11 – Absorbance spectra of an IO PC fabricated using 114.9 ± 3.4 nm diameter polystyrene nanoparticles, showing strong FCC (111) diffraction at 211 nm at normal incidence. Listed angles are measured in air from the IO PC surface normal. 129

Figure 4.12 – Scanning electron micrograph of the right edge of the strongly diffracting region indicated by the arrow of the IO PC sample shown in Figure 4.3A, tilted at a 45° angle. The banding features near the slide edge are visible as sweeping curves which terminate at the microscope slide edge, visible at the bottom of the micrograph. 130

Figure 4.13 – Absorbance spectra of the IO PC depicted in Figure 4.3 at normal incidence shortly after inversion (red) and after the sample was extensively handled and characterized (black). The times listed in the figure denote the number of days that had elapsed between the end of fabrication and the day of spectral collection. The small differences in λ_{max} attenuations and peak positions between the two measurements are likely due to minute positioning and angle differences of the IO PC sample within the cavity of the absorption spectrometer. 131

List of Equations

Equation 1.1 32

Equation 2.1 64

Equation 3.1 83

Equation 3.2 87

Equation 3.3 87

Equation 3.4 87

Equation 3.5 93

Equation 3.6 93

Equation 4.1 112

Equation 4.2 131

Preface

My success as a graduate student was inextricably linked to the huge amount of support, encouragement, and tutelage I received during my graduate career. This work towards my doctorate would not have been possible without my network of family, friends, advisors, professors, and supporters. I would like to thank Dr. Sanford Asher for being my advisor, both in research and in life, throughout my career here at the University of Pittsburgh. I am fortunate to have had such an understanding, supportive, knowledgeable, and flexible advisor during my studies here in the Department of Chemistry. Most importantly, his encouragement and confidence in my abilities, research, and accomplishments helped me to become the scientist I am today. My growth as a scientist as I worked towards my PhD under the auspices of Dr. Asher was truly shocking in its extent, and I am grateful for his help and for the opportunity to work in the Asher Lab.

I would also like to thank my many labmates, friends, colleagues, and coworkers that I had the pleasure of interacting with throughout my time here in Pittsburgh. I would like to specifically thank, in no particular order, my labmates Ryan Jakubek, Dr. Alyssa Zrimsek, Dr. Sergei Bykov, Ryan Roppel, Kyeongwoo Jang, Natasha Smith, Dr. David Punihaole, Lily (Tsung-Yu) Wu, and Dr. Zhenmin Hong.

I would first like to thank Ryan Jakubek for being such a great friend, for the numerous insightful discussions we've had on theory of all sorts, for being so professional and reliable, and for working with me to repair and align numerous pieces of equipment, spectroscopic and otherwise, throughout the lab. I would like to thank Alyssa for being such an excellent mentor, collaborator, and friend. I am tremendously appreciative of Alyssa's guidance and advice on any

problem, and for her integral contribution towards my last dissertation project. I'd especially like to thank Sergei for his essential expertise and guidance in teaching me the fundamentals of true laboratory spectroscopy, and for collaborating with me on our papers and various other scientific ideas throughout the years. I thank Natasha for being such a good friend, for supporting me throughout my research, for her boundless energy and enthusiasm, and her steadfast belief that scientific research can make the world a better place. I'd like to thank Dave for his friendship, for holding the group to such a high standard of professionalism, and for demanding the best out of all of us. I thank Lily for being such a positive influence on group chemistry, for being a great friend, and for motivating all of us to eat better and hit the gym.

I would like to thank Sharon Mansfield for being one of the friendliest people I have ever met and for being so incredibly helpful to all of us; achieving a PhD would be at least an order of magnitude more difficult without her help. I would also like to thank Dr. David Waldeck, Dr. Sean Garrett-Roe, and Dr. Sachin Velankar for serving on my comprehensive and dissertation committees and for asking the tough questions that taught me how to give a good technical talk.

I am enormously grateful for and thank all of the facilities and their experts at the University of Pittsburgh. I thank everyone at the Machine Shop, especially Tom Gasmire, Jeff Tomaszewski, and Shawn Artman, for teaching me how to machine, for their guidance and friendship, and for making numerous, invaluable parts for me that I installed into my spectrometers over the years. I also thank Tom Harper who runs the Department of Biological Sciences electron microscopy facility for being so helpful with his knowledge of electron microscopes, which were an integral part of my dissertation work. I'd like to thank University of Pittsburgh's scientific glassblower Lori Neu for fixing our scientific glassware and for fabricating a large number of

sample substrates for me during the latter half of my PhD, which were critical to the success of my final project.

I am also extremely appreciative of my parents, Paul and Evelyn Hufziger, and my siblings, Daniel, Adam, and Mary, for their continuous support and guidance during these years of graduate research, and for their extensive interest in my work and my life. Most of all, I'd like to thank my best friend and partner in all things Katie Johnston. Her love, support, friendship, scientific guidance, and partnership was integral to help me get through the longest, hardest challenge in my life to date. We met at Villanova University as lab partners on our first day of undergraduate inorganic chemistry lab. I would never have guessed that my life would become so thoroughly intertwined with Katie's, but I am thankful that it did. I would also like to thank Dr. Jared Paul, who as a close friend and as my undergraduate research advisor played an essential role in the development of my career and of my love of chemistry. I am grateful for all of the family, friends, and mentors I have had the immense pleasure of interacting with during graduate school.

1.0 Chapter 1: Introduction

1.1 Scope of Introduction

This introduction covers a diverse range of topics relevant to understanding the utility and characteristics of deep UV excited resonance Raman spectroscopy and photonic crystal optical devices in addition to a review of the state of the art in explosive detection. First, we describe the background and motivation behind our goal to develop better trace explosive detection techniques. Next, we describe Raman spectroscopy and the desire to use deep UV excitation to improve its sensitivity. We then describe the fabrication and use of photonic crystal optics, particularly as they relate to wide-field imaging spectroscopy. Finally, we thoroughly examine the field of explosive detection techniques in general, describing the state of the art in both contact and standoff explosive detection methodologies, with a focus on the recent use of Raman spectroscopy for this purpose.

1.2 Motivation and Background

Better tools are needed to safeguard the public against terrorist attacks. The last decade has seen a significant rise in both the total number of terrorist attacks as well as the number of attacks utilizing explosive devices (Figure 1.1), peaking at nearly ~9500 attacks utilizing explosives across the world in 2014. As the number of attacks has increased over the last decade, significant interest has grown in preventing terrorist attacks via screening methods.[1] Numerous

analytical methodologies and commercial devices have been developed to screen objects, landscapes, and people to detect the presence of explosives, such as concealed improvised explosive devices (IEDs) or buried landmines.[2]

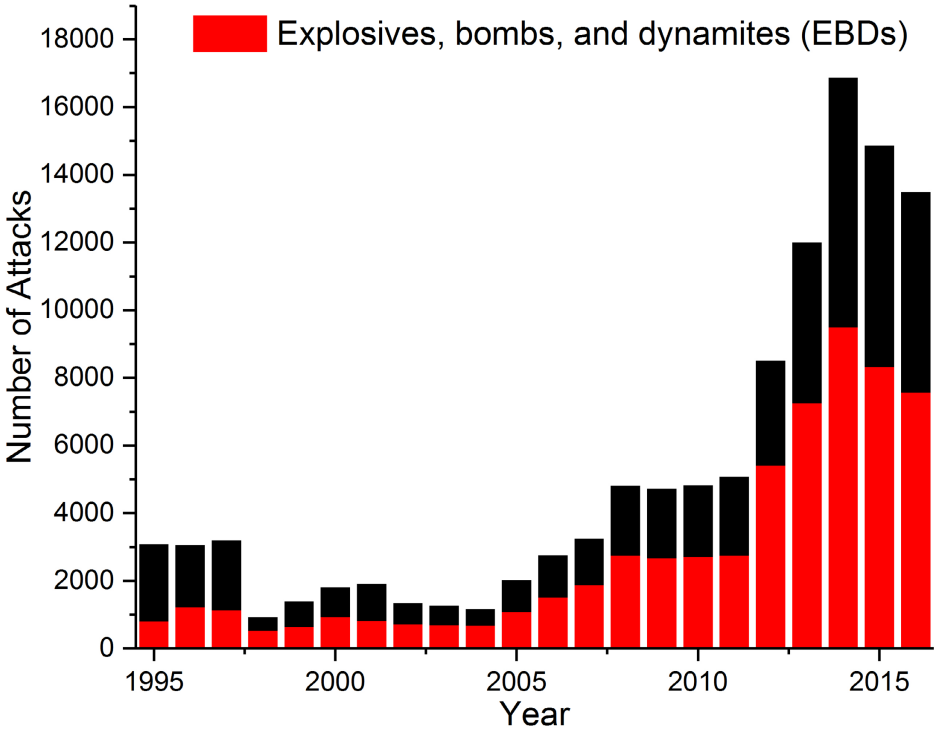

Figure 1.1 – Number of terrorist attacks world-wide per year, where the red portion of each column indicates the number of attacks carried out using explosives, bombs, and dynamites. Figure data is compiled from the Global Terrorism Database.[3]

Towards this goal, a number of techniques have been specifically developed to detect and analyze explosives present at trace levels. Trace detection techniques are largely aimed towards detecting minute quantities of explosive transferred to surfaces off of the hands of people who recently handled explosives or to sense gaseous species present in the atmosphere around hidden bulk explosives.[4, 5] Detecting trace explosive residues transferred onto a surface is highly desirable for security screening purposes.[5-7] For example, a device that could quickly and definitively detect

solid explosive micro-particles transferred from a contaminated hand onto a package or car door handle could be used to screen packages at mail facilities or vehicles entering a military checkpoint. Devices sensitive enough to detect explosives at these levels could be used to signal to an operator that a threat is present that requires caution and further screening.

Although there are several technologies that are sensitive enough to detect explosives at trace levels, such as ion mobility spectrometers used to screen passengers at airports, currently used detection schemes are limited by the necessity that an operator or instrument directly physically interact with the surface or object to be sampled.[8, 9] Screening objects via direct interaction is relatively dangerous, requiring an operator, canine, robot, or instrument to be in close proximity with the sample, which could contain hidden bulk explosive, in order to physically swab, spray, or "sniff" it.[9] Ideally, trace explosive detection methods would be capable of screening objects from a sufficiently safe distance of meters or more, to keep operators and instrumentation away from explosive hazards. Furthermore, the ideal trace detection technique should be sensitive, fast, and specific in order to precisely identify the chemistry of any present threat molecules.

At this time, the ideal standoff trace explosive detection device does not exist. However, our research laboratory and numerous other laboratories across the world have made significant progress in the development of standoff detection instrumentation and methodologies over the past two decades. Current spectroscopic methods, discussed in detail in Chapter 1.5, can detect and identify bulk explosives from >100 meters away, or detect trace $\mu g/cm^2$ quantities of solid explosives from several meters away.

Spectroscopic analysis is the ideal way to definitively identify the chemistry of trace amounts of materials on a sample surface from a far distance. Of the numerous spectroscopic techniques used for chemical analysis, Raman spectroscopy is particularly well suited for

explosive detection because the collected Raman spectra act as unique molecular fingerprints, enabling definitive identification of molecules illuminated by the laser beam used to produce to Raman scattering.[10] Importantly, Raman spectroscopy is also well suited for standoff detection, and several groups have previously demonstrated that Raman spectra can be collected from samples placed tens to >100 meters away from the Raman instrumentation.[9] Furthermore, Raman spectra can be collected with no sample preparation, which is a significant advantage in the development of fast, field usable standoff instruments.[11]

In a typical Raman experiment, a laser is focused onto a small spot on a sample, producing Raman scattered light that is collected and analyzed with a spectrograph to determine the identity of molecules within the irradiated area. However, the laser beam can also be defocused to illuminate an arbitrarily large area of the sample surface (sometimes denoted global illumination), thereby producing Raman scattered light from a large area of the sample surface.[12] Under these conditions, specially designed wide-field imaging spectrometers can be used to analyze light scattered from the entire illuminated region simultaneously, yielding a Raman image that depicts the intensity of Raman bands as a function of sample position. Raman images therefore depict the spatial distribution and identities of molecules across the surface of the sample.

Raman wide-field imaging is appealing for the standoff screening of surfaces that may be contaminated with explosives because wide-field techniques can increase measurement signal to noise, increasing the probability of detecting trace explosive particles that may be sparsely dispersed across a broad area on the sample surface.[13] As discussed in more detail in Chapter 1.5.3, Raman measurement signal to noise can also be drastically increased by utilizing excitation in the deep UV due to resonance enhancement and due to the fact that Raman signal scales with the fourth power of the excitation laser frequency (ν^4 effect).

The key component of wide-field imaging spectrometers is the wavelength selection device that is utilized to direct only one narrow bandwidth spectral region into a camera at a time while rejecting all other wavelengths, allowing molecules on the surface of the sample to be differentiated in the collected Raman image based on their specific Raman spectra.[14] While Raman wide-field imaging spectrometers are relatively easy to construct in the visible and near infrared spectral regions due to the wide availability of wavelength selection devices, these devices do not exist in the deep UV spectral region due to material limitations which inhibit their design and implementation.[15]

The goal for this dissertation work was therefore twofold: first, to create a wavelength selection device that functions in the deep UV spectral region, and second, to use this optical device to build a deep UV wide-field Raman imaging spectrometer to detect trace quantities of explosives from a standoff distance. Over the past three decades the Asher group has extensively studied and developed photonic crystal optics, which diffract a wavelength tunable narrow bandwidth spectral region.[16] Recently, our lab invented the first photonic crystal that diffracts in the deep UV at ~240 nm, opening a new avenue for deep UV optics development.[15] In this dissertation work, we build upon our laboratory's previous work in photonic crystals and Raman spectrometer development towards the goal of advancing the state of the art in trace explosive detection.

1.3 Raman Spectroscopy

Raman spectroscopy is a technique where the frequency and intensity of light inelastically scattered by a sample are studied to gain insight into the chemical identity, local chemical environment, and molecular conformation of that sample.[17-20] In a typical Raman experiment, a

focused, monochromatic laser is used to irradiate a sample. This incident electromagnetic field drives the oscillation of electrons in the irradiated molecules, inducing oscillating dipoles in those molecules.[10] These induced oscillating molecular dipoles will then radiate light in all directions. The majority of scattered photons, defined as Rayleigh scattered photons, are elastically scattered and have the same frequency as the incident photons (Figure 1.2, left).

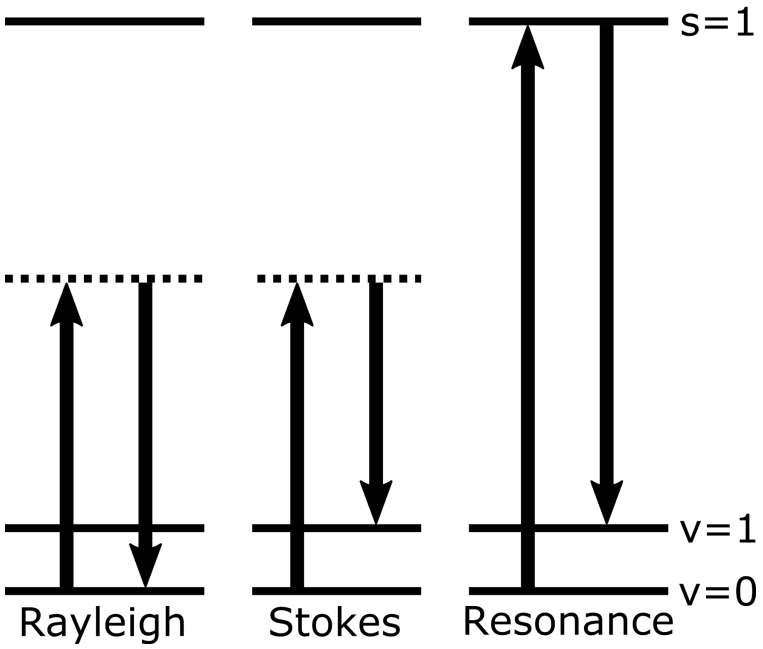

Figure 1.2 – Energy level diagram depicting Rayleigh scattering, Stokes Raman scattering, and resonance Stokes Raman scattering, where the solid lines indicate real vibronic states of the molecule and the dotted lines indicate virtual states.

A small fraction of incident photons, about 1 part in 10^6, will be inelastically Raman scattered, exchanging a quantum of energy with the scattering molecule.[17] In this case, the oscillation of molecular electrons due to nuclear vibration couples to the oscillating dipole induced by the incident electromagnetic field, scattering a photon with a different frequency than that of the incident photon.[21] After Raman scattering occurs, the irradiated molecule is left in a different

vibrational energy level. The energy difference between the incident photon and scattered photon is equal to the energy difference between the initial and final vibrational energy levels of the scattering molecule. Since most molecules are initially in the ground vibrational level according to the Boltzmann distribution, most inelastically scattered Raman photons are Stokes shifted, appearing at a lower frequency than the incident photon (Figure 1.2, middle).[22] Anti-Stokes scattering can also occur for a molecule that initially lies in a vibrational excited state, resulting in the inelastic scattering of a photon at a higher frequency than the incident photon.

Depending upon the number, identity, and bonding arrangement of atoms which make up a particular molecule there are a certain number of Raman active vibrational modes that can couple to the incident electromagnetic field, yielding Raman scattered photons at a variety of different frequencies.[23] Measuring the frequency and intensity of these Raman scattered photons yields a Raman spectrum that is unique to the chemical environment and chemical identity of the scattering molecule. Raman spectroscopy is therefore an excellent technique for determining the identity of unknown samples.[1, 24, 25] The ability to definitively determine the chemical identity of species that are irradiated by the incident laser makes Raman an appealing technique for explosive detection, however the excitation laser wavelength must be carefully chosen to enable the detection of trace quantities of any analyte, especially if they are distant from collection optics used to collect the Raman scattered light.[26]

In non-resonance (often denoted as "normal") Raman measurements, the wavelength of the incident laser is far from the wavelength of any electronic absorption bands of the analyte molecules. In this case, the number of inelastically scattered Raman photons produced by the sample is relatively low, requiring high laser powers, concentrated samples, efficient

spectrometers, and/or long accumulation times to collect a sufficient number of Raman scattered photons to produce a high signal to noise spectrum.[10]

Raman signal to noise can be dramatically increased by selecting a laser wavelength in the UV or deep UV spectral regions (<300 nm) for several reasons. First, the intensity of Raman scattering increases with a fourth power dependence on the frequency (ν) of the incident light; increasing the frequency of the incident light drastically increases the scattering strength and therefore the number of Raman scattered photons.[27, 28] In addition to the ν^4 dependence, if the frequency of the incident laser is close to the frequency of any electronic absorption bands of the sample, Raman scattering intensity can be increased by up to 10^6 through resonance Raman enhancement.[23] In resonance Raman, because the frequency of the incident light is chosen to coincide with the frequency of an electronic absorption band of the irradiated molecule, the Raman polarizability and therefore the magnitude of the induced oscillating dipole moment drastically increases.[21] As a result, resonance enhancement increases the Raman scattering efficiency of any Raman active vibrational modes that are coupled to the particular electronic transition in resonance with the laser excitation wavelength.[23]

Many explosive molecules absorb strongly in the deep UV spectral region at <250 nm, allowing their resonance Raman enhancement via appropriate selection of an excitation laser (Figure 1.3).[26, 29-32] The ν^4 increase in scattering strength and the resonance Raman enhancement effect significantly increases the sensitivity of Raman measurements using deep UV excitation, enabling standoff detection of trace quantities of explosives that would otherwise be nearly undetectable if longer wavelength lasers were utilized.[33]

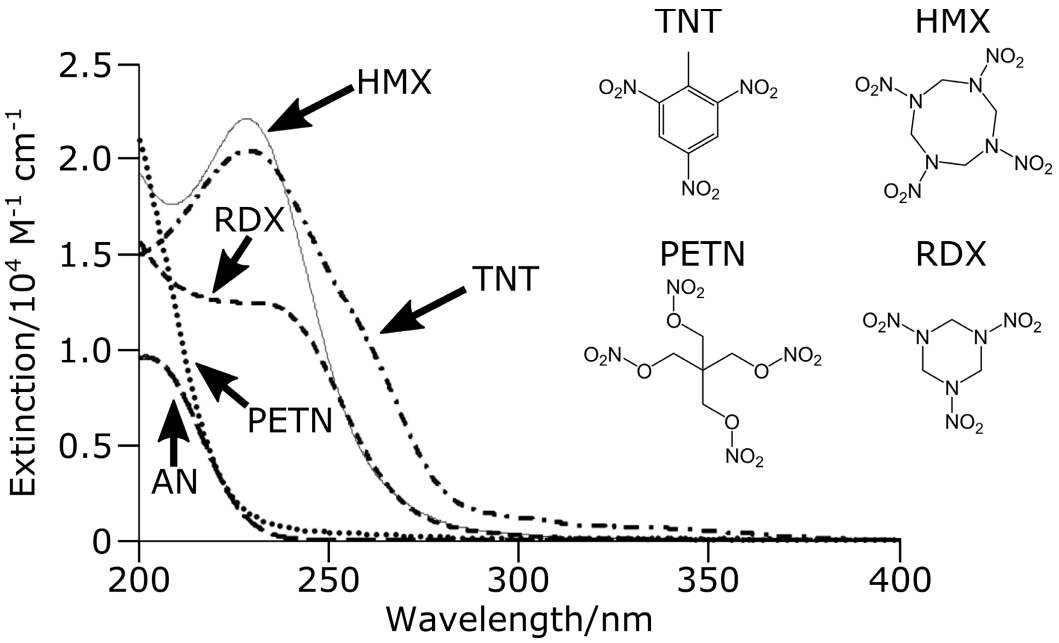

Figure 1.3 – Deep UV absorption spectrum of several explosive molecules of interest, including PETN, HMX, TNT, and RDX, dissolved in CH_3CN, as well as NH_4NO_3 (AN) dissolved in water. Figure adapted from Tuschel *et al.*[26]

While there are several significant advantages conferred by the use of deep UV excitation, as discussed in more detail in Chapter 1.5.3, designing deep UV Raman instrumentation for the standoff detection of trace explosives is challenging for several reasons. The most significant obstacle for the development of deep UV Raman wide-field imaging is that wavelength selection devices, such as liquid crystal tunable filters (LCTFs), acousto-optic tunable filters (AOTFs), and dielectric notch filters, are not available in the deep UV spectral region likely due to electronic absorption by the optical materials used in the construction of these devices.[5, 14, 34-36] Therefore, to fabricate a Raman wide-field imaging spectrometer for standoff explosive detection utilizing deep UV excitation, we needed to develop a custom wavelength selection device that utilized deep UV transparent materials. We chose to develop photonic crystals, which are discussed in detail in

the next section, to produce a wavelength selection device that functions in the deep UV spectral region.

1.4 Photonic Crystals

Photonic crystals are materials that control the propagation of light via their highly ordered periodic structures.[37] Light propagation within a photonic crystal is controlled by the particular spacing and material composition of the photonic crystal lattice, which yields a periodic modulation of the dielectric constant. Light propagating through any medium is scattered by changes in the dielectric constant in that medium.[38, 39] As light propagates through a photonic crystal it is scattered by these regularly spaced variations in dielectric constant within the structure. Depending upon the wavelength, polarization, and direction of incident light and the periodicity, shape, and materials comprising the photonic crystal, light scattered by all of these variations in the dielectric environment will constructively or destructively interfere, depending on the direction. As a result, for a particular light incident angle and photonic crystal structure, certain wavelengths of scattered light will strongly constructively interfere in particular directions, giving rise to a phenomenon known as Bragg diffraction.

The diffraction of light by photonic crystals yields a strongly iridescent color that is observed everywhere in nature, from brilliantly colored opal gemstones composed of naturally formed silica nanoparticles, to bright butterfly wings and beetle carapaces.[40-42] Photonic crystals are also extremely useful as optical devices since light propagation within and therefore through the photonic crystal can be controlled either by modifying the direction of incident light or by controlling the physical structure of the photonic crystal, both of which are realizable in the lab.

In the laboratory, photonic crystals and their wavelength tunable diffraction are utilized for a wide variety of different purposes, including as the readout method for sensors and as optical devices that reject particular wavelengths of light while allowing all other wavelengths to transmit freely.[43, 44]

The wavelength of light diffracted by the photonic crystal depends upon the initial light propagation direction, which is easily controlled in the lab by changing the angle of the photonic crystal relative to incident light. As a result, the photonic crystal can be used as an optical device to pick and diffract a particular spectral region of light that is wavelength tunable.[15, 44] In this dissertation work, we utilized the photonic crystal as an optical wavelength selection device to diffract Raman scattered photons of a particular frequency. We utilized the photonic crystal wavelength selection device to construct a new generation of Raman imaging spectrometers. Photonic crystals were crucial for the implementation of this spectrometer because they enabled diffraction of a narrow spectral region of light in the deep UV, a spectral region that is otherwise extremely difficult to construct optics for due to material absorption limitations.

To diffract light in the deep UV and visible spectral regions (200 – 700 nm light), the photonic crystal must have a lattice constant on roughly the same length scale as the wavelength of light. Photonic crystals with lattice constants on the sub-micron length scale can be fabricated via top-down methods such as direct laser writing, reactive ion etching, or other lithographic techniques.[45, 46] However, these top-down techniques can be complicated, expensive, extremely slow to fabricate large structures, and limited in their size resolution and obtainable structural geometries.[47] Alternatively, bottom-up methods can be utilized where many individual nanoparticles self-assemble to create the photonic crystal. Bottom-up self-assembly of photonic crystals is appealing because large photonic crystals, with surface areas on the order of cm^2 that

contain ~10^{12} nanoparticle structural elements, can be simply, inexpensively, and rapidly fabricated with little equipment.[47]

Nanoparticles are materials with <100 nm spatial dimensions and have been used since ancient times due to interesting and useful material properties that arise when their dimensions are reduced to this length scale.[48] Nanoparticles are widely used for photonic crystal fabrication because their size, concentration, material composition, and surface chemistry are readily tunable, enabling the resulting photonic crystal diffraction wavelength to be tuned across a broad region of the electromagnetic spectrum from the deep UV through the IR.[15, 49] For photonic crystal applications, the two most widely used nanoparticle materials are polymer and silica, although other materials, including metal oxides, have also been used.[50]

1.4.1 Polymer Nanoparticles

Polymeric nanoparticles, such as those comprised of polystyrene, poly(N-isopropylacrylamide), or poly(methyl methacrylate), are frequently utilized to create photonic crystals.[51-53] Polystyrene nanoparticles, used throughout this work, are commonly fabricated via emulsion polymerization methods, which enables the synthesis of highly monodisperse particles across a wide range of sizes.

Emulsion polymerization via free radical polymerization is a process where hydrophobic monomers, free radical initiators, and water are heated and mixed, typically in the presence of surfactants, to produce nanoparticles that have a narrow distribution in their diameters.[54, 55] For emulsion polymerization processes containing surfactants, such as those utilized in this work to produce highly charged polystyrene nanoparticles, the theoretical framework described in the late 1940s by Harkins,[56] and Smith and Ewart,[57] is typically used to describe the polymerization

process. At the start of a typical batch emulsion polymerization hydrophobic monomer, water, and surfactant are mixed, yielding an "oil in water" emulsion. In this emulsion, most of the monomer by mass is contained in large monomer droplets due to the hydrophobicity and accompanying low aqueous solubility of monomer molecules. Outside of the monomer droplets, the aqueous phase contains a small amount of dissolved monomer and a large number of micelles formed by the surfactant which contain small volumes of monomer. Surfactant coats the surface of the large monomer droplets and forms monomer filled micelles to reduce the interfacial tension that occurs due to the immiscibility of the hydrophobic monomer and aqueous phase.[55]

After forming the emulsion while heating, a water-soluble initiator is added that thermally decomposes to form free radicals. These free radicals then either react with the vinyl groups of a small amount of dissolved monomer in the aqueous phase, or migrate into and react with monomer filled micelles, in both cases forming oligoradicals.[55] Any oligoradicals in the aqueous phase continue to react with dissolved monomer via radical propagation, increasing the oligomer chain length until they become sufficiently hydrophobic such that they migrate into the interior of surfactant micelles. As radical polymerization proceeds within the micelles, a concentration gradient forms which draws monomer molecules out of the large monomer droplets and into the micelles containing the growing oligomer chains. Micelles containing oligoradicals thereby act as particle nuclei which grow by consuming monomer that diffuses out of the monomer droplet and into the micelle.[58]

As a result, as these particle nuclei grow, surfactant from the monomer droplet surfaces and from other ungrown micelles which have not absorbed free radicals is drawn towards the growing particle micelles to stabilize their expanding hydrophobic surfaces. Eventually, all radical-free micelles are consumed by this mechanism and nucleation of new particles ceases.

Migration of monomer from the monomer droplets into the growing particle nuclei continues until the monomer droplets are exhausted, yielding the final full-sized polymeric nanoparticles.

Fabrication of polymer nanoparticles via free radical emulsion polymerization enables facile covalent integration of comonomers containing vinyl functional groups into the nanoparticle structure. For example, sulfonic acid functionalized comonomers such as 3-allyloxy-2-hydroxy-1-propane sulfonic acid can be added during the initial emulsification step to produce polystyrene particles that are covalently surface functionalized with sulfonic acid groups, yielding a high negative zeta potential.[59] Polystyrene nanoparticles are very popular for the fabrication of photonic crystals that diffract visible and near IR light, however they strongly absorb light at wavelengths <275 nm, so a different nanoparticle material, such as highly transparent silica, must be used to make photonic crystal in this spectral region.

1.4.2 Silica Nanoparticles

Silica nanoparticles, which are a comprised of a -Si-O-Si- network, are also commonly used to form photonic crystals.[15, 53, 60-64] Silica nanoparticles are usually fabricated via modified and enhanced forms of the now famous method published by originally by Stöber in 1968.[65] In the original Stöber method, tetraalkyl silicate monomer was added to a solution of ammonium hydroxide and alcohol and stirred to produce monodisperse silica spheres from several hundred nanometers to several microns in diameter. Modern versions of the Stöber method typically utilize tetraethyl orthosilicate (TEOS) as the silica monomer which is added to aqueous solutions made basic via the addition of ammonium hydroxide or in some cases amino acids such as lysine and arginine.[66, 67] Upon addition to the basic aqueous solution, TEOS is hydrolyzed via nucleophilic attack by the basic species on the silicon atom to form silicic acid species $[Si(O\text{-}Et)_{4-x}(OH)_x]$

containing one or more silanol (Si-OH) functional groups.[68] After hydrolysis, two silicic acid species can condense, again via nucleophilic attack of one of the silicon atoms, to yield an -Si-O-Si- bond.

Although the Stöber method and its variations have been widely utilized for decades to produce monodisperse silica nanospheres, the exact mechanism of sphere formation is still under debate. In the most popular 'monomer addition' mechanism first described by Matsoukas *et al*., silica nanosphere formation follows a LaMer type nucleation and growth mechanism, where hydrolysis of TEOS proceeds until a critical concentration is reached where the solution becomes saturated with silicic acid species, yielding a temporally short burst of nuclei formation.[69-72] Following the fast formation of silica nanoparticle nuclei, silicic acid concentration is reduced below the critical level and TEOS hydrolysis continues to slowly generate active monomer which preferentially condenses with the nanoparticle nuclei, enabling the slow growth of monodisperse silica nanoparticles.

An 'aggregative' mechanism, first described by Bogush *et al*., has also been used to describe silica nanoparticle formation.[73, 74] In this mechanism, silica nanoparticles are hypothesized to be formed by the aggregation of many smaller, primary particles that are continuously nucleated throughout the synthesis.[75, 76] These authors theorize that these small, ~2 nm diameter primary particles are unstable in solution and quickly aggregate, resulting in the formation of larger, more stable aggregated particle assemblies. These particle assemblies grow in size via aggregation with other assemblies and with newly formed nuclei until they become sufficiently large that they resist further aggregation due to the buildup of repulsive electrostatic forces, yielding the final mature silica nanoparticles.

In an attempt to reconcile these seemingly disparate mechanistic theories, Han *et al*. studied the TEOS hydrolysis rate as a function of solution conditions.[77] These authors find that nanoparticle growth is different depending upon concentration of the basic species in solution, which controls the hydrolysis rate of TEOS. Based on their results, these authors conclude that both the aggregative and monomer addition models can be used to describe nanoparticle formation depending upon solution conditions.

After fabrication, the surfaces of silica nanoparticles can be readily functionalized using condensation chemistry to form covalent -Si-O-Si- linkages between silanol groups on the nanoparticle surface and a variety of silane coupling agents. The ability to easily functionalize silica nanoparticles post-fabrication is important because it enables the surface properties to be tuned depending upon the desired application. For example, sulfonic acid terminated coupling agents can be used to create highly negatively charged nanoparticles that resist aggregation via electrostatic repulsion, or bulky polymer chains can be attached to create nanoparticles that are sterically repulsive.

1.4.3 Nanoparticle Interactions

The ability to functionalize the surfaces of nanoparticles either during synthesis, as is the case with polymer nanoparticles synthesized via emulsion polymerization, or post-fabrication, as with silica nanoparticles, is extremely important because it enables the surface chemistry of these nanoparticles to be easily controlled. Nanoparticle surface chemistry plays a major role in the stability and utility of the nanoparticle by governing how the nanoparticle interacts with its surroundings. Careful selection of nanoparticle surface functionalization is necessary to produce a stable and functional colloidal dispersion under the specific solution conditions where the

nanoparticles will eventually be used. For example, electrostatically stabilized colloidal particles that are highly shelf stable when dispersed in electrolyte free solvent will quickly aggregate when moderate amounts of salt are added.[78]

The stability of nanoparticle dispersions depends upon the balance of attractive and repulsive forces between nanoparticles.[78, 79] Unless the nanoparticle surface produces a repulsive force which creates an energy barrier against the approach of other, nearby nanoparticles, the tendency of a dispersion will be to irreversibly aggregate and settle out of solution. The driving force for nanoparticle aggregation is the attractive London dispersion force.[80, 81] The London dispersion force arises from the constantly fluctuating distribution of electron density about atoms. An unevenly distributed electron density about the nucleus results in a formation of a transient, varying dipole. This varying dipole produces an electric field that influences the electrons in nearby atoms, thereby inducing dipoles in those atoms. The resulting interaction of these dipoles between nearby atoms gives rise to an attractive force which draws these molecules together.

The attractive dispersion force also operates between nanoparticles and is the major cause of colloidal aggregation. Models developed by Hamaker and Lifshitz can be used to describe the attractive force between nanoparticles.[82, 83] Importantly, the dispersion force becomes stronger as inter-particle distances decrease. There is a large negative Gibbs free energy for closely spaced nanoparticles, known as the primary minimum, that arises as a result of this dispersion force.[78] Any un-stabilized particles that diffuse through solution due to Brownian motion and collide become trapped by the primary minimum. Since the depth of the primary minimum is several orders of magnitude more than the thermal energy (kT) available to the particles to overcome the attractive dispersion force, they remain in contact after collision, leading to aggregation of the colloidal dispersion.

Two strategies can be employed to provide a repulsive force to prevent aggregation and stabilize the nanoparticle dispersion. For small diameter nanoparticles and for nanoparticles that will be used in solvents containing large quantities of electrolytes, steric repulsion can be utilized.[78, 79] To sterically stabilize a nanoparticle, long polymer chains are attached to the surface either via adsorption or covalent linkage. By attaching polymers that are soluble in the dispersing solvent, and therefore do not lay flat on the surface, a thick polymer layer is formed on the surface. As polymer covered particles approach each other in solution the freedom of movement of the individual polymer chains decreases as they come into close proximity with chains on the nearby particles. Since the polymer chains of two closely spaced particles are able to sample fewer spatial configurations than if the particles were far apart, entropy is reduced upon particle approach which is thermodynamically unfavorable.[84] A thick polymer layer thereby produces steric repulsion, preventing the close approach of nearby particles. Steric repulsive forces reduce dispersion aggregation by preventing nearby particles from approaching close enough for attractive dispersion forces to become significant.

In addition to steric repulsion, electrostatic repulsion can be utilized to stabilize a nanoparticle dispersion.[78] Electrostatic stabilization of a nanoparticle dispersion arises from screened Coulombic repulsive forces between nanoparticles that form due to charges on the nanoparticle surface.[85, 86] Nanoparticle surface charge can result either from the adsorption of charged species from solution onto the nanoparticle surface, or from the covalent attachment of surface ligands with ionizable groups. As a result of these processes, nanoparticles acquire a high surface charge by releasing counterions of opposite charge into solution. The charges that coat the nanoparticle surface generate an electric field that attracts counterions of opposite charge, forming an electric double layer around the nanoparticle.[87] Electric double layer interaction between two

like-charged nanoparticles results in a repulsive force between the two nanoparticles, stabilizing the nanoparticle dispersion against aggregation.

Current double layer theory is largely based on the work of Helmholtz, Gouy and Chapman, and Stern.[78, 87] The double layer is comprised of two distinct areas. In the inner layer near the nanoparticle surface, called the Stern layer, counter-ions are strongly bound to the nanoparticle surface charges. These counter-ions are considered to be immobilized on the surface and move with the particle through solution. Outside of the Stern layer is the diffuse Gouy-Chapman layer. In this layer, a balance between thermal motion and electrical attraction of the counterions with the surface charge results in a diffuse distribution of counterions that are not tightly bound to the nanoparticle surface. When the double layers of two like-charged particles overlap, the particles repel each other, providing a stabilizing force against dispersion aggregation.[88]

In the widely known Derjaguin, Landau, Verwey, and Overbeek (DLVO) theory of nanoparticle interactions, the electrical potential generated by bound surface charges falls off exponentially as a function of distance from the particle surface and is only appreciable on lengths scales on the order of the Debye length, equal to $1/\kappa$.[78] Increasing the ionic strength of the solution via the addition of electrolytes screens the electric potential generated by the nanoparticle, reducing the thickness of the double layer and the Debye length, thereby reducing the repulsive force experienced between two like-charged particles on close approach. Therefore, electrostatic stabilization of nanoparticles is only effective in solutions with low ionic strength. In these low ionic strength solutions however, the double layer thickness can be on the order of hundreds of nanometers, which results in a high energetic barrier of several hundred kT against the close approach of nanoparticles, thereby stabilizing the nanoparticle dispersion by preventing the

approach of nearby particles to distances where the strength of the attractive dispersion force becomes significant.[78] This repulsive electrostatic force is also utilized in this work to drive the self-assembly of nanoparticles into photonic crystals, which is discussed in detail in the next section.

1.4.4 Self-Assembly

Bottom-up photonic crystal fabrication involves the self-assembly of nanoparticles from an initially disordered state into a regularly repeating, highly ordered crystalline structure. This colloidal phase transition between liquid and crystalline states has been of continued interest for chemists since the 1960s, when it was observed that monodisperse polystyrene nanoparticles form brightly iridescent, Bragg diffracting structures under certain conditions.[85, 89, 90] Since Bragg diffraction necessitates a highly ordered structure, these colloidal dispersions were obviously undergoing a phase transition to a crystalline state.

There are multiple theories that have been developed to describe why colloidal particles undergo phase transitions into crystalline states. Some authors hypothesize that a major driving force behind colloidal phase transitions into crystalline states is entropic in origin.[47, 91-93] These authors theorize that at equilibrium, a colloidal dispersion will assume a structure that minimizes the free energy by maximizing the entropy of the particles.[92] This seemingly paradoxical result that a crystalline state has the highest entropy can be understood based on the maximum achievable volume fractions of different close packed structures. For a disordered, randomly closed packed (RCP) structure of spheres, the highest possible filled volume fraction is ~64%, at which point all particles are in direct contact with their neighbors.[94] Conversely, crystalline, highly ordered FCC

and hexagonally close packed (HCP) structures have been shown to have the highest filled volume fraction possible, at ~74%.

As the volume fraction of spherical nanoparticles approaches 64% in an RCP configuration, the nanoparticles become jammed and are locked into position via contact with their neighbors. Although the particles are disordered in this state, they are unable to move and sample other spatial configurations, which results in low "configurational entropy." However, if the nanoparticles were in an FCC or HCP lattice at this volume fraction, they would be able to move around within their lattice sites due to the more efficient packing structure, therefore yielding greater configurational entropy for particles in crystalline FCC or HCP structures rather than disordered RCP structures. The gain in configurational entropy due to the ability of the particles to move and sample additional configurations within their lattice sites is greater than the loss in entropy due to the formation of an ordered structure.[95] As a result, it is thermodynamically favorable for particles to form crystalline, ordered structures rather than disordered RCP structures.

Other authors hypothesize that electrostatic interactions are the major driving force for colloidal crystallization.[86, 96] For highly charged nanoparticles in extensively de-ionized solutions, the electric double layers formed around these nanoparticles can be large, with Debye lengths (κ^{-1}) on the order of several particle diameters. The effective size of the nanoparticles, which is a combination of the physical particle size and the size of the electrical double layer, is therefore large.[97] As a result, since these highly charged nanoparticles are confined at relatively close contact by the walls of a container, they readily self-assemble to form non-close packed FCC colloidal photonic crystals in order to minimize these screened repulsive Coulomb interactions, thereby minimizing the free energy.[86, 98] Using simulation, Woodcock calculated that a FCC crystal has a lower free energy than a HCP crystal, despite the similarity between the two crystal

structures.[99] The larger thermodynamic stability of the FCC crystal structure may explain why self-assembled colloidal crystals typically form FCC rather than HCP structures.

In this work, two different methods are utilized to self-assemble nanoparticles into FCC crystals that strongly Bragg diffract light. The first method involves the use of highly charged nanoparticles in extensively de-ionized solutions to form non-close packed crystalline colloidal arrays. In this method, many ionizable functional groups are attached to the nanoparticle surface, which dissociate to yield a high negative surface charge and zeta potentials of ~-50 mV at pH 5. After synthesis and functionalization, these colloidal dispersions are dialyzed against large quantities of ultrapure water (18 MΩ·cm) to remove most of the synthetic impurities and electrolytes. The dialyzed colloid is then stored over a mixed bed ion exchange resin, which is a mixture of anion and cation exchange beads designed to further de-ionize the dispersion and exchange any remaining free cationic or anionic electrolytes with H^+ or OH^-. At sufficiently high concentrations, these extensively de-ionized colloidal dispersions strongly diffract light with no further preparation. An example of a non-close-packed FCC unit cell is depicted in Figure 1.4.

The non-close packed self-assembly of nanoparticles into an FCC structure is advantageous because crystallization can occur over a range of nanoparticle concentrations. Tuning the nanoparticle volume fraction by adding or removing solvent from the colloidal dispersion enables the FCC lattice constant to be easily tuned. As discussed in more detail in Chapter 1.4.5, the tunable FCC spacing allows a single batch of monodisperse nanoparticles to form FCC photonic crystals that diffract over a wide region of the electromagnetic spectrum simply by modifying their concentration.

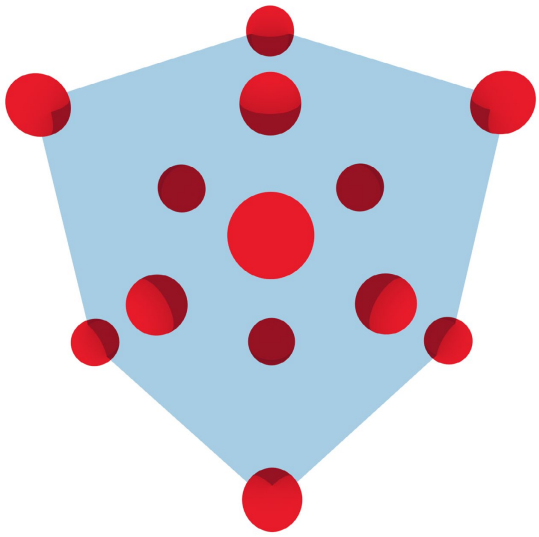

Figure 1.4 – Non-close packed FCC unit cell of spheres (red), looking along the (111) plane normal. A blue, semi-transparent cube whose corners intersect with the centers of the spheres at the corners of the unit cell is included as an aide for the eye.

In addition to non-close-packed photonic crystals, close-packed photonic crystals (Figure 1.5) can also be fabricated via a variety of methods which typically involve controlled evaporation of the dispersion solvent to yield a solvent-less FCC structure attached to a substrate. Techniques including spray coating, spin coating, doctor blade coating, horizontal deposition, and vertical deposition have been utilized to form close-packed photonic crystals.[100] In particular, vertical deposition methods have been thoroughly investigated since the late 1990s due to their ability to form highly ordered close packed arrays with large crystalline domains via relatively straightforward experimental procedures.[53, 63, 64] In a typical vertical deposition procedure, a clean, hydrophilic substrate such as a Piranha cleaned microscope slide is immersed vertically in a vial filled with a dispersion of nanoparticles. The dispersion solvent is then slowly evaporated, yielding a close-packed array of particles on the substrate surface.

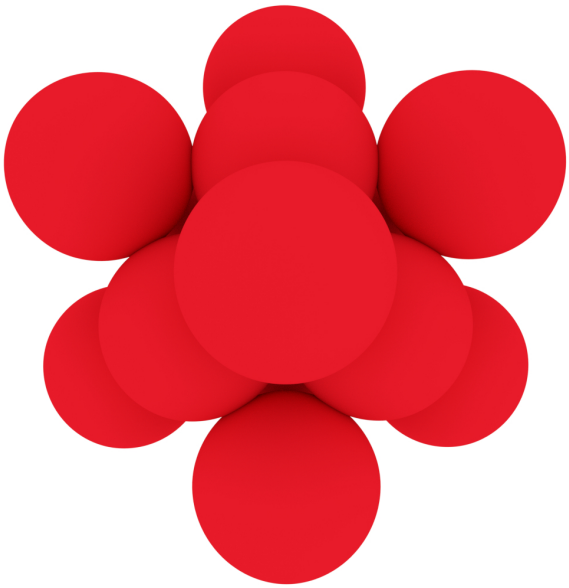

Figure 1.5 – Close packed FCC unit cell of spheres, looking along the (111) plane normal.

Although the experimental procedure is relatively simple to execute in the laboratory, the self-assembly mechanism for close-packed FCC photonic crystals is still poorly understood despite extensive experimental investigation. The current prevailing theory is that convective flow, followed by attractive capillary forces or convective steering forces, drive the self-assembly of nanoparticles into an ordered array.[101]

When a hydrophilic substrate is immersed into an aqueous nanoparticle dispersion a concave solvent meniscus forms against that substrate, where the solvent thickness in the meniscus decreases as a function of distance from the bulk solvent level, as depicted in Figure 1.6.[102] At the top of the meniscus, the solvent film becomes extremely thin and terminates at the contact line, where the substrate surface, solvent, and air closely intersect.[103] Solvent evaporates more quickly near the contact line in the meniscus than from the surface of the bulk solution since the density of neighboring evaporation sites is decreased near the air-substrate-solvent interface.[104] Since solvent evaporates more quickly from the contact line than from the bulk solution, a convective

solvent flow forms where solvent from the bulk solution continuously flows into the meniscus towards the contact line. This convective solvent flow results in a viscous drag of nanoparticles from the bulk solution into the meniscus, concentrating nanoparticles within the spatially confined meniscus region (Figure 1.6).[105, 106]

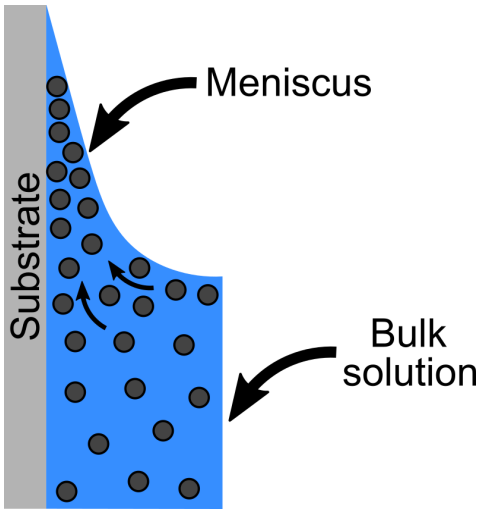

Figure 1.6 – Side-on schematic of a vertical deposition process, where a hydrophilic solid substrate is dipped into a solution (blue) containing nanoparticles (grey circles). Relatively rapid evaporation from the meniscus results in a convective flow of solvent and nanoparticles from the bulk solution into the meniscus, forming a close packed FCC array. Figure adapted from Hufziger *et al.*[107]

Highly concentrated nanoparticles in the meniscus are theorized to crystallize into FCC structures via capillary forces and convective steering forces.[101, 108] Capillary forces are hypothesized to be important in the formation of the crystal nucleus. The capillary force theory was first utilized by Denkov *et al.* to describe the assembly of 2D hexagonally close packed monolayers on horizontal substrates.[106] For a solution of nanoparticles that are closely confined between the air-solvent interface and the solvent-substrate interface, nanoparticles become partially pinned to the substrate surface as the thickness of the solvent approaches that of the

nanoparticle diameter. Further solvent evaporation exposes the tops of the nanoparticle to the surrounding atmosphere, resulting in the formation of menisci between nearby particles due to the wettability of the nanoparticle surfaces (Figure 1.7). The deformation of the solvent surface produces an attractive lateral immersion capillary force that is several orders of magnitude stronger than kT between nearby partially immersed particles.[109] These immersion capillary forces draw nearby particles together, producing a close packed array as solvent continues to evaporate.

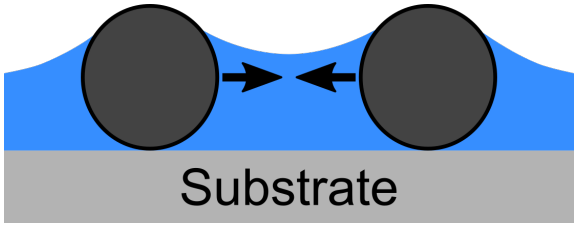

Figure 1.7 – Schematic of the immersion capillary force. Nanoparticles that are closely confined between a substrate and a solvent (blue)-gas interface will deform the solvent surface, producing a strong attractive immersion capillary force that draws adjacent particles together. Figure adapted from Prevo *et al.*[101]

In addition to lateral immersion capillary forces, the other mechanism that is hypothesized to drive array formation is convective steering. After the nucleation of the close-packed nanoparticle array at the meniscus contact line, capillary forces draw solvent through the interstitial spaces between the close-packed nanoparticles.[108, 110] It is hypothesized that as solvent flows through these interstitial spaces, it drags nearby free-floating nanoparticles towards the interstices resulting in crystal growth. These convective steering forces have been observed in video microscopy studies by Meng *et al.* and Yang *et al*., where nanoparticles approaching the crystal growth front at the contact line are clearly drawn towards crystal interstices.[110, 111] Theoretical studies by Brewer *et al.* indicate that for solvent flowing through a close-packed network, solvent

flows more quickly through so-called clear interstices formed as a result of ABC FCC packing than through obstructed interstices formed as a result of ABA HCP packing.[112, 113] As a result, nanoparticles drawn into the growing array via capillary steering forces are more likely to form FCC than HCP close-packed structures.

In a vertical deposition method, as the solvent evaporates the contact line slowly traverses the substrate. By carefully balancing the evaporation rate, which controls the contact line movement rate, with the nanoparticle concentration, which controls the influx rate of nanoparticles into the meniscus region, a continuous, well-ordered photonic crystal can be fabricated.[114] A significant advantage of fabricating close-packed rather than non-close packed aqueous photonic crystals is that at the end of the fabrication procedure, the self-assembled photonic crystals contain no solvent and are attached to solid substrates.

In contrast to the aqueous non-close-packed photonic crystals which rely upon electrostatic repulsion to maintain ordering, solid photonic crystals are much more mechanically durable. In aqueous photonic crystals, repulsive electrostatic interactions can be easily disrupted by the addition of electrolytes. For example, in Chapter 3.0 we observe a degradation in aqueous photonic crystal diffraction that we hypothesize is caused by impurity electrolytes, which screen electrostatic interactions and disorder the FCC array, that were formed upon irradiation with a deep UV laser. In addition, solvent evaporation from non-close-packed aqueous photonic crystals disrupts diffraction by changing the nanoparticle concentration. Close-packed photonic crystals such as those formed via vertical deposition processes necessarily do not depend upon electrostatic interactions or stability of solvent conditions to maintain ordering after fabrication is complete, which greatly improves their utility and durability.

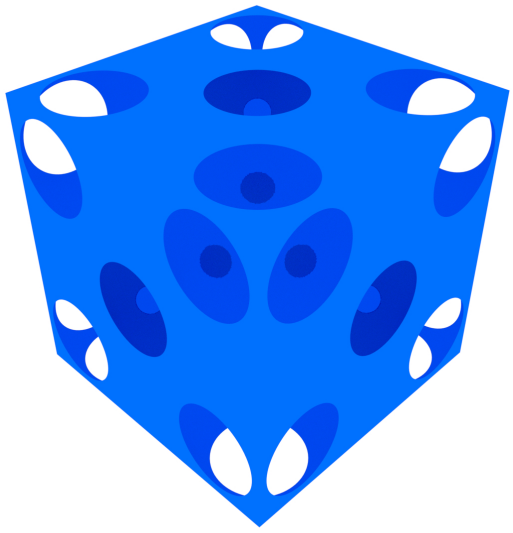

Figure 1.8 – Inverse close-packed FCC structure looking along the (111) plane normal, where the interstices in Figure 1.5 have been completely filled with a polymer (blue) and the nanospheres have been removed, leaving behind empty void space. Sphere to sphere contact excludes monomer during the polymerization process, resulting in small "windows" between spherical air-voids left behind after nanoparticle removal, which are visible as small circles in this schematic.

After deposition, close-packed photonic crystals are commonly converted into inverse opal structures which also diffract light.[53, 115] Inverse opals are typically formed by infiltrating either a monomer or sol-gel precursor into the interstitial spaces between the nanoparticles either during or after the self-assembly process. The monomer solution is then polymerized, immobilizing the nanoparticles in a solid matrix. The nanoparticles are then removed typically via dissolution or calcination at high temperatures while keeping the matrix material intact, yielding an inverse FCC structure where the nanoparticles are replaced by air voids (Figure 1.8). Inverse opal structures are useful because the inversion process allows the materials that comprise the photonic crystal structure to be conveniently changed.

In this work, we utilize the inversion process to produce an inverse opal photonic crystal that diffracts in a spectral region that would be otherwise inaccessible given the size and material of the nanoparticles used to form the original close-packed array. Normally, a photonic crystal composed of close-packed polystyrene nanoparticles could not be used to diffract light in the deep UV due to the electronic absorption of polystyrene at wavelengths <300 nm. Filling this close-packed polystyrene photonic crystal with a UV-transparent material and then removing the polystyrene spheres, however, can be utilized to make an inverse opal that diffracts in the deep UV.

In Chapter 4.0, we utilize polystyrene nanospheres with excellent monodispersity in the presence of TEOS to form a close-packed FCC photonic crystal via a vertical deposition method. During the self-assembly process TEOS condensed in the polystyrene nanoparticle array interstices, forming a solid, deep UV transparent SiO_2 network. We then removed the polystyrene nanoparticles via acid treatment to produce an SiO_2 inverse opal that diffracts in the deep UV.

1.4.5 Photonic Crystal Diffraction and Bragg's Law

Suspensions of nanoparticles have been known to diffract visible light, forming brightly colored iridescent solutions, since the work of Luck *et al*. and Hiltner *et al*. in the 1960s.[85, 90] Since then, interest in the phenomenology of photonic crystal diffraction, photonic crystal self-assembly mechanisms, controlled defect management to modify their optical properties, and applications of photonic crystals as optical devices has grown tremendously.[116, 117] Photonic crystals have been demonstrated and utilized in a huge variety of applications, including as waveguides,[118, 119] allowing light to be directed around sharp 90° corners, optical fibers,[120] inks for anti-counterfeiting measures,[61] the readout technique for chemical and biosensors,[121, 122] and as optical filters for

rejecting certain frequencies of light depending on the angle.[16] Controlling and understanding photonic crystal diffraction is therefore extremely important to optimize their performance depending upon the specific application.

Photonic crystals produced via bottom-up self-assembly of nanospheres into crystalline structures are the most widely studied and used form of these optical devices due to their relative ease of manufacture. The defining attribute of photonic crystals that enables control over the propagation of electromagnetic radiation is that the photonic crystal structure is highly ordered, typically in FCC, HCP, or body centered cubic (BCC) lattices.

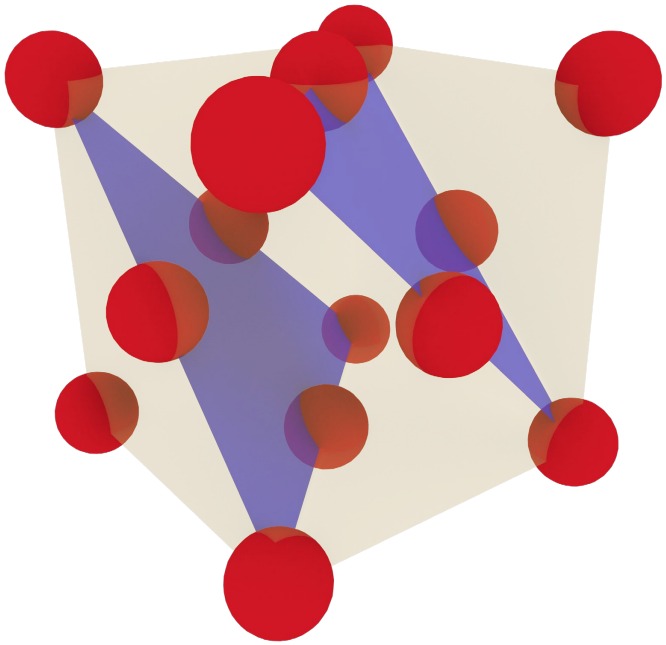

Figure 1.9 – Non-close-packed FCC unit cell of red spheres. A (111) Miller index lattice plane originating in this unit cell, in addition to a (111) plane originating from an above FCC cell (not shown), are depicted as the left and right purple triangles, respectively. The origin in this case is the sphere in the lower back left corner of the unit cell, and the three reference axis run along the edges of the cubic unit cell outwards from the origin.

Photonic crystals and their diffraction can be described and understood using the framework of diffraction planes and their Miller indices, originally utilized to describe x-ray diffraction from atomic crystals.[123] For a colloidal photonic crystal where the nanospheres are arranged in a lattice, planes can be drawn through groups of nanospheres to conveniently describe their orientation relative to reference axes for the lattice. Planes are labelled using Miller indices, which is a set of integer values equal to the inverse of the distance between an origin and the intersection points of the plane with three reference axes drawn from that origin.[123] An example of (111) Miller index crystal planes for an FCC structure are depicted in Figure 1.9. These crystallographic planes provide a useful way to describe, calculate, and understand diffraction from photonic crystals.

When light propagating through a material encounters a change in the dielectric constant, for example when light is incident upon a nanoparticle dispersed in water, it is scattered in all directions.[38] In the case of a photonic crystal that contains a large number of particles regularly arranged into a lattice, the propagation of light with certain wavelengths and polarizations can be completely inhibited in certain directions if light scattered by these particles destructively interferes in those directions, forming a band gap where the propagation of certain wavelengths of light is forbidden inside the photonic crystal.[37, 124] Likewise, certain directions exist where scattered light of a particular wavelength and polarization completely constructively interferes, allowing light propagation in that direction. The condition for complete constructive interference of scattered light is defined as the Bragg condition. Light incident upon a photonic crystal that meets the Bragg condition will be diffracted and cannot propagate through the photonic crystal.

Quantitatively, the Bragg condition for constructive interference is described by Bragg's law (Equation 1.1), first utilized by W. L. Bragg in the early 20th century to describe x-ray diffraction from an atomic lattice.[125]

Equation 1.1 $$m\lambda_0 = 2nd_{hkl}sin(\theta)$$

where m is the diffraction order, λ_0 is the wavelength of light in vacuum, n is the average refractive index of the photonic crystal, d_{hkl} is the spacing between two crystal planes of Miller index (hkl), and θ is the glancing angle relative to that particular set of crystal planes, after accounting for refraction by the photonic crystal.[126] Bragg's law can be derived and intuitively understood by considering the geometry of adjacent lattice planes within the crystal (Figure 1.10).

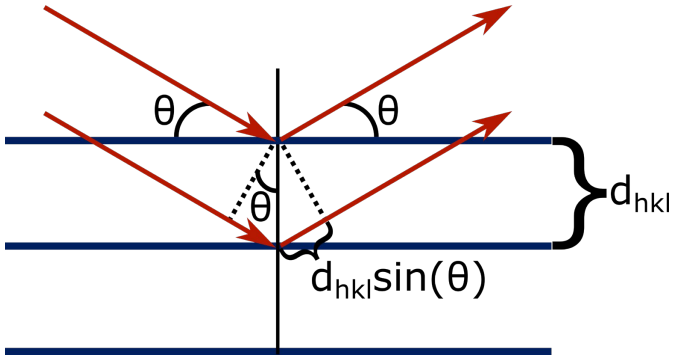

Figure 1.10 – Depiction of the Bragg condition, where the lattice planes, such as the (111) planes shown in Figure 1.9, are depicted as blue lines separated by the distance d_{hkl}. Light, depicted by red arrows, is incident from the left and is diffracted by these lattice planes towards the right. Figure adapted from Kittel.[127]

For light propagating through the crystal that is scattered by spheres contained within two successive lattice planes, light being scattered by spheres in the second plane in the direction depicted by the right arrows in Figure 1.10 must travel an additional distance equal to $2d_{hkl}sin(\theta)$.[127] For light being scattered by spheres in these two planes to be in phase and constructively interfere, this path difference must equal an integer multiple of the wavelength, equal to $n\lambda$. For a particular

diffraction order, only light of one particular wavelength can fulfill this Bragg condition. Light scattered in this direction by these planes at other wavelengths that do not fulfill the Bragg condition will not be in phase and will not be Bragg diffracted by the photonic crystal. Light at these wavelengths will instead be transmitted through the photonic crystal.

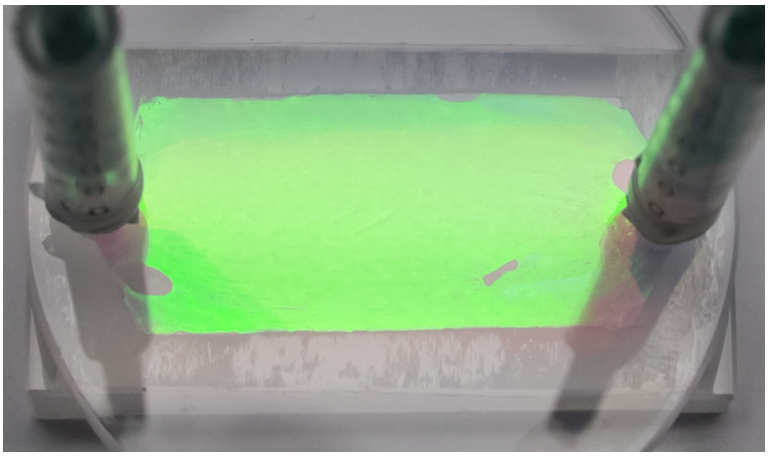

Figure 1.11 – Photograph of a non-close-packed FCC photonic crystal composed of highly charged ~100 nm diameter polystyrene nanospheres injected between two fused silica plates, showing bright green (111) Bragg diffraction.

For a given crystal structure and lattice constant, there are many different crystal lattice planes at different orientations and plane spacings that can each Bragg diffract light. Fortuitously, the FCC (111) lattice planes have a spacing and orientation such that at incidence angles near the (111) plane normal, their Bragg diffraction does not overlap in wavelength with the Bragg diffraction from any other FCC crystal planes. Furthermore, the (111) planes result in the longest wavelength diffraction possible in an FCC crystal. The spectral separation and long-wavelength nature of FCC (111) Bragg diffraction is advantageous because it allows for the construction of photonic crystal optical devices that select and diffract just one narrow bandwidth spectral region,

while allowing light that does not meet the Bragg condition to transmit through the device. A typical non-close-packed photonic crystal containing ~100 nm nanoparticles with a lattice spacing of several hundred nm is depicted in Figure 1.11, showing bright green iridescence resulting from the spectrally distinct (111) Bragg diffraction.

The pathlength difference for light scattered by nanoparticles in adjacent crystal planes is angle dependent. As a result, Bragg's condition changes depending upon the glancing angle (θ) of light upon a set of crystal planes, allowing the diffracted wavelength to be tuned over a certain range by modifying the angle of the photonic crystal relative to the incident light. In addition to tuning the diffraction wavelength by controlling the light glancing angle, the photonic crystal diffraction wavelength can be significantly varied by modifying the plane spacing d_{hkl}. d_{hkl} can be controlled by tuning the concentration of the nanoparticles, where lowering the nanoparticle concentration yields a larger inter-particle spacing and a larger d_{hkl} spacing. Since monodisperse nanoparticles are readily fabricated from ~30 nm to >1000 nm in diameter and their concentrations can be modified via centrifugal concentration or dilution with additional solvent, colloidal photonic crystals can be made to diffract from the deep UV through the IR spectral regions.[49]

The wavelength tunability and spectral separation of the (111) diffraction band from bands diffracted by other Miller index planes are the key features that allow these photonic crystals to be used as wavelength selection optics that select and diffract a narrow bandwidth spectral region of light. In this dissertation work, we extensively developed and utilized photonic crystals as wavelength selection optics inside Raman imaging spectrometers. In these studies, we irradiated samples of interest with a laser to produce Raman scattering, collected that scattered light, and directed it onto a photonic crystal optic placed within the spectrometer. We carefully selected the angle of the photonic crystal such that a particular Raman spectral region met Bragg's condition

and was diffracted by the photonic crystal. Focusing this Bragg diffracted Raman light onto a CCD camera sensor yields an image made up of light only from a certain number of Raman bands, allowing the spatially dependent chemistry of the irradiated sample to be precisely investigated.

1.5 Explosive Detection

Section 1.5 was previously published in the *Journal of Raman Spectroscopy* as K. L. Gares,* K. T. Hufziger,* S. V. Bykov, and S. A. Asher, "Review of Explosive Detection Methodologies and the Emergence of Standoff Deep UV Resonance Raman". J. Raman Spectrosc. 2016. 47(1): 124-141, where "*" denotes equal contribution, and is reprinted with permission. This section was prepared by K.T.H. with the assistance of S.V.B and S.A.A.

1.5.1 Non-standoff Explosive Detection

The September 11th 2001 attack on the US and the subsequent wars in Afghanistan and Iraq dramatically increased the apparent need and funding for explosive detection.[128] The goal of this review is to discuss the leading explosive detection methodologies and to compare them with the emergence of standoff deep UV resonance Raman (UVRR) spectroscopy. Several non-standoff methodologies are already widely utilized by law enforcement and military personnel.

Canine olfaction is known to be extremely sensitive and trained dogs have been used for explosive detection since World War II.[129] Despite the rapid development of explosive detection instrumentation, trained dogs are still one of the most widely employed detection systems because they offer sensitivity, specificity, and directionality found lacking in many portable analytical

systems. Limited evidence suggests that canines can sense some analytes at parts per trillion (ppt) levels,[130] however there are numerous challenges associated with use of canine detection. Canine duty time is generally limited to just a few hours a day, and canine sensing effectiveness is a function of training, physical activity, and handler influence.[131,132,133,134] At present the mechanism of olfaction is not well understood and it is unclear if trained canines sense the analyte of interest or accompanying impurities present in the explosive material.[135,136]

Ion mobility spectrometry (IMS) is an analytical technique that sees widespread use in airports worldwide for explosive detection.[137,138] The technology used in IMS is relatively mature which facilitates its development for field use.[139,140,141,142] Sample collection typically occurs using surface swabbing. The swab is then rapidly heated to evaporate any adsorbed volatile species. A "sniffing" methodology can also be utilized where air is drawn directly into the IMS spectrometer to be sampled.[139] Samples introduced into the IMS spectrometer are typically pre-concentrated before being ionized via radioactive ^{63}Ni, electrospray ionization, photo-ionization, or corona discharge, among other approaches.

The ions are then introduced into a drift tube along with a carrier gas, which is typically purified air. An electric field applied across the length of the drift tube propels ions through the field at different characteristic velocities which depend on their mass, charge, and collision cross sections before being detected (Figure 1.12). Detection limits for explosive molecules readily reach into the picogram regime.[143,139] IMS is a widely adopted explosive detection method due to the commercialization of small, easy to use instruments that produce results in several seconds.

However, there are several challenges faced by IMS. Since analyte molecules need to be physically drawn into the spectrometer, this precludes the use of IMS for standoff detection. The necessity of physical sample handling also hampers automated screening as well as the screening

of large objects. Trace vapor detection is also impeded by the extremely low vapor pressures (ppb) of many explosives.

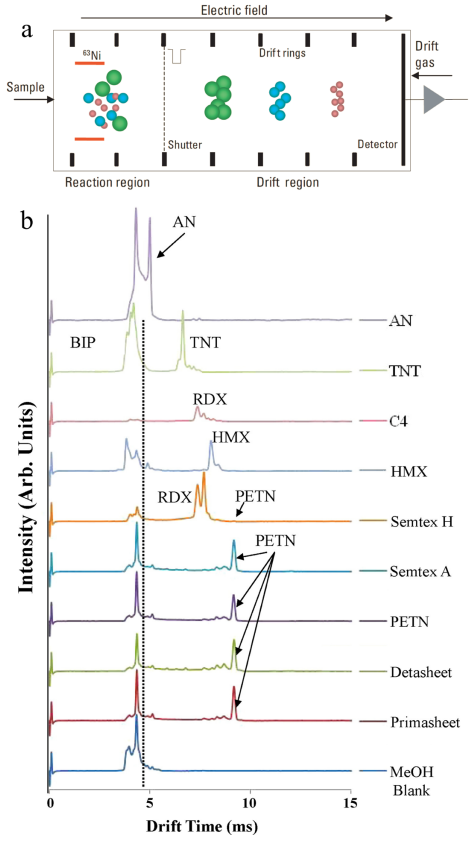

Figure 1.12 – (a) Example of an IMS measurement. First, molecules are introduced into the reaction region to be ionized before being introduced into the drift region to be separated by mass, charge, and collision cross section before being detected. (b) Example spectra of several explosives detected by an ion mobility spectrometer. Figure adapted from Eiceman *et al.* and Hilton *et al.*[144, 145]

Colorimetric and fluorimetric assays produce spectral changes upon interactions with explosive analytes. Color-based techniques offer low cost, simple to interpret, instrument free detection that can be performed by untrained personnel in the field. Three broad categories of color-based detection exist: colorimetric, fluorescence quenching, and fluorescence

activation.[146,147] Colorimetric based assays typically function by utilizing Griess and Meisenheimer chemistries to produce brightly colored compounds upon reaction with nitrites (NO_2^-) and nitroaromatics, respectively. In a Griess test, nitrate esters and nitramines are treated with base to release NO_2^-, followed by treatment with sulphanilic acid and an arylamine to produce a bright pink azo dye,[146] enabling visual detection of RDX, HMX, PETN, NG, and nitrocellulose.[148]

Alternatively, nitroaromatics such as TNT and dinitrotoluene (DNT) can react with nucleophilic bases to produce brightly colored Meisenheimer complexes with ppm detection limits.[149] These technologies have been developed as commercially available spray kits for field detection of explosives.[150] While these tests are rapid, inexpensive, and simple to use, the utilization of colorimetric detection is hampered by its lack of specificity and its moderate sensitivity. The Griess test, for example, can produce false positives if fertilizer, nitrocellulose (commonly found in lacquers), or other sources of NO_2^- have contaminated the interrogated area.

Fluorimetric quenching explosive detection assays typically utilize electron rich conjugated polymeric substrates which contain many fluorophores that act as binding sites for explosive molecules.[146] When the polymer is excited by photon absorption the excited state involves multiple fluorophores along the polymer chain.[151,152] If a quenching molecule such as an electron deficient nitroaromatic is bound to a sampled binding site, the excitation will be quenched. The quenching of multiple fluorophores by a single analyte molecule greatly enhances detection sensitivity.[153] This has enabled ppb level sensing for TNT, DNT, and dinitrobenzene (DNB).[154,155,156,157] Cumming *et al*. demonstrated a sensor system (Fido) that consists of a chamber containing a fluorescent pentiptycene polymer film which samples air being drawn through the sensor inlet.[4] A blue LED fluorescence excitation source and a photomultiplier (PMT) detects the

decrease in fluorescence intensity when explosive analytes bind to the polymer film (Figure 1.13). TNT was detected at ppt levels in air as well as in the air surrounding deactivated landmines buried at a DARPA test range. This methodology has been commercialized for handheld explosive detection fluorescence quenching devices for military use.

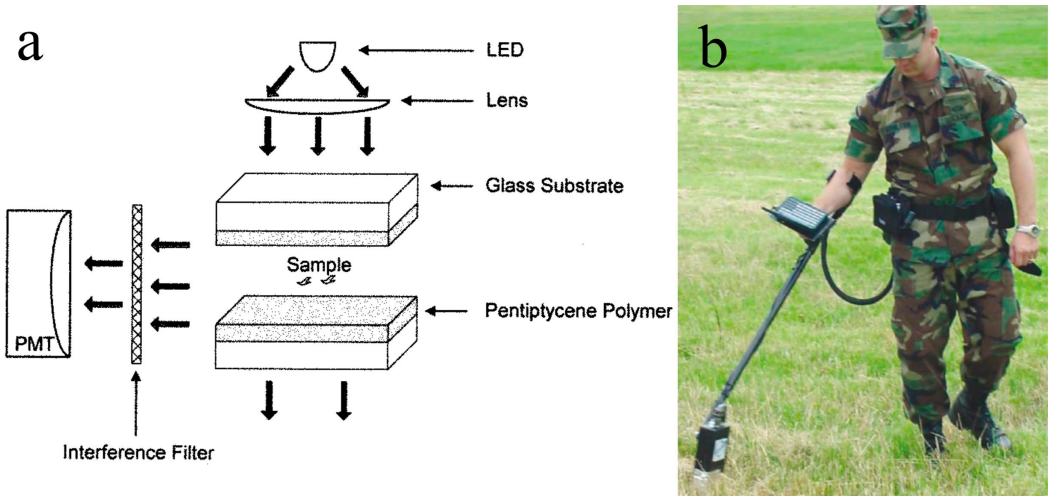

Figure 1.13 – (a) Schematic of the Fido fluorescence quenching explosive sensor originally demonstrated in 2001. (b) Handheld Fido 4A fluorescence quenching instrument. Figure adapted from Cumming *et al.* and Swager *et al.*[4, 158]

Fluorescence turn-on methodologies have recently been developed. These sensors function by forming fluorescing species upon reaction with specific explosive molecules. The emission of these fluorophores sensitively reports the presence of explosives. PPM sensitivities for RDX and PETN were reported as well as ppb sensitivities for TATP and TNT.[159,160,161] The broad challenge facing color-based sensors is that each sensor is designed to sense a specific explosive of interest, or a single class of explosives. Thus, multiple sensors are required for field detection of explosives. These methodologies are not amenable to standoff detection.

In addition to the methods mentioned above, there exist a multitude of other techniques that are currently being investigated for the purpose of explosives detection. These methods include mass spectrometry[162,163,164] and neutron techniques[165] for explosive identification, as well as X-ray and X-ray computed tomography (CT) methods for imaging suspected explosive devices in airline luggage.[166] These analytical methods all have the disadvantage that that they need to be placed in direct proximity to the interrogated object in order to analyze its composition.

1.5.2 Standoff Explosive Detection

Approaching a suspicious object such as a suspected IED is extremely undesirable from a safety standpoint. It is therefore highly desirable to develop standoff methodologies to determine the composition of a sample from a safe distance in order to keep both personnel and instrumentation from harm. Laser based spectroscopies appear to be the only currently viable standoff detection methods. Standoff spectroscopic measurements have been demonstrated at distances of tens to hundreds of meters.[25,167,168] Furthermore, since no physical interaction with the sample is necessary, it is possible to construct instruments that can continually and automatically survey an area (for example, a military checkpoint), and alert an operator if a hazardous analyte is detected. Spectroscopic techniques can be highly selective and can be employed to detect many different analytes of interest. Laser spectroscopies can also be utilized in chemical imaging methodologies to obtain spatially resolved chemical composition information.[12,169,170]

Standoff spectroscopic methods face significant challenges. As the distance from the object being analyzed to the collection optic increases, the amount of light collected will decrease as the inverse square of the distance.[25] Long distance measurements typically require the use of

large telescopes for light collection, high laser powers, efficient spectrometers, and long accumulation times. The collected signal intensity increases with excitation power; however, eye and skin-safe field detection requires low laser powers.

Figure 1.14 – Cart mounted standoff LIBS instrument utilized for explosive detection. A Nd:YAG laser produced 350 mJ pulses of 1064 nm light to excite samples including TNT, RDX, and C-4 placed on a car door at 30 m standoff. Figure adapted from Lopez-Moreno *et al.*[171]

Laser induced breakdown spectroscopy (LIBS) has recently been developed as a spectroscopic technique for standoff explosive measurements.[172,173] LIBS utilizes short, high peak power laser pulses to produce dielectric breakdown of the sample surface, resulting in rapid heating and plasma formation.[174,175] Materials ablated by the plasma spark decompose into multiple smaller molecular, ionic, and atomic species. These species are excited by the plasma before relaxing and emitting photons of characteristic wavelengths. The intensity ratios of the atomic emission lines from C, N, O, and H can be used to infer the original molecular structure stoichiometry by comparing the collected spectra to standard spectra taken of known compounds

under similar experimental conditions. LIBS has recently been applied to standoff explosive sensing because it offers the possibility of high signal, long standoff ranges, and low spectral accumulation times without the necessity of sample preparation.

Several standoff LIBS instruments for explosive detection have been demonstrated over the past decade. Lopez-Moreno *et al*. demonstrated a portable cart sized LIBS instrument that detected TNT, RDX, and C-4 deposited on a car door 30 m away (Figure 1.14).[171] A challenge facing field measurements of unknown samples is whether it is possible to identify explosive spectral signatures in the presence of other emitting interferents. The authors developed a spectral analysis method in the form of a flow chart that they use to determine the presence of explosives.

Gottfried *et al*. studied and developed partial least squares (PLS) and principle component analysis (PCA) chemometric software to aid in the identification of explosive spectral signatures in the presence of other emitting interferents on different substrate materials.[176,177,178] Lucena *et al*. recently constructed an imaging LIBS system that could image fingerprints of explosive molecules at a range of 30 m.[179] González *et al*. found that they could utilize LIBS to measure TNT and C-4 placed behind transparent sheets of plastic and glass.[180]

There is interest in combining LIBS and Raman spectroscopy within a single instrument in order to measure both elemental and molecular sample information. Moros *et al*. developed a combined Raman/LIBS instrument that utilized a single 532 nm laser pulse to generate both the LIBS plasma and the Raman scattering which were collected by a telescope and directed into two separate spectrometers in order to collect both spectra simultaneously.[181] NH_4NO_3, RDX, DNT, TNT, PETN, potassium chlorate ($KClO_3$), and sodium chlorate ($NaClO_3$) were all measured at a distance of 20 m.

The largest challenge facing the implementation of LIBS as an explosive detection technique for field use is that the LIBS spectra strongly depend upon the detailed experimental conditions. Matrix effects including the emission of molecules on or within the substrate, as well as in the surrounding atmospheric gases can complicate analyte identification. In addition, organics within the plasma can react to form new species with different spectral emissions. The matrix composition, as well as the incident laser pulse temporal width, energy, and wavelength impact the excited plasma, complicating qualitative and quantitative analysis.[172] LIBS instruments are also intrinsically eye-unsafe due to their need for high power laser pulses.

Raman spectroscopy has also been widely utilized for standoff detection. Raman spectra are generated by exciting a sample with a monochromatic light source, normally a laser. Raman spectra detail the intensity of inelastically scattered light as a function of the frequency difference relative to the excitation light.[23,21,10] These spectra detail both the structure and environment of the scattering molecule. Thus, Raman spectra serve as sensitive and specific fingerprints that can be used to determine the chemical composition of illuminated samples. Raman spectroscopy can be used as a standoff, highly specific, non-destructive, eye-safe monitor of molecular composition.

In the early 90's, Angel *et al*. demonstrated a portable visible Raman standoff spectrometer that utilized a visible Ar^+ ion laser to detect several salts including solid and solution state $NaNO_3$ at a 17 m distance.[182] The goal of this study was to develop a system capable of measuring contaminants inside of storage tanks at waste disposal sites.

The first demonstrations of standoff Raman for explosive detection were by Carter *et al*. and Sharma *et al*. in the early 2000's.[25,183] The instrument developed by Carter *et al*. utilized a frequency doubled Nd:YAG laser (532 nm) for excitation and a 20 cm open aperture Cassegrain telescope to collect the scattered light from samples at a 50 m standoff distance. The Raman

scattered light from TNT, RDX, PETN, and NH_4NO_3 was collected, dispersed, and detected with a gated, intensified CCD (ICCD) camera. The authors demonstrated that use of a short ICCD gate width greatly reduced the background contribution of ambient light and decreased the contribution of sample fluorescence (Figure 1.15). The authors estimated a limit of detection (LOD) for their instrument of ~250 ppm for 1000 laser pulses (100 s integration) at 27 m standoff distance for 8% w/w RDX contained in a sand matrix.

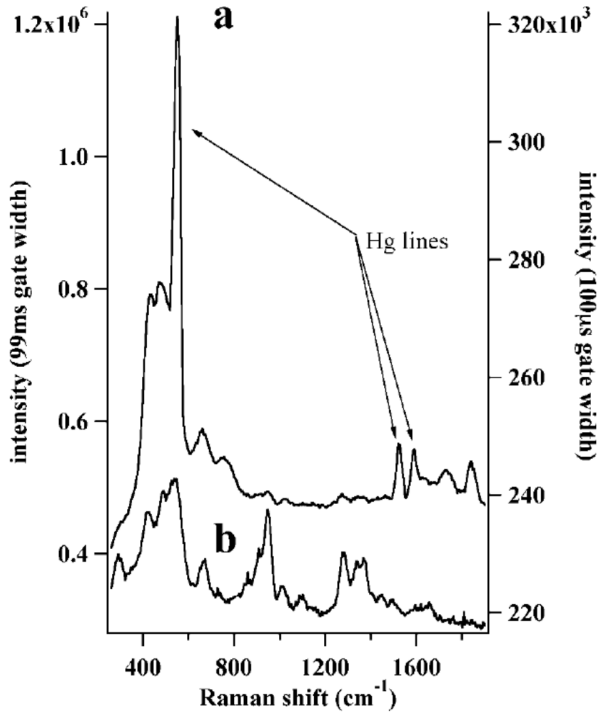

Figure 1.15 – 27 m standoff Raman spectra of RDX with a (a) 99 ms and (b) 100 µs ICCD gate width. The spectra show strong Hg lines from fluorescent ceiling lamps that appear with longer gate widths. Figure adapted from Carter *et al.*[25]

Several Raman standoff studies were performed by the Swedish Defense Research Agency (FOI). Pettersson *et al*. utilized 532 nm excitation coupled with a 15 cm open aperture Cassegrain telescope to collect Raman light from samples such as nitrobenzene (NB), TATP, methyl ethyl

ketone peroxide (MEKP), and HMTD contained within glass containers placed outdoors ~30 m away.[184] Östmark *et al*. recently demonstrated a standoff visible Raman imaging spectrometer which utilized 532 nm excitation and a telescope to collect a hyperspectral Raman image of solid chunks of sulfur, DNT, NH_4NO_3, and TNT placed 10 m away (Figure 1.16).[14] A liquid crystal tunable filter (LCTF) was utilized to transmit only a single narrow wavelength spectral region (~0.25 nm) to be focused onto a CCD camera. The LCTF could be rapidly wavelength tuned to enable efficient hyperspectral image collection. By judiciously selecting and imaging the Raman bands characteristic of each analyte, the different explosives could be easily distinguished in the resulting Raman spectral images.

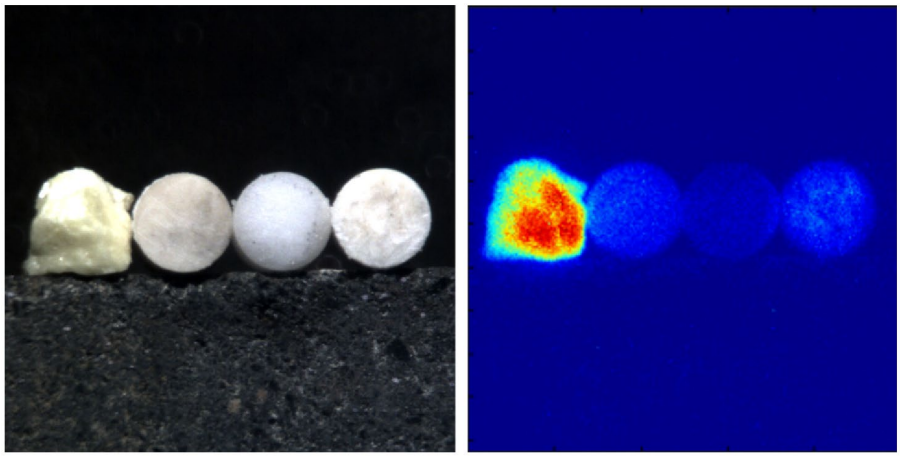

Figure 1.16 – (a) White light image of solid 5 mm diameter sulfur, DNT, NH_4NO_3, and TNT samples from left to right. (b) Raman spectral image of the samples depicted at left indicating the sum of the measured Raman band intensities. Color indicates relative Raman intensity from low (blue) to high (red). Sulfur scatters Raman light much more intensely than the three other samples, resulting in a bright red feature. Figure adapted from Östmark *et al.*[14]

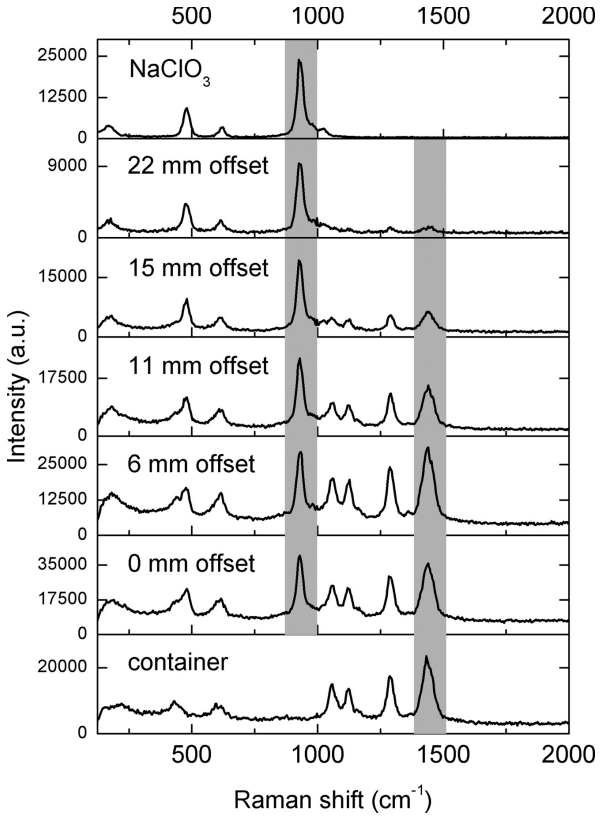

Figure 1.17 – Spatially offset Raman spectra of solid $NaClO_3$ held within a 1.5 mm thick HDPE container at 12 m standoff. Neat $NaClO_3$ and HDPE are depicted in the top and bottom spectra, respectively. The ratio of $NaClO_3$ to HDPE Raman bands increase with the spatial offset between the collection optic and the exciting beam. Figure adapted from Zachhuber *et al.*[185]

Collecting Raman spectra of samples within containers can be difficult because the container walls also Raman scatter and interfere with determination of the container contents. Spatially offset Raman spectroscopy (SORS) utilizes a spatial offset between the laser excitation spot and the spot where the collection optic is focused in order to minimize the contribution of Raman bands from the container walls. This increases the relative intensities of the Raman bands of the container's contents.[186] The principle behind SORS is that Raman scattered light generated by a highly scattering sample powder inside a container is more likely to propagate laterally before it exits the container, compared to Raman light generated by the container wall.[186] Therefore, as

the collection optic is pointed away from the laser excitation, more Raman scattered light from the container contents are observed relative to that from the container wall.

Zachhuber *et al*. recently demonstrated standoff SORS for the analysis of chemicals within containers.[185,187] A 532 nm laser beam with beam directing optics to produce the spatial offset was utilized to generate Raman scattering in the sample that was then collected by a telescope. Offset Raman spectra were measured of $NaClO_3$ contained within semi-opaque, high density polyethylene (HDPE) containers placed 12 m away. At 0 mm offset, the telescope and laser beam are coaxial and the collected spectra contains Raman bands from both $NaClO_3$ and HDPE (Figure 1.17). However, as the offset between the laser beam and the telescope increases the HDPE bands diminish in intensity relative to $NaClO_3$ and the collected spectra approaches that of pure $NaClO_3$. The ability to collect Raman spectra through semi-opaque containers can be important for field use in cases where bulk explosive materials are stored within containers.

Misra *et al*. demonstrated that visible Raman spectra can be measured from greater than 100 m standoff distances.[24] Single 100 mJ pulses of 532 nm light excited NB, potassium perchlorate, and NH_4NO_3 samples inside sealed glass vials 120 m away (Figure 1.18). The Raman scattered light was collected by a 20 cm diameter telescope and focused into a spectrograph. The light was detected by an ICCD camera. Importantly, no cosmic ray removal or baseline correction was necessary before data analysis due to the use of ICCD gating to detect spectra only during the brief time period during the arrival of Raman scattered light in order to minimize spectral interference from ambient light and cosmic rays. High S/N spectra were easily measured with short accumulation times. Collection of high S/N spectra with minimal contributions from spectral interferents is important for field instrumentation in order to enable trace explosives identification.

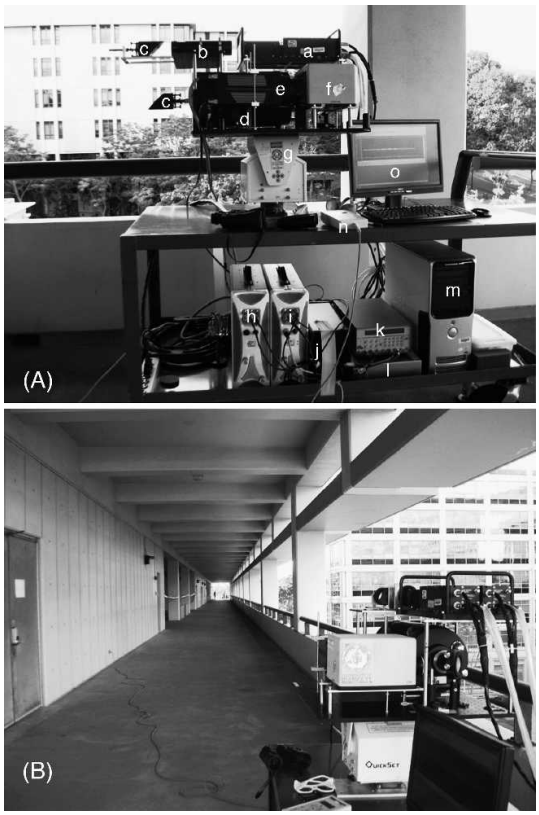

Figure 1.18 – Standoff visible Raman spectrometer constructed by Misra *et al.* pointed at samples 120 m away. Figure adapted from Misra *et al.*[24]

Until recently most standoff excitation studies utilized visible and near IR wavelength lasers such as Ar and Kr ion lasers, frequency doubled Nd:YAG lasers, and diode lasers due to their widespread availability. In addition, high quality optics and optical filters which can be used to reject Rayleigh scattered light are also easily available for visible and near IR wavelength excitation. Visibly excited standoff Raman spectroscopy is challenged by sample and impurity fluorescence, which often occurs in the same spectral region as the Raman bands of interest. Intense fluorescence can degrade spectral S/N which impedes analyte detection. Pulsed laser excitation and gated detection can be utilized to reduce contributions from fluorescence as well as

ambient light and cosmic rays. However, the use of pulsed laser excitation significantly increases the eye safety hazards associated with the field standoff measurements.

1.5.3 Advantages of UV Excitation for Raman Spectroscopy

Although visible Raman spectroscopy has been successfully used for standoff detection of bulk amounts of explosives, trace explosives detection will be difficult with visible or near IR excitation due to the generally small visible or near IR Raman cross sections that result in low sensitivity. Furthermore, visible and near IR excitation cannot be used to selectively enhance the resonance Raman spectra of explosives. For visible excitation, Raman bands of explosives have cross sections similar to those of interferents and substrates. This degrades the ability to spectrally differentiate between explosive analytes and interferents.

Excitation in the deep UV (< 260 nm) results in an increased selectivity and sensitivity of standoff Raman due to resonance enhancement, the ν^4 dependence of the scattered intensity, and the lack of deep UV interference from fluorescence.[21,188] Resonance enhancement results in increased Raman intensities from molecules that absorb near or at the excitation wavelength.

Fountain *et al*. and Emmons *et al*. measured the dependence of Raman scattering intensities of NH_4NO_3 and TNT on both the excitation wavelength (from the near IR to the UV) and on the sample thickness.[33,27] The authors demonstrated that deep UV excitation is advantageous for thin film detection where the increased *resonance* Raman cross sections increase the observed intensities (Figure 1.19). They also showed that the increased Raman intensities associated with resonance enhancement is limited by sample absorption. This absorption limits the penetration depth for the excitation beam.

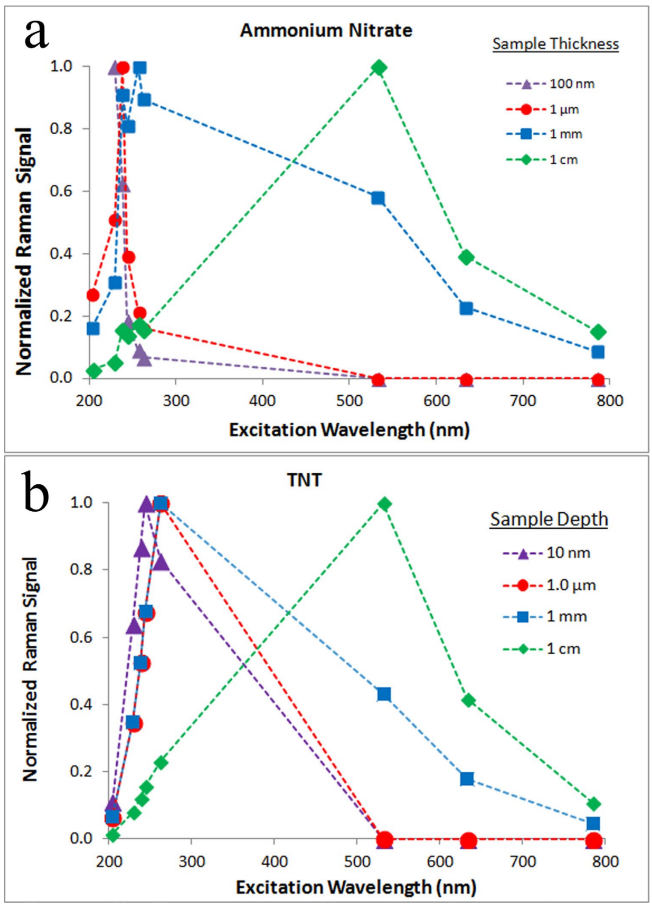

Figure 1.19 – Normalized Raman intensity for the (a) 1044 cm^{-1} band of solid NH_4NO_3 and (b) 1620 cm^{-1} band of solid TNT as a function of sample thickness and excitation wavelength. Figure adapted from Fountain *et al.*[33]

Visible wavelength excitation results in high Raman intensities for thick explosive samples where there is negligible absorption of the excitation beam. Visible excitation produces Raman scattering from a much greater depth of a thick sample because the laser beam is not strongly attenuated. Visible and near IR wavelength excitation is advantageous for thick, transparent samples, which are unlikely to be encountered in the field. UV excitation is advantageous for trace explosive detection which generally involves thin samples.

UV excitation is also beneficial for standoff instrumentation because the higher eye exposure limits for deep UV light allows the use of higher laser powers compared to visible excitation. Carroll *et al*. recently compared the use of 532 and 266 nm excitation for eye-safe standoff detection.[189] The authors conclude that because the maximum permissible exposure (MPE) set by ANSI is much higher for UV light compared to visible light, higher beam powers can be utilized for UV standoff detection, giving a 130-fold increased detection distance for 266 nm excitation compared to 532 nm. At 266 nm the photochemical MPE set by ANSI is 3 mJ/cm^2, which allows 1 sec of sample illumination with a 10 Hz, 1 mW average power 7 mm diameter beam. The authors calculate that for their instrument, these conditions enable an eye-safe 3 m maximum detection distance for Teflon. It should be noted that protection of personnel against deep UV light is easily accomplished by utilizing glass enclosures and plastic goggles.

1.5.4 Standoff UV Raman Spectroscopy

Several groups have begun exploring the feasibility of standoff UV Raman towards explosive detection.[190,191,192,193,194,195] Hug *et al*. (Photon Systems Inc.) and Bhartia *et al*. (Jet Propulsion Laboratory/Caltech) have developed portable UV Raman instrumentation utilizing small transverse excited hollow cathode (TEHC) 248 nm NeCu lasers.[190-192] Waterbury *et al*. (Alakai Defense Systems) have recently constructed a truck mounted UV Raman system for standoff detection.[193]

The Swedish Defense Research Agency has developed deep UV Raman instruments for standoff detection. Ehlerding *et al*. constructed instruments that utilized deep UV excitation generated by an optical parametric oscillator (OPO) pumped by the 3rd harmonic of a Nd:YAG laser.[194] Scattered light was collected by a 13 cm telescope at a 1.6 m standoff distance. The

Raman light was dispersed by a single spectrograph and detected by an ICCD. Vapor phase TNT and DNT were detected with 100 sec accumulation times. NM was also measured outdoors at a 13 m standoff distance.

Reichardt *et al*. constructed an instrument that used 244 nm excitation for the detection of TNT that employed a conventional Czerny-Turner spectrograph with an ICCD detector.[195] The authors utilized their measured spectral S/N ratios for standoff measurements to estimate the accumulation times necessary to detect TNT. They concluded that detection of >6 $\mu g/cm^2$ amounts of TNT at ~100 m standoff distances would require >10 sec accumulation times.

Advances in UV Raman instrumentation will aid in the development of standoff UV Raman methods for trace explosive detection. While visible and near IR Rayleigh rejection optical filter technology is mature and relatively inexpensive, commercialized deep Rayleigh rejection filters have much poorer performance with low out-of-band transmission, as well as insufficient cutoff band edge steepness. This has previously necessitated the use of multistage spectrometers with low light throughput.

We recently developed a novel high throughput, high dispersion deep UV Raman spectrometer. This spectrometer consists of a high efficiency filter stage monochromator and a high dispersion Echelle spectrograph (0.04 nm/mm dispersion at 229 nm). This high dispersion allowed us to open the entrance slit to 1 mm, while maintaining a spectral resolution of ~10 cm^{-1} full width half max (FWHM). Use of a 1 mm wide entrance slit results in a ~35-fold throughput increase compared to previously UV-optimized Raman spectrographs.[196] We utilize this spectrograph in a prototype standoff deep UV Raman spectrometer we are developing.[197] We also developed novel deep UV Rayleigh rejection filters and Raman imaging optics as discussed in detail below.

The development of standoff deep UV Raman instruments has also been slowed by the lack of suitable deep UV laser sources. Current UV Raman measurements mainly utilize Nd:YAG 3rd (355 nm), 4th (266 nm) and 5th (213 nm) harmonics, the second harmonics of visible Ar^+ ion laser lines at 257, 248, 244 and 229 nm, and UV-tunable (193-240 nm) harmonics of Ti:Sapphire tunable lasers.[198] For wavelengths below 244 nm, these lasers produce < 20 mW output power. These lasers are large, heavy, require water cooling, and are relatively inefficient. High power low duty cycle excimer lasers, like ArF at 193 nm and KrF at 248 nm, require use of highly poisonous and reactive halogens. High average power, portable, easy to operate UV lasers are required for standoff Raman instruments.

In collaboration with UVisIR Inc. we recently developed a novel, compact, acousto-optically Q-switched diode pumped solid state (DPSS) intracavity-frequency tripled Neodymium-doped Yttrium Vanadate ($Nd:YVO_4$) laser capable of producing up to 100 mW of quasi-CW 213 nm light. The light is generated as 15 ns pulses at a 30 kHz repetition rate.[197] We utilized this new laser in a prototype standoff deep UV Raman spectrometer. We monitored the UVRR spectra of solid and solution nitrate species utilizing our lab built Echelle deep UV Raman spectrometer.[197] The laser beam size was ~2 mm in diameter at the sample (~30 mW/cm^2) and Raman scattered light was collected by a 5 cm plano-convex lens. At a ~2.2 m standoff distance we were able to easily monitor the NO_3^- symmetric stretching band of 1 mg/cm^2 $NaNO_3$ powder spread on a metal surface (Figure 1.20), and of 20 μM aqueous solutions of $NaNO_3$ (Figure 1.21).

We monitored the 1065 cm^{-1} ν_1 NO_3^- symmetric stretching band of solid $NaNO_3$ for different amounts of solid $NaNO_3$ per cm^2 (Figure 1.20).[197] We are able to clearly detect the 1065 cm^{-1} Raman band of solid $NaNO_3$ at ~1 mg/cm^2 with a 60 sec accumulation time. We estimate a

~100 μg/cm^2 detection limit for 1 min accumulation times for the ν_1 symmetric stretching vibration of solid NO_3^-.[197]

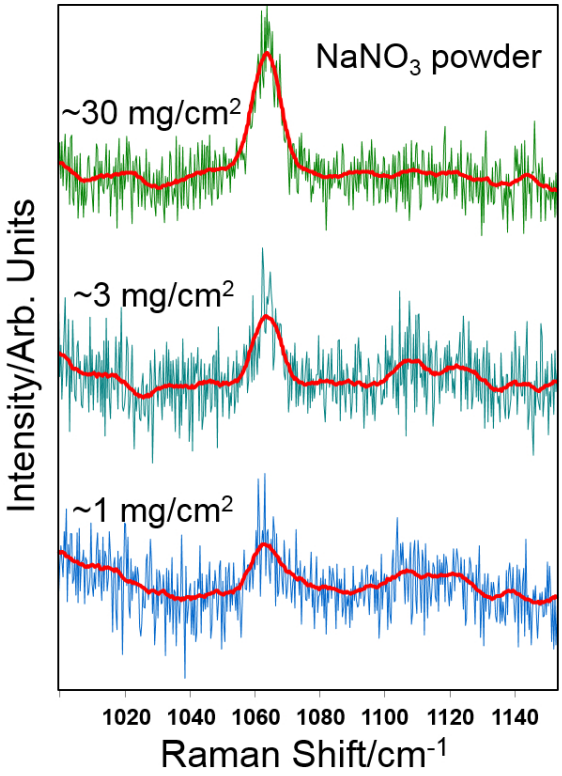

Figure 1.20 – 2.2 m standoff 213 nm UVRR spectra of different amounts of solid $NaNO_3$ powder. Spectra were accumulated for 60 sec and the irradiance is ~30 mW/cm^2. The smoothed (Savitzky-Golay) and raw spectra are overlaid. Figure adapted from Bykov *et al.*[197]

We also monitored the 213 nm excited ν_1 symmetric stretching vibration of NO_3^- at ~1044 cm^{-1} for solution state NH_4NO_3 at different concentrations (Figure 1.21). The 1044 cm^{-1} band is detectable for 20 μM solutions with 10 sec accumulation times.[197] For the most concentrated 2 M NH_4NO_3 sample, the excitation beam is completely absorbed by a thin surface layer of solution. As the NH_4NO_3 concentration decreases, the beam penetration depth into the sample increases, yielding a larger sampled volume. The number of irradiated molecules therefore remains constant

even as the concentration decreases by 4 orders of magnitude, resulting in very similar 1044 cm^{-1} band measured Raman intensities over a large concentration range.

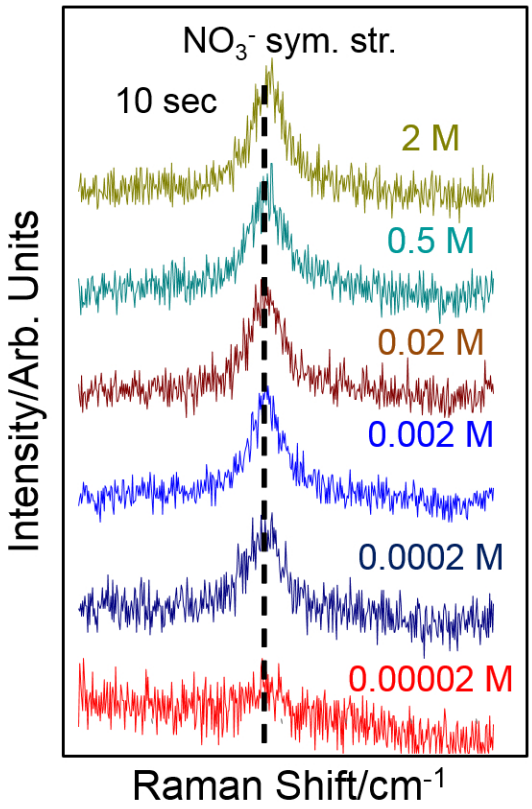

Figure 1.21 – 2.2 m standoff 213 nm UVRR spectra of aqueous NH_4NO_3 solutions at different concentrations in a 1 cm path length cuvette. Spectra were accumulated for 10 sec. Figure adapted from Bykov *et al.*[197]

1.6 Motivation for Deep UV Diffracting Photonic Crystal Development

Portions of Chapter 1.6 were previously published in the *Journal of Raman Spectroscopy* as K. L. Gares,* K. T. Hufziger,* S. V. Bykov, and S. A. Asher, "Review of Explosive Detection Methodologies and the Emergence of Standoff Deep UV Resonance Raman". J. Raman Spectrosc. 2016. 47(1): 124-141, where "*" denotes equal contribution, and is reprinted with permission. The

portions of this section reprinted below were originally prepared by K.T.H with the assistance of S.A.A.

The goal of this dissertation work was to develop photonic crystals as wavelength selection optical devices that would enable deep UV spectral imaging for trace explosive detection purposes. Spectral imaging techniques are powerful because they can be used to map the locations analyte of interest on the surface of an object.[12] Spectral images can be measured using either raster-scan or wide-field imaging methods.[199] In the raster-scan method, a focused laser sequentially illuminates a number of small spatial regions across the surface of the sample. Raman spectra are measured at each spatial region, and a hyperspectral image, which depicts the spatial variation in sample chemistry, can be formed from the large set of individual raster-scanned spectra. The major disadvantage of raster scanning is that large numbers of individual spectra must be measured to achieve high image resolution or to image large spatial areas. The number of spectra required depends on the size of the surface and the desired spatial resolution, which can result in extremely long accumulation times on the order of hours for images with large numbers of pixels.[200]

Alternatively, wide-field imaging instruments can be utilized to collect spatially resolved spectral information from an arbitrarily large region of the sample surface all at once. Instead of utilizing a focused laser beam, an expanded beam is used to illuminate a large spatial area of the sample surface.[12] In this case, in a typical wide-field experiment a spectrally narrow portion of the overall Raman spectrum is selected and its intensity is measured at each point in the irradiated area of the surface simultaneously. Wide-field imaging instruments typically utilize a wavelength selection device to select the narrow spectral region to be detected by a CCD camera. Liquid crystal tunable filters (LCTFs), acousto-optic devices, and dielectric filters are traditionally used as the wavelength selection optics in wide-field imaging spectrometers because they can select

spectrally narrow wavelength spectral intervals and are readily wavelength tunable.[12] By tuning the wavelength transmitted by these devices and collecting a wide-field image at each wavelength, a hyperspectral image can be formed that details the spatial variation in sample surface chemistry, similar to that obtained via the raster-scan method discussed above.[35,36,34] Alternatively, fiber optic arrays can also be coupled to a traditional dispersive spectrographs and used for wide-field imaging.[12,201]

One benefit of wide-field imaging techniques is that they can improve hyperspectral image S/N under conditions where the excitation power is not limiting, which can be used to reduce the time required to complete a measurement.[13, 199, 202] It is also possible to further reduce measurement time in wide-field imaging techniques by only collecting a limited number of spectral images at a limited number of spectral regions of interest, while ignoring spectral regions that are not expected to contain information of interest. In general, utilizing techniques to maximize measurement S/N are beneficial because in addition to shorter measurement times, high S/N allows for increased standoff distances and lower detection limits. All three of these parameters are extremely important to consider when designing instrumentation for field use, where extremely sensitive, fast performance is desired and necessary.

As discussed in Chapter 1.5.3, it is necessary to use deep UV excitation to enable resonance Raman enhancement, thereby maximizing the number of Raman scattered photons generated by the sample and improving the likelihood of detecting extremely thin, trace samples of explosives. However, development of wide-field Raman imaging spectrometers for use with deep UV excitation is impeded because the wavelength selection devices discussed above do not function in the deep UV, likely because materials used in their manufacture absorb light in this spectral

region. To create a wide-field imaging spectrometer in the deep UV spectral region, a wavelength selection device that functioned in the deep UV needed to be developed.

Directly prior to the start of the dissertation work described in the following chapters, the Asher research group demonstrated photonic crystals composed of highly charged monodisperse silica nanoparticles that diffracted narrow wavelength intervals of deep UV light.[15, 203] In that work, Wang *et al*. demonstrated the use of these deep UV diffracting PCs as Rayleigh rejection filters for 229 nm excited deep UV Raman measurements. In this dissertation work, we further developed these photonic crystal optics in the visible and deep UV spectral regions, demonstrating for the first time their use in wide-field imaging spectrometers. In Chapter 2.0, we describe our development of a novel, proof of concept wide-field Raman imaging spectrometer utilizing visible excitation to validate our spectrometer design. In Chapter 3.0, we utilized the knowledge acquired during that work, along with additional improvements in deep UV photonic crystal fabrication and characterization, to develop the first standoff deep UV wide-field Raman imaging spectrometer that we utilized to detect and image 10 $\mu g/cm^2$ quantities of explosives from 2.3 m away. We then developed the first mechanically robust, solvent-less deep UV diffracting inverse opal photonic crystals to improve the lifetime and durability of these photonic crystal wavelength selection optics, described in detail in Chapter 4.0.

2.0 Chapter 2: Raman Hyperspectral Imaging Spectrometer Utilizing Crystalline Colloidal Array Photonic Crystal Diffraction

This chapter was previously published in the journal *Applied Spectroscopy* as K. T. Hufziger, S. V. Bykov, and S. A. Asher, "Raman Hyperspectral Imaging Spectrometer Utilizing Crystalline Colloidal Array Photonic Crystal Diffraction". Appl. Spectrosc. 2014. 68(11): 1219-1223, and is reprinted with permission. K.T.H. collected and analyzed the data with the assistance of S.V.B. This manuscript was prepared by K.T.H. with the assistance of S.V.B and S.A.A.

2.1 Introduction

Hyperspectral imaging is a powerful technique because it determines the spatial dependence of the sample chemical composition.[12, 204, 205] The spectrum of each pixel in a hyperspectral image is encoded with the sample surface chemical composition. This information can be used for characterizing pharmaceutical tablets,[206] determining food quality,[207,208] atmospheric monitoring,[209] and standoff detection of analytes.[210] Hyperspectral images have been measured for reflectance,[211] fluorescence,[212] infrared absorbance,[213] and Raman spectral techniques.[214]

Raman spectroscopy is well suited to identifying chemical species because Raman spectra are molecular fingerprints. Raman spectral bands contain vibrational information that details molecular composition and molecular environment.[23] Raman imaging spectrometers can utilize either mapping techniques or wide-field imaging. Mapping instruments utilize a focused laser

beam and a precision sample translation stage.[169,215] To create an image, the laser is rastered over the sample surface while collecting Raman scattered light at each desired position. The collected light at each position is dispersed by a traditional Raman spectrometer. Raman spectrometers typically use double or triple monochromators to remove the intense Rayleigh scattered light. While these systems provide excellent spectral resolving power they are often large, heavy, and have poor throughput.[44] The consequence is that long integration times and high laser powers must be used to achieve sufficient signal-to-noise. The resulting accumulation times for rastered Raman images can be extremely long depending on the desired spatial resolution and the sample size.

Alternatively, wide-field instruments utilize a broad laser beam and the scattered light is simultaneously collected from a large surface area.[216] Rather than dispersing the collected light with a diffraction grating, these instruments typically utilize thin-film band-pass filters,[36] acousto-optic filters,[35] or liquid crystal tunable filters[34] to select a narrow wavelength Raman spectral region for imaging on a CCD camera. The advantage of this approach is that narrow spectral Raman images are created of the entire sample surface, greatly decreasing the total time required to generate the hyperspectral image.

In previous work we pioneered the use of crystalline colloidal array (CCA) photonic crystals as spectral dispersion optical devices for use as Rayleigh rejection filters in Raman spectrometers.[15, 16, 217-219] More recently, there have been additional studies on the utility of using photonic crystals to replace traditional diffraction gratings.[203, 220, 221] In this work, we use photonic crystals for the first time as the wavelength selection element of a wide-field Raman imaging spectrometer to diffract narrow spectral regions of light.

2.2 Experimental

2.2.1 Synthesis of Monodisperse Polystyrene Nanoparticles

Polystyrene nanospheres were synthesized using a modification[222] of the previous method of Reese *et al*.[59] A 500 mL jacketed Kontes reaction vessel was temperature controlled by a Thermo Neslab RTE 740 recirculator and stirred by using a Caframo BDC6015 overhead stirrer connected to a Teflon coated stir rod.

Styrene (Sigma Aldrich) was passed through a column containing 50 mL of aluminum oxide to remove the butylcatechol inhibitor. The ionic comonomer 3-allyloxy-2-hydroxy-1-propanesulfonic acid (COPS-1), the charged surfactant dihexyl sulfosuccinate (MA-80-1), and ammonium persulfate were acquired from Sigma Aldrich and used as received. Sodium bicarbonate was acquired from JT Baker and used as received. Nanopure water was generated by a Barnstead purification system.

A typical synthesis for the monodisperse 105 nm diameter polystyrene spheres is as follows. 0.348 g sodium bicarbonate and 275 mL nanopure water were added directly to the reaction vessel that was fitted with an addition funnel, a Teflon stir rod, a nitrogen purging inlet, and a reflux condenser. The stirring rate was set to 60 RPM and the solution was degassed for 30 min with N_2. 3.433 g MA-80-1 was dissolved in 5 mL nanopure water and added to the reactor, allowing 10 min of degassing after addition. 115 mL styrene was transferred to an addition funnel that was previously wrapped in aluminum foil to prevent photopolymerization. The styrene was purged with N_2 for 30 min. After purging, the stir speed was increased to 350 RPM and the reactor brought to a temperature of 50 °C. The styrene monomer was then added at a rate of ~0.1 mL / sec. Five min after completion of styrene addition, 6.282 g COPS-1 was added, and the

temperature increased to 70 °C. 1.562 g ammonium persulfate was dissolved in 5 mL nanopure water and injected to initiate the reaction. After allowing the reaction to proceed for two hours, an additional 1.043 g COPS-1 was injected into the reactor, followed 5 min later by another 1.015 g ammonium persulfate dissolved in 2 mL nanopure water. The reaction was allowed to proceed for another hour before being cooled to 50 °C under stirring. The particle dispersion was then filtered through previously boiled glass wool.

The mixture was then dialyzed using either 14,000 D MWCO regenerated cellulose tubing (Sigma Aldrich) or 1,000 kD MWCO cellulose ester tubing (Millipore) against nanopure water for two weeks. Following dialysis, the polystyrene colloidal dispersion was stored in contact with cleaned AG-501-X8 (Bio-Rad) mixed bed ion exchange resin.[223] The colloidal particle concentration was varied by adding or removing water. Care needs to be taken when increasing the concentration to avoid aggregation. To increase the colloid concentration, the particles were placed in 100 kD MWCO regenerated cellulose centrifugal filters (Millipore Amicon) and spun at 2000 *g* to slowly draw water from the sample.

2.2.2 Characterization Techniques

Diffraction of the colloidal array was measured using a Cary 5000 UV-Vis-NIR absorption spectrometer. Zeta potentials were measured using a Malvern Nano ZS90 Zetasizer. Particle sizes were measured using a FEI Morgagni 268 80 kV transmission electron microscope (TEM) by placing 10 μL of the dilute colloidal dispersion on Formvar coated copper grids (01814-F, Ted Pella) and evaporating to dryness. 100 spheres were measured via Image J (NIH) in order to determine the particle monodispersity.

2.2.3 Raman Instrumentation

A Renishaw InVIA Raman microscope utilizing 488 nm excitation was used to measure the Raman spectrum of Teflon. All imaged samples were excited with ~300 mW 488 nm light from a Coherent Industries Innova 90C-A6 Argon ion laser. An Ocean Optics HR4000 spectrometer was used to record the diffracted Raman spectra by focusing the light directly into its entrance slit. Raman images were collected by a Princeton Instruments PyLoN 400 B back illuminated 1340 x 400 pixel CCD camera, with a pixel size of 20 x 20 μm. Raman image exposure time was 5 seconds. Laser power was measured using a Gentec TPM-300 power meter.

2.3 Results and Discussion

2.3.1 Photonic Crystal Diffraction

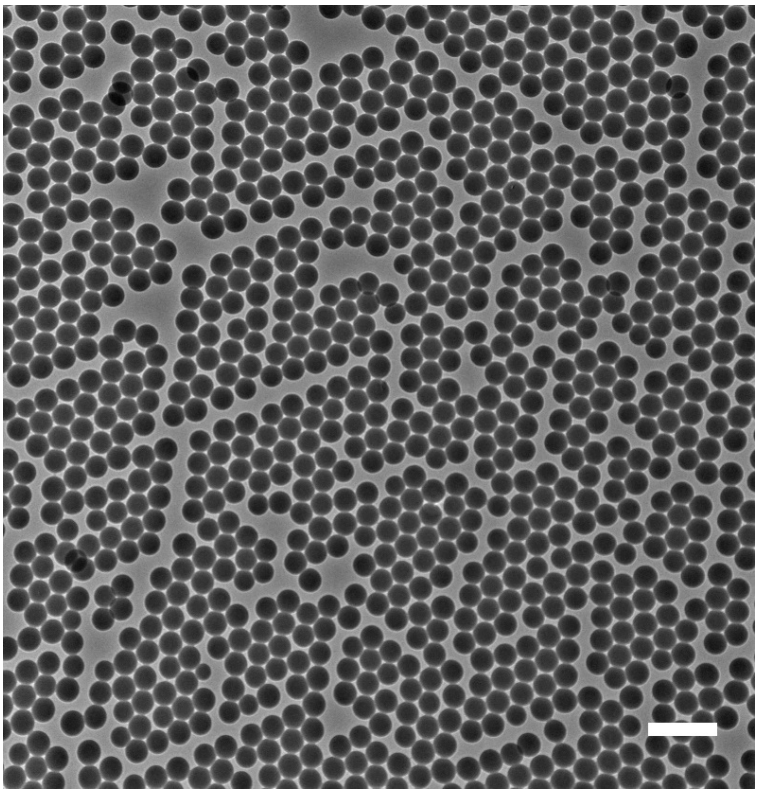

Figure 2.1 – TEM micrograph of monodisperse 102.7 ± 4.1 nm diameter polystyrene nanospheres. Scale bar represents 300 nm.

We utilized 102.7 ± 4.1 nm diameter polystyrene spheres that had a zeta potential of -81.8 mV at pH 5 (Figure 2.1). This surface charge derives from thousands of negatively charged sulfonate groups from the ionic comonomer COPS-1. These highly charged spheres repel each other and self-assemble in low ionic strength solutions into face centered cubic (FCC) crystals that diffract light according to Bragg's Law (Equation 2.1).[224]

Equation 2.1 $$m\lambda_0 = 2nd\,sin(\theta)$$

where m is an integer describing the order of diffraction, λ_0 is the wavelength of light in vacuum, n is the refractive index of the system, d is the diffraction plane spacing, and θ is the glancing angle. The value of θ depends upon any refraction for light entering the photonic crystal. For any plane spacing d, only one narrow wavelength band efficiently diffracts at each incidence angle θ.[225] Other wavelengths not meeting the Bragg condition transmit through the array except for small reflections from the windows enclosing the photonic crystal.

Polystyrene particle self-assembly into photonic crystals occurs readily for particle weight fractions from 2 to 15%. The lattice spacing d can be calculated for any desired plane for an FCC crystal of known particle concentration.[226] The diffraction wavelength maximum can be calculated at any incidence angle.[96]

The photonic crystal was contained between two 2" diameter quartz plates separated by a 130 μm thick Parafilm spacer. The input window (Thor Labs BSF2550) was wedge shaped to reflect light out of the diffraction plane. The colloidal particle dispersion was injected into the cavity between the plates, where it immediately assembled into an FCC crystal resulting in bright iridescence. The photonic crystal used here diffracts a narrow ~9 nm FWHM wavelength band. As the photonic crystal is rotated to achieve different incidence angles, different narrow wavelength bands diffract (Figure 2.2). The bandwidth depends on the CCA ordering and particle diameter. Smaller particles, thinner crystals and better ordered FCC arrays result in narrower diffraction.[96]

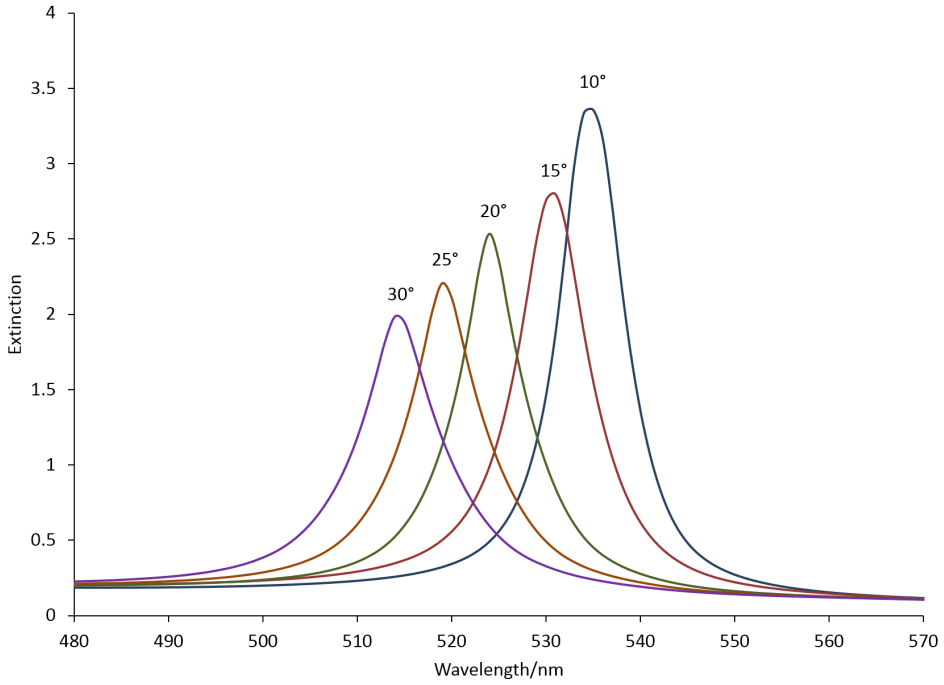

Figure 2.2 – Incidence angle dependence of diffraction by a 102.7 nm diameter polystyrene particle photonic crystal measured using an absorption spectrometer. Incidence angles measured relative to the input plate.

The diffraction efficiency decreases for larger incidence angles due to the decreased diffraction efficiency of π polarized light.[227] In addition, charged impurities can screen the electrostatic repulsive force between particles. This results in disorder that increases the diffraction bandwidth. To maximize diffraction efficiency and minimize bandwidth we used low ionic strength solutions and carefully cleaned quartz cells.

We determined the diffraction efficiency by directing a 514 nm Argon laser beam onto the photonic crystal and measuring the diffracted beam intensity with a power meter. Diffuse scattering due to phonon modes and crystal defects are the primary sources of diffraction light loss.[96,126] A 0.5 cm aperture was placed before the detector to reject some of the diffusely scattered light. We measured an 70% diffraction efficiency for 514 nm light.

2.3.2 Spectrometer Design

The sample was excited by a 488 nm laser beam (Figure 2.3) and the backscattered light was collected and collimated by plano-convex lens L1. A thin-film interference long-pass edge filter (Semrock) removed most of the Rayleigh scattered light. Aperture A1 limits the beam width that illuminates the photonic crystal. The Raman imaging spectrometer utilizes our photonic crystal to select and diffract a narrow wavelength spectral region. We chose angle θ_1 to select the wavelength of the diffracted spectral region.

Mirror M1 directs the diffracted beam towards mirror M2 which directs it towards either the Ocean Optics spectrometer to measure the diffracted Raman spectrum, or to lens L3 to focus the collimated narrow wavelength band to form an image on the Pylon CCD camera.

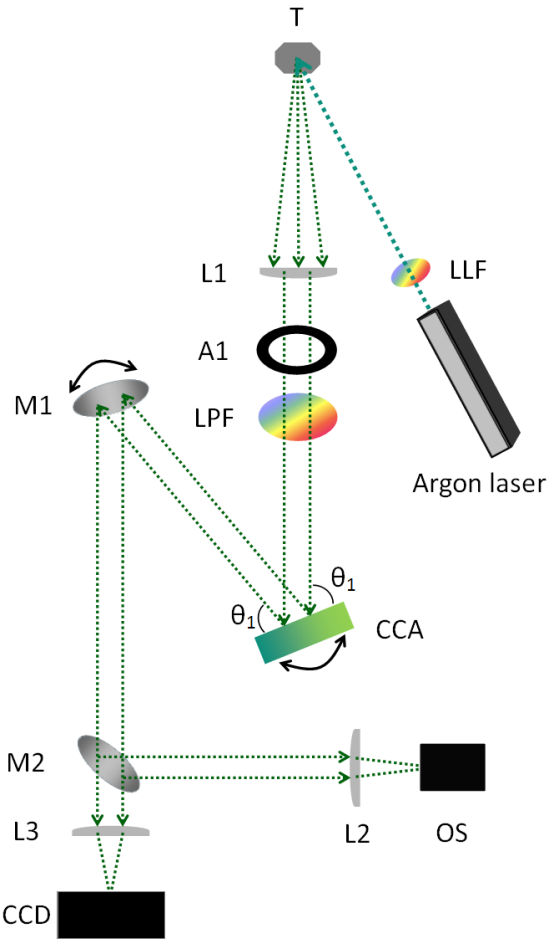

Figure 2.3 – Diagram of the Raman imaging spectrometer where an Argon laser produces 488 nm light. LLF is a 488 nm laser-line filter, T is the Teflon sample, L1 is a plano convex collection lens, A1 is a 1.5 cm diameter aperture, LPF is a long-pass edge filter used to remove the Rayleigh scattered light, CCA is our crystalline colloidal array photonic crystal mounted on a rotation stage, M1 is a rotatable planar mirror, and M2 is a planar mirror used to direct the diffracted light towards either of the plano convex lenses, L2 or L3. CCD is the Pylon CCD camera and OS is the Ocean Optics spectrometer. The lens focal lengths are $f_{L1} = f_{L2} = 10$ cm, and $f_{L3} = 30$ cm.

2.3.3 Raman Diffraction

We used a block of polytetrafluoroethylene (Teflon) as a sample. Figure 2.4a shows the Raman spectrum of Teflon measured using a Raman microscope utilizing 488 nm excitation. Teflon shows strong lines at 731, 1216, 1300, and 1380 cm^{-1} as well as a background likely due to fluorescence. We selected the triplet centered at ~1300 cm^{-1} (522 nm) for imaging, and angle tuned the photonic crystal to diffract a band of light centered at 522 nm.

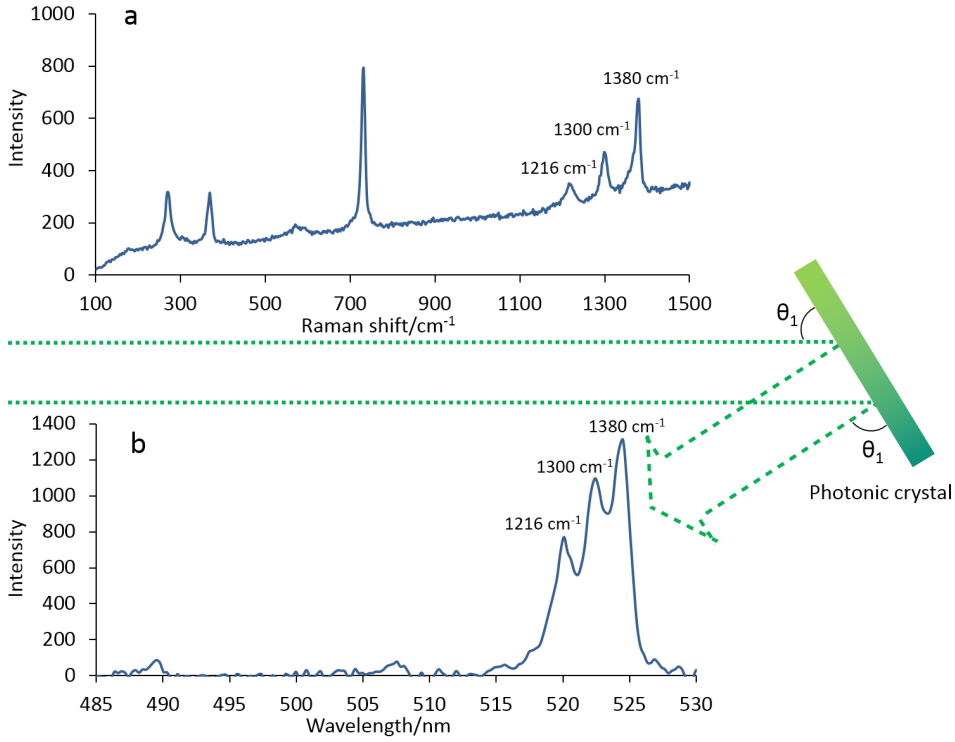

Figure 2.4 – (a) Teflon Raman spectrum measured with the Raman microscope. (b) Teflon Raman spectrum of light diffracted by the photonic crystal measured by the Ocean Optics spectrometer. Both samples were excited with 488 nm light.

Figure 2.4b shows the Raman spectrum of the diffracted light that was focused onto the slit of the Ocean Optics spectrometer. We clearly see the triplet of Teflon bands centered at 522 nm. Most of the light below 517 nm and above 527 nm transmits through the photonic crystal except for a small amount scattered by the polystyrene spheres and reflected by the quartz cell surfaces.

2.3.4 Raman Imaging

Our Raman imaging measurements used a Teflon sample that contained a ~1 mm diameter circular depression filled with finely ground NaCl (Sigma Aldrich) (Figure 5a). NaCl was used because it shows no Raman bands in the ~1300 cm^{-1} spectral region. The sample surface was illuminated by a ~2 mm diameter 488 nm laser beam.

The Raman light diffracted by the photonic crystal was imaged by lens L3 onto the CCD, resulting in a Raman image of the sample surface. Lens L3 magnified the image on the CCD by ~3 to increase image resolution. Due to the Teflon Raman bands centered at ~1300 cm^{-1}, the Teflon surface appears bright, while the NaCl filled center is dark (Figure 5b).

Our photonic crystal can be angle tuned to select and image different narrow wavelength spectral regions. These images can be accumulated to form a hyperspectral data set that contains a Raman spectrum associated with each pixel. The wavelength range of our spectrometer is limited by the useful spectral range of the photonic crystal which can be used between incidence angles of 5 to 40°. This enables diffraction measurements over a 1900 cm^{-1} region of the visible spectrum between 490 - 540 nm for the photonic crystal used here. Incidence angles greater than 40° are less useful because they show simultaneous diffraction from higher Miller index FCC planes.[126]

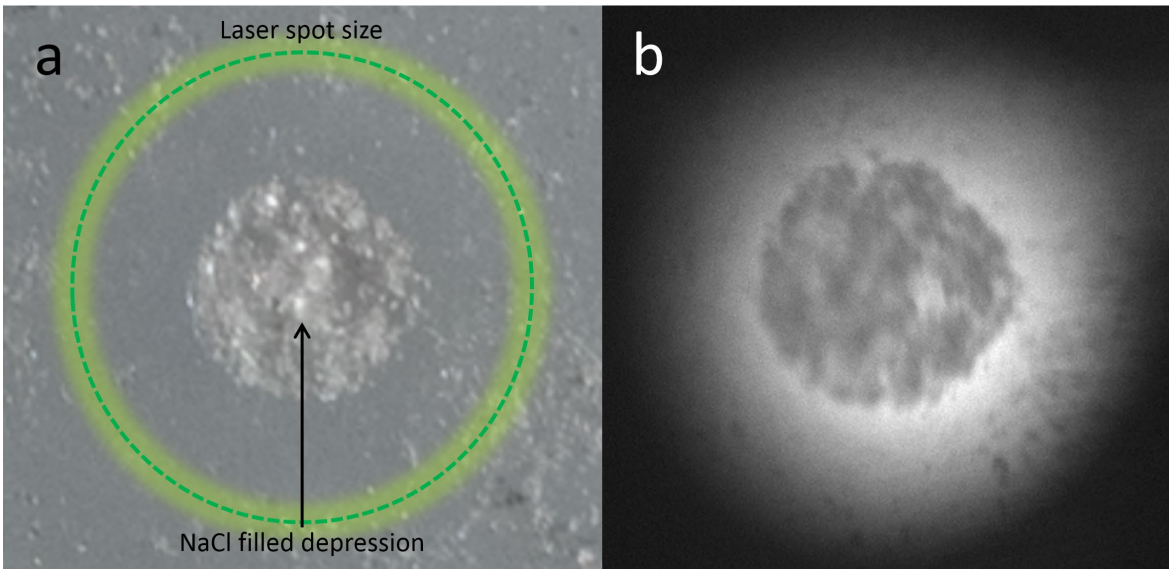

Figure 2.5 – (a) Photograph of a Teflon surface with a ~1 mm diameter NaCl filled depression. (b) Raman spectral image of 1200 – 1400 cm^{-1} light diffracted by the photonic crystal showing the NaCl depression. Accumulation time for the Raman image was 5 seconds.

The diffraction bandwidth calculated by dynamical diffraction theory[228] for 102.7 nm spheres is ~10 nm at 10° incidence, in excellent agreement with our measured value (Figure 2). The photonic crystal diffraction wavelength bandwidth utilized here is still relatively broad. It should be significantly narrowed below 10 cm^{-1} for maximum resolution Raman imaging. The diffraction bandwidth can be decreased by decreasing the particle diameter,[126] by increasing particle size monodispersity, by increasing the array ordering, by decreasing the crystal thickness, and by decreasing the difference in refractive index between the particles and the medium. The polystyrene particles used here are suitable for visible and infrared diffracting[49] photonic crystals, but materials such as silica must be used for ultraviolet light diffraction since polystyrene absorbs below 350 nm.[15]

Work is now ongoing to decrease the diffraction bandwidth of our photonic crystals. We recently demonstrated that 50 nm diameter silica nanosphere photonic crystals diffract ~4 nm

FWHM spectral regions in the 230 nm UV spectral region, enabling the construction of a UV Raman photonic crystal imaging spectrometer.[15]

A major advantage of our photonic crystal imaging Raman spectrometer is its relative simplicity and efficiency compared to traditional grating spectrometers. We calculate that with the use of anti-reflection coated lenses and dielectric mirrors the optimum throughput of our spectrometer would be mainly limited by the diffraction efficiency of the photonic crystal which we measure to be 70%. Our photonic crystals can also be utilized as Rayleigh rejection filters in low cost Raman spectrometers.

2.4 Conclusion

We demonstrate a prototype Raman imaging spectrometer that utilizes a photonic crystal consisting of an FCC array of charged polystyrene spheres to diffract a narrow spectral region. Focusing this diffracted Raman light onto a CCD camera generates a Raman image that can be used to determine the surface chemical composition. We are presently working on increasing the spectral resolution and are extending the utility of this approach to the deep UV spectral region.

2.4.1 Acknowledgements

This work was supported by the ONR N00014-12-1-0021 grant.

3.0 Chapter 3: Ultraviolet Raman Wide-field Hyperspectral Imaging Spectrometer for Standoff Trace Explosive Detection

This chapter was previously published in the journal *Applied Spectroscopy* as K. T. Hufziger, S. V. Bykov, and S. A. Asher, "Ultraviolet Raman Wide-field Hyperspectral Imaging Spectrometer for Standoff Trace Explosive Detection". Appl. Spectrosc. 2017. 71(2): 173-185, and is reprinted with permission. K.T.H. collected and analyzed the data with the assistance of S.V.B. This manuscript was prepared by K.T.H. with the assistance of S.V.B and S.A.A.

3.1 Introduction

The increasing use of explosive devices in terrorist attacks has dramatically increased the need for sensitive standoff explosive detection instruments that can be utilized to screen for trace explosive residues that may indicate the presence of explosive threats.[229,2] There is intense interest in detection of explosives at trace concentrations such as those present in explosive-laced fingerprints, on vehicle panels or other surfaces contaminated by explosive residues, and in vapors surrounding buried landmines.[4, 5, 171, 179] Trace explosive detection is challenging because explosives typically have low vapor pressures, making vapor detection difficult.[2,230] In addition, explosives often quickly photolyze when exposed to near-UV irradiation from sunlight, as well as from deep UV irradiation during spectroscopic measurements.[31-33, 231, 232] Any detection methodology must be able to detect different classes of explosives that have widely varying chemical structures.

We have been developing deep UV resonance Raman spectroscopy for standoff trace explosive detection. We have determined deep UV Raman spectral signatures, cross sections, and the UV photochemistry of many explosives.[26, 29, 31, 32] We have also developed new spectroscopic instrumentation, as well as novel, compact UV laser excitation sources.[197] We recently reviewed advances in UV Raman standoff methods and compared their utility to existing methodologies that are currently used to detect and screen for trace explosives.[229] These include canine olfaction, ion mobility spectrometry, fluorescence quenching devices, and colorimetric assays.[8, 136, 146] The key limitation of these other techniques is the necessity for humans, canines, or instrumentation to be in close proximity to the objects being screened. Laser-based spectroscopies are the only currently viable means to detect explosives from safe standoff distances.

Raman spectroscopy is an inelastic light scattering technique that is well suited for explosive detection because measured Raman spectra can serve as molecular fingerprints.[26,21, 23, 233] In a typical Raman measurement, a monochromatic excitation source, usually a focused laser, excites a small area of a sample. The vibrational modes of molecules in the sample inelastically Raman scatter light, which gives rise to light shifted from the excitation frequency by the frequency of the molecular vibration. The Raman scattered light is collected, dispersed by a spectrograph, and measured using a CCD detector. Visible wavelength Raman spectroscopy has been previously used for standoff detection by exciting distant samples with a laser and collecting the Raman scattered light with a telescope.[25,24]

Raman imaging methodologies have also been utilized to characterize the spatial chemical composition of sample surfaces.[12] Raman imaging instruments can be broadly differentiated by whether they involve raster-scanning or wide-field illumination.[169] Raster-scanning Raman imaging instruments typically either translate a focused laser and collection optics across a

stationary sample or utilize scanning stages that precisely move the sample in front of a stationary focused laser. Raman spectra are measured at discrete points on the sample utilizing a traditional Raman spectrometer.[199] The collected spectra can be assembled to produce a hyperspectral Raman image that depicts the Raman spectra of the sample as a function of position.[234]

In cases where the available laser beam power is not limiting, wide-field imaging instruments can provide hyperspectral images with dramatically increased S/N compared to raster-scan instruments.[13] In wide-field Raman instruments, a defocused laser beam illuminates a large region of the sample, and the Raman scattered light is simultaneously collected from the entire illuminated area. The Raman scattered light is analyzed by a wavelength selection device (WSD) that selects a narrow wavelength spectral region of interest to form a wide-field Raman image of the entire sample surface. In the simplest case, the WSD selects a spectral region containing only a single Raman band of the analyte. In this case, the Raman image intensity details the spatial distribution of the analyte.[170,14]

Typically, the WSD is then tuned to image additional spectral regions, enabling the collection of a hyperspectral Raman image of the sample. In our previous work, we demonstrated the first use of a photonic crystal (PC) as a WSD to construct a visible wide-field imaging spectrometer with 488 nm excitation.[170] We pioneered and have extensively studied PCs composed of highly charged, self-assembling nanospheres that diffract light according to Bragg's Law.[217,235] We have utilized these PCs as visible Rayleigh rejection filters for Raman measurements and for numerous sensing applications including detection of small molecules, proteins, and micro-organisms.[16, 44, 236-239] Other groups have developed near IR and visible wavelength Raman wide-field imaging spectrometers by utilizing liquid crystal tunable filters (LCTF), acousto-optic tunable filters (AOTF), and bandpass filter WSDs .[199,35]

Many previous standoff Raman explosive detection instruments utilized visible excitation due to the availability of high performance visible optics and filters, efficient detectors, and high power visible laser sources.[25,24,184,240] The major limitation of visible Raman for trace explosive detection derives from the weak Raman cross sections that limit detection sensitivity. Furthermore, fluorescence caused by visible excitation can severely degrade Raman spectral S/N and visible excitation power must be severely constrained to maintain eye safety for detection in the field.

There is great interest in utilizing deep UV excitation for standoff explosive detection.[229,197,190, 194, 241] Deep UV excitation (< 250 nm) has significant advantages for Raman standoff trace explosive detection. Raman scattering intensity has a ν^4 dependence on excitation frequency, yielding greater Raman intensities as the excitation wavelength decreases.[21] Excitation at < 250 nm within the explosives' electronic absorption bands results in resonance Raman enhancements of up to 10^6, significantly improving detection sensitivity.[29,26,10] Sample luminescence that notoriously degrades spectral S/N for visible and near IR Raman experiments occurs outside the Raman spectral region when deep UV excitation is utilized, improving sensitivity.[188] In addition, the ocular mean permissible exposure (MPE) set by ANSI for deep UV light is much higher than for visible excitation, enabling the use of higher laser power eye-safe deep UV instruments.[242,189] Thus, the sensitivity and selectivity of Raman instruments for explosive detection is dramatically increased for deep UV excitation, especially for trace samples likely to be encountered in the field.[229,33,26,197,27]

The primary challenge for deep UV wide-field imaging instrumentation is that until this work, there were no WSDs that functioned in the deep UV spectral region. We recently invented the first deep UV diffracting PC and demonstrated its use as a Rayleigh rejection filter for 229 nm

UV Raman experiments.[15] We developed a modified Stöber synthesis to prepare highly charged, monodisperse ~47 nm diameter silica nanoparticles. These particles self-assembled in solution to produce a PC that diffracted a narrow deep UV spectral region. We utilized this deep UV diffracting PC as a 229 nm Rayleigh rejection filter in a Raman measurement of Teflon, where the Stokes shifted Teflon Raman bands transmitted through the PC to be dispersed by the spectrograph. In the present work, we demonstrate the use of a silica nanoparticle PC as a WSD to construct the first deep UV standoff wide-field Raman imaging spectrometer for trace explosive detection.

3.2 Experimental

3.2.1 Monodisperse Silica Nanoparticle Synthesis and Functionalization

Monodisperse silica nanospheres were synthesized by using a scaled up regrowth method first described by Hartlen *et al*.[67] Briefly, 99.5 mL nanopure H_2O (Thermo Scientific Barnstead) was added to a jacketed 500 mL reactor (Kontes) connected to an ethylene glycol bath (Thermo Scientific Neslab RTE 740) for temperature control. The reactor was fitted with a Teflon agitator (Ace Glass 8090-08) attached to an overhead stirrer (Caframo BDC6015) set to 60 RPM and a reflux condenser. 0.1825 g L-arginine (Sigma Aldrich A5006) was dissolved in 39.0 mL nanopure H_2O and added to the reactor, followed by 12.0 mL cyclohexane (Fisher Scientific C556). After the reactor contents reached ~60 °C, 11.00 mL tetraethyl orthosilicate (TEOS, Sigma Aldrich 86578) was pipetted slowly down the reactor wall to prevent fast mixing with the aqueous layer, resulting in improved nanoparticle nucleation which increased the final particle monodispersity.[67]

The reaction was allowed to proceed for 20 hours before being cooled to room temperature. The resulting silica nanoparticle seed dispersion was 24.7 ± 2.8 nm in diameter.

Between each synthesis step, the nanoparticle dispersion was removed and the reactor was washed with ethanol and nanopure H_2O. To grow the silica nanoparticles to their final size, the entire nanoparticle seed dispersion was added to the reactor and stirring was restarted at 60 RPM. 490 mL nanopure H_2O was added, followed by 53 mL cyclohexane. The recirculator heated the reactor to ~55 °C, and 40.0 mL TEOS was pipetted slowly down the reactor wall. The reaction was allowed to proceed for 30 hours before cooling to room temperature.

The resulting 35.7 ± 2.9 nm nanoparticles were functionalized with 3-trihydroxylsilyl-1-propane sulfonic acid (THOPS, Gelest SIT 8378.3) following a procedure described by Wang *et al*.[15] The entire dispersion was added to the reactor, stirring was restarted at 60 RPM, 100 mL nanopure H_2O was added to the reactor, and the reactor heated to 70 °C. ~4 mL NH_4OH (Sigma Aldrich 21228) was added to 20.0 mL THOPS and the pH ~9 mixture was poured into the reactor. The reaction was allowed to proceed for 6 hours before cooling to room temperature.

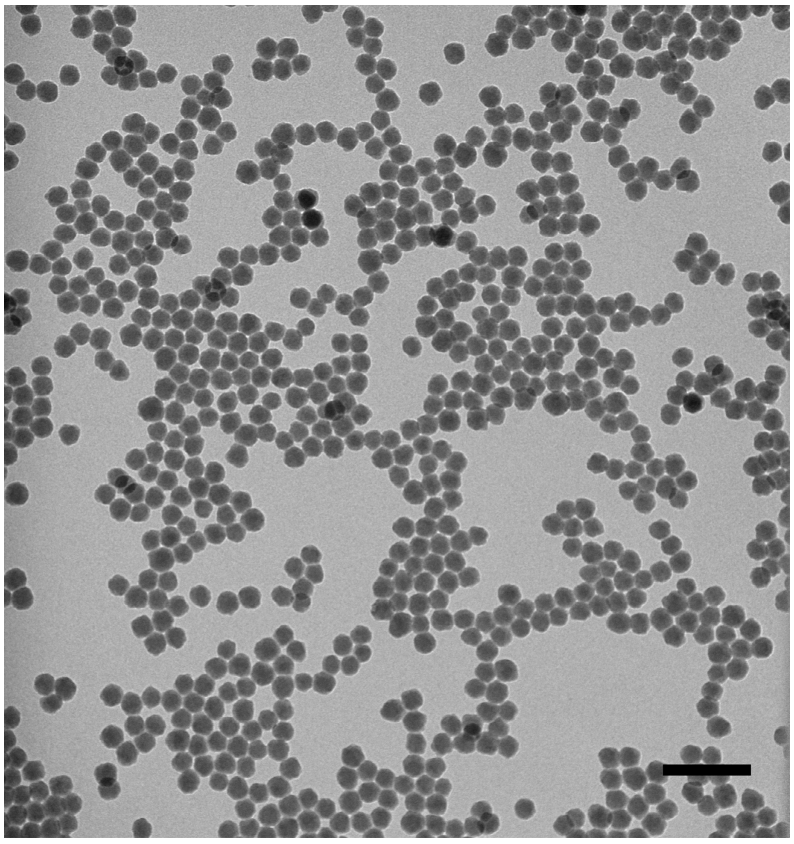

Figure 3.1 – Transmission electron micrograph of highly charged 35.5 ± 2.9 nm silica nanoparticles. Scale bar denotes 150 nm.

The dispersion was removed from the reactor and dialyzed (Sigma Aldrich D9652) against nanopure water for 3 days to remove unreacted species. Following dialysis, the dispersion was centrifuged at 18,000 *g* for at least one hour, the supernatant was removed, and the pellet re-dispersed in nanopure H_2O. Supernatant removal via centrifugation followed by redispersion was repeated 4 times before storing the final product over mixed bed ion exchange resin (Bio-Rad AG-501-X8 (D)) to remove any remaining ionic contaminants. The final nanoparticle size was measured to be 35.5 ± 2.9 nm by TEM (Figure 3.1). We measured a Zeta potential of -50.5 mV at pH 4.5.

3.2.2 Nanoparticle and Photonic Crystal Diffraction Characterization

Nanoparticle sizes were measured by pipetting dilute dispersions onto Formvar coated copper grids (Ted Pella, 01814-F). After air-drying, the grids were imaged using a transmission electron microscope (FEI Morgagni 268). At least 100 individual nanoparticles were measured via Image J (NIH)[243] to determine the particle size distribution. The Zeta potential of a diluted nanoparticle dispersion was measured using dynamic light scattering (Malvern ZS-90 Zetasizer, Smoluchowski approximation). Sample pH was monitored during Zeta potential measurements using pH strips (EMD Millipore ColorpHast 0-6 pH).

The transmission of UV light by the PC was monitored by using a UV-Vis-NIR absorption spectrometer (Varian Cary 5000). The PC was held by a 2" mirror mount (Newport GM-2) attached to a rotational stage (Newport 481-A) mounted on a breadboard placed within the spectrometer. The PC diffraction bandwidth was directly determined by measuring the angular dependence of the power of a weak 229 nm laser beam diffracted by the PC. The PC was mounted to a rotational stage (Newport 481-A) and illuminated by ~150 μW 229 nm continuous wave (CW) light generated by an intracavity frequency doubled Coherent Innova 300c FreD Ar ion laser.[244] The diffracted laser beam power was measured using a photodiode power meter (Thor Labs PM200 meter with a S120VC head) and fit to a Gaussian for further analysis (OriginPro).

3.2.3 Trace Explosive Sample Preparation

Drop-cast trace explosive samples were prepared on the surface of ~2.5 x 2.5 cm aluminum plates (McMaster-Carr, Multipurpose 6061 aluminum) that were first smoothed by a milling machine (Pitt Chemistry Machine Shop) followed by final polishing with fine grit sandpaper

(Norton P800). The aluminum plates were thoroughly washed with acetone, ethanol, and nanopure H_2O before being dried with a stream of N_2.

To prepare the drop-cast samples for Raman imaging, a 1.00 mL methanol solution containing 1.00 mg pentaerythritol tetranitrate (PETN, AccuStandard M-8330-ADD-2-10x) was evaporated using a gentle stream of N_2. The small crystals were dissolved in 50.0 μL spectroscopic grade acetone (Acros 16764-5000, >99%). 6.0 μL of a 20.0 mg/mL solution of NH_4NO_3 (AN, EM Science AX1315-1, >99%) in spectroscopic grade methanol (Fisher Scientific A408-1, >99%) was drop-cast onto a section of a clean aluminum plate. 6.0 μL of the PETN solution was drop-cast a short distance away. These droplets quickly evaporated to create two explosive films containing 760 μg/cm^2 AN and 920 μg/cm^2 PETN, respectively (Figure 3.6a and e). The total amount of explosive deposited in each film is 120 μg. ~100 μg PETN and AN were similarly drop-cast onto two separate, clean aluminum plates for Raman spectral analysis (Figure 3.6b and f). Microscope images (DinoLite Edge) were recorded of the samples prior to irradiation.

It is well known that solids migrate towards the edge of evaporating droplets, resulting in the formation of a "coffee-ring" where most of the solute becomes localized at the ring edge.[104,245] To increase film uniformity and surface coverage of these drop-cast explosive samples we utilized high vapor pressure solvents and small solution volumes that were deposited in multiple aliquots with drying in between to minimize coffee-ring formation.

In addition to these drop-cast samples, we also measured 10, 100, and 250 μg/cm^2 PETN and AN inkjet printed explosive samples on smooth aluminum substrates (ACT Test Panel Technologies) donated by the US Army Research Lab (ARL). Preparation of these samples is described elsewhere.[246] Inkjet printing offers several important advantages over drop-cast deposition. Inkjet printing enables reproducible deposition of droplets that are several orders of

magnitude smaller in volume than is possible using micropipettes, mitigating coffee ring formation.[245] Inkjet printing enables reproducible preparation of samples with well-defined explosive surface coverage via precise control of the volume, location, and number density of deposited droplets.

3.2.4 Raman Measurements

Trace explosive samples were excited by 229 nm light generated by an intracavity doubled Ar ion laser, described above.[244] A custom deep UV optimized spectrometer (Spex Triplemate) equipped with a CCD (Roper Scientific Spec 10) was utilized to collect solid state deep UV Raman spectra of the explosives (Figure 3.6b and f).[247] The solid state explosive samples were illuminated by a ~4.3 mW, 229 nm beam with a ~70 μm spot size and were spun during irradiation (Figure 3.6b and f). Raman spectra were scaled proportionally to the Raman cross sections of their most intense Raman bands (1044 cm^{-1} for NH_4NO_3 and the sum of the 1269 + 1289 cm^{-1} bands for PETN) after cosmic ray removal and calibration (Thermo GRAMS/AI 8.0) using solid state 229 nm Raman cross sections measured by Emmons *et al.*[27]

For Raman imaging experiments, the 229 nm beam was directed through two plano-convex microlens arrays (Edmund Optics 64-477) to generate a square, ~1.2 x 1.2 cm beam at the sample. The total incident laser power was measured by a photodiode power meter (Thor Labs PM200 meter with a S120VC head) to be ~6.5 mW after the final turning mirror at the sample during the Raman imaging measurements.

All Raman images are depicted in false color by utilizing WinSpec software (Princeton Instruments). The false color contrast range that determines the color of each pixel in the Raman image was set to be identical for all Raman images with the same accumulation time (i.e. all 30

sec Raman images have the same false color scale), enabling separate Raman images to be visually compared. Raman image false colors range from dark blue (low intensity) to bright red/white (high intensity). Laboratory lights were turned off during Raman image collection.

3.3 Results and Discussion

3.3.1 Photonic Crystal Diffraction

The low pKa sulfonic acid groups attached during THOPS functionalization of our monodisperse silica nanoparticles yields a high negative surface charge and a high ζ-potential of -50.5 mV at pH 4.5. We utilized these 35.5 ± 2.9 nm silica nanoparticles to fabricate PCs that diffract light in the deep UV spectral region (Figure 3.2). After thoroughly removing dissolved charged species from the nanoparticle dispersion, electrostatic repulsion between the highly charged nanoparticles caused self-assembly of a face centered cubic (FCC) crystal that diffracts light according to Bragg's Law (Equation 3.1).[170]

Equation 3.1 $$m\,\lambda = 2\,n\,d\,\sin\theta$$

where m is the diffraction order, λ is the wavelength of light in vacuum, n is the refractive index of the dispersion, d is the FCC (hkl) plane spacing, and θ is the glancing angle within the dispersion.[126] We utilize diffraction from the FCC (111) planes because their diffraction is highly spectrally separate from the higher Miller index planes. The FCC (111) interplanar distance is readily calculated from the nanoparticle number density.[226] Only one narrow wavelength spectral region will be diffracted by the FCC (111) planes for a specific incident angle of light on the PC (Figure 3.2). All wavelengths of light that do not meet the Bragg condition transmit through the

PC except for a small amount of light that is diffusely scattered by the nanoparticles and a small amount of light that is reflected from the surfaces of the fused silica cell that encloses the PC.

The front face of the PC cell is wedge shaped (Thor Labs BSF2550) in order to direct unwanted reflected light out of the optical plane of the imaging spectrometer (Figure 3.3). The cell was constructed by utilizing a partially melted ~120 μm thick Parafilm spacer to attach the wedged front face to a flat fused silica back plate. The highly charged nanoparticle dispersion was injected via a syringe through holes in the back plate. The nanoparticles immediately self-assemble to form the FCC PC where the (111) planes oriented parallel to the cell surfaces.

Angle tuning the PC relative to the incident light tunes the wavelength of the diffracted narrow spectral region. We previously demonstrated that ~47 nm diameter silica nanoparticles that diffract ~230 nm light at normal incidence show ~5 nm full width at half max (FWHM) transmission bandwidths when measured using our absorption spectrometer.[15] The measured PC diffraction bandwidth is governed by the particle light scattering, particle ordering, light incident angle, and light collimation. The narrowest diffraction occurs for normal incident angles.[44] We reduced the normal incidence *transmission* bandwidth by ~46% to ~2.7 nm FWHM (Figure 3.2) measured in the absorption spectrometer by reducing the nanoparticle diameter from ~47 nm in our previous work to 35.5 ± 2.9 nm here. Reducing the diffraction bandwidth increases the spectral resolution of the Raman imaging spectrometer, enhancing the ability to differentiate between analytes with closely spaced Raman bands.

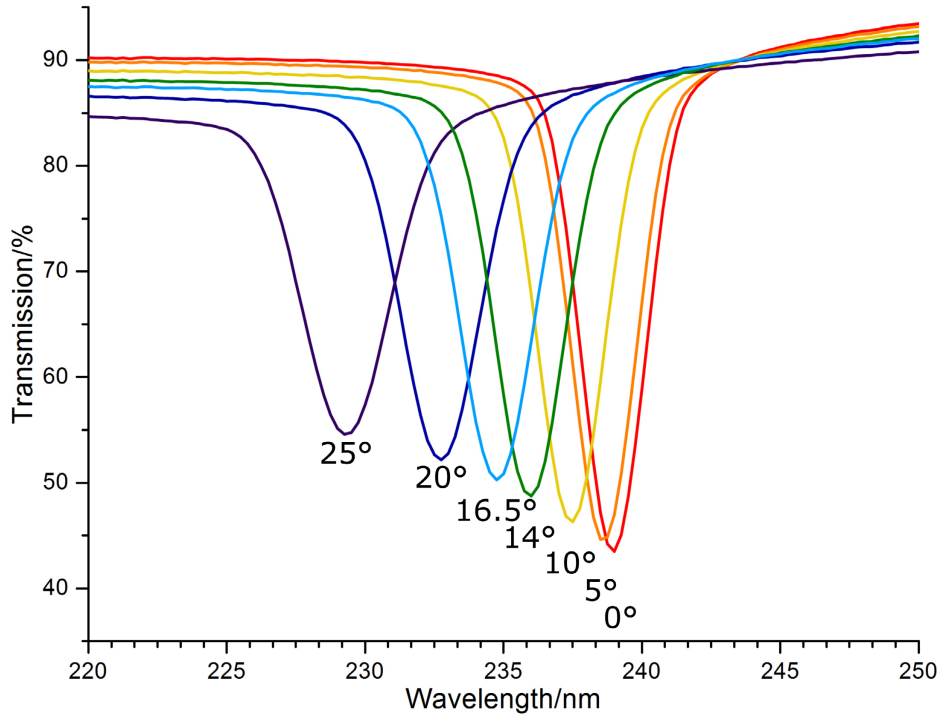

Figure 3.2 – 35.5 ± 2.9 nm silica nanoparticle PC transmission measured using an absorption spectrometer at various PC rotational angles.

Smaller nanoparticle diameters and increased FCC ordering narrows the transmission and diffraction bandwidths.[126,228,96] Smaller nanoparticles and nanoparticles with refractive indices closer to that of the surrounding medium decrease the nanoparticle light scattering. For an optically thick PC this allows a greater number of PC FCC planes to participate in diffraction, which narrows the diffraction spectral bandwidth.[126,228] Inhomogeneities in the nanoparticle spacings can derive from a lack of nanoparticle size and charge monodispersity, or result from the formation of small polycrystalline domains due to imperfect self-assembly. This can result in a distribution of FCC (111) interplanar spacings that can broaden the diffraction bandwidth.[126] Determining the relative contribution of each of these phenomena is difficult since it requires complex studies of the dependence of diffraction bandwidth on all of the relevant PC material parameters.

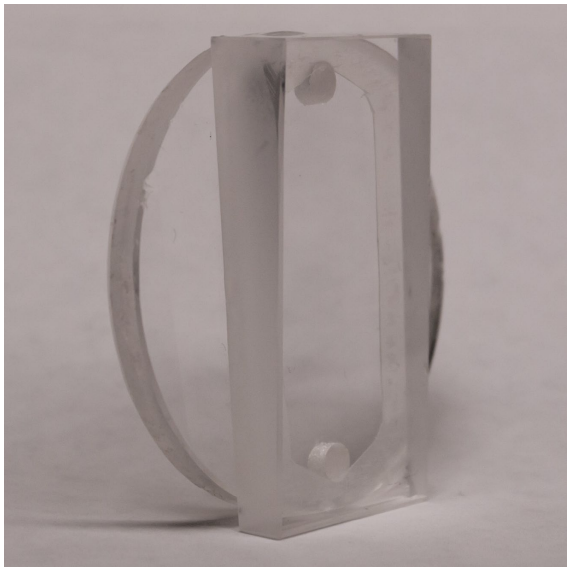

Figure 3.3 – Photograph of the PC cell. Highly charged, monodisperse nanoparticles are injected through the back plate into a cavity formed by a melted Parafilm spacer, where the particles self-assemble to form the deep UV diffracting PC.

The absorption spectrometer transmission measurements conveniently and quickly monitor the PC diffraction wavelengths and the transmission bandwidths for any incident angle. However, the PC diffraction bandwidths that determines the PC spectral imaging resolution are significantly narrower than the transmission bandwidths.[96] Furthermore, both the diffraction and transmission bandwidths are broadened for incident light that is imperfectly collimated, which results in a distribution of PC Bragg glancing angles. This phenomenon gives rise to an increased bandwidth for the transmission spectra measured by our absorption spectrometer which utilizes a non-collimated beam in the sample compartment.[15]

We directly measured the PC diffraction bandwidth by determining the angular dependence of the diffracted power of a 229 nm laser beam (Figure 3.4). Snell's Law was applied to the incident laser beam glancing angles measured in air to calculate the glancing angles within the PC,

after refraction through the quartz cell and into the PC (Figure 3.4a). A Gaussian fit depicted in blue (Figure 3.4a) was utilized to calculate the glancing angle for the maximum intensity of 229 nm diffraction (74.6°) and the angular FWHM bandwidth (Δθ, 0.94°). The refractive index of the dispersion (*n*) was calculated to be ~1.395 using the volume fraction of nanoparticles (2.9%), the nanoparticle refractive index (assumed to be that of fused silica at 229 nm, 1.521), and the refractive index of water (1.391).[227, 248, 249] If we treat the PC diffraction in the more complete dynamical diffraction limit we will find a more complex relationship between the diffraction angle and the refractive index.[96,250] Given the calculated PC refractive index, we can use Bragg's Law in the kinematic limit to calculate the d_{111} plane spacing utilizing the measured glancing angle for the maximum intensity 229 nm diffraction (Equation 3.2).

Equation 3.2 $$d_{hkl} = {229\ nm}/{2 * 1.395 * sin(74.6°)} = 85.2\ nm$$

We then utilized Bragg's Law to relate the angular bandwidth, Δθ, to the wavelength bandwidth, Δλ (Equation 3.3 and Equation 3.4). The limiting diffraction band glancing angles (FWHM, θ_L and θ_H) are calculated by taking the difference between the center glancing angle and half of the angular FWHM (74.6 ± 0.47°). The wavelength difference (Δλ) between incident light at θ_L and θ_H (Equation 3.4) yields the FWHM diffraction bandwidth in *nm*.

Equation 3.3 $$\lambda = 2 * 1.395 * 85.2\ nm * sin(\theta) = 238 * sin(\theta)$$

Equation 3.4 $$\Delta\lambda = |[238sin(\theta_L)] - [238sin(\theta_H)]| = |[238sin(74.1)] - [238sin(75.1)]| = 1.0\ nm$$

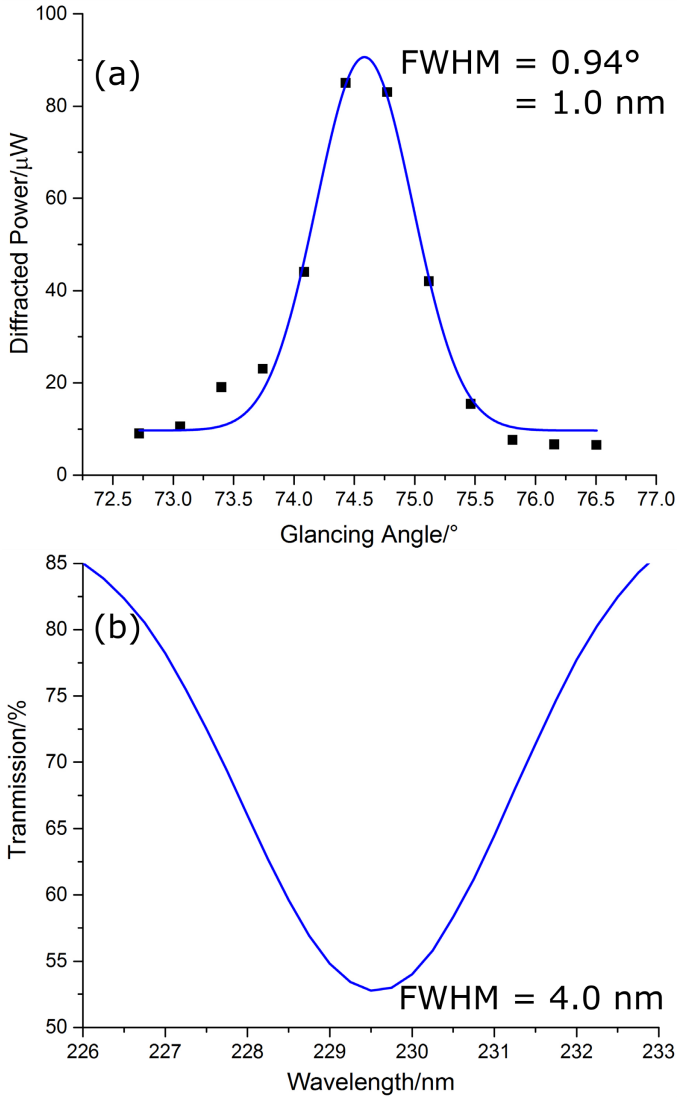

Figure 3.4 – (a) Diffraction power of the 229 nm laser beam diffracted by PC in panel (b) as a function of laser glancing angle within the PC dispersion. Incident beam power is ~150 μW. A Gaussian fit is depicted in blue. (b) PC transmission measured in the absorption spectrometer at a 68° glancing angle measured in air (74° within PC after refraction).

We measured a maximum diffraction efficiency of ~50% at a glancing angle of 74.4° (Figure 3.4a). We measured a bandwidth of ~4.0 nm FWHM for PC transmission at a glancing angle of 68° in our absorption spectrometer (Figure 3.4b), which is ~4 times larger than the calculated bandwidth measured via the laser beam intensity diffraction method (Figure 3.4a).

During the 229 nm laser beam intensity measurements we discovered that extended 229 nm laser beam irradiation causes local PC disorder likely due to photochemical reactions that presumably increase ionic strength. The beam intensity used was too small to give rise to photothermal effects due to local heating.[251,252] These PC photochemical reactions will be negligible during UV Raman imaging due to the weak incident UV power produced by UV Raman photons.

3.3.2 UV Wide-Field Imaging Spectrometer Design

Figure 3.5 shows a schematic of our deep UV wide-field imaging spectrometer. We utilized a custom-built Maksutov-Cassegrain telescope (Questar 3.5" Field Model) optimized for deep UV transmission to collect Raman scattered light from a 2.3 m standoff distance. A 229/244 nm dual notch filter (NF, Semrock NF01-229/244-25) was attached to the exit port of the telescope to reject Rayleigh scattered light. The collected light was collimated by a 2" diameter plano-convex lens (L1).

The PC diffraction angle was set by a computer controlled rotational stage (Zaber X-RSW60A, fine resolution, low speed model) to enable precise, reproducible tuning of the PC angle. Prior to Raman imaging, a 1280x1024 color CMOS camera (CMOS, Thor Labs DCC1645C) with a 35 mm f/2.0 lens (Thor Labs MVL35M23) was used to image the sample using ambient visible light. This image also enabled alignment of the spectrometer with respect to the sample.

The Raman light diffracted by the PC was directed to a 2" diameter planar UV enhanced mirror (M, CVI Laser Optics DUVA-PM-2037-UV) mounted to a rotational (Zaber X-RSW60A) and translational stage (Zaber T-LSM200A, 200 mm travel). Mirror M directed the diffracted

Raman scattered light through the center of lens L2. A 2" plano-convex lens (L2) mounted to a translational stage (Zaber T-LSM050A, 50 mm travel) focused the Raman image onto the CCD.

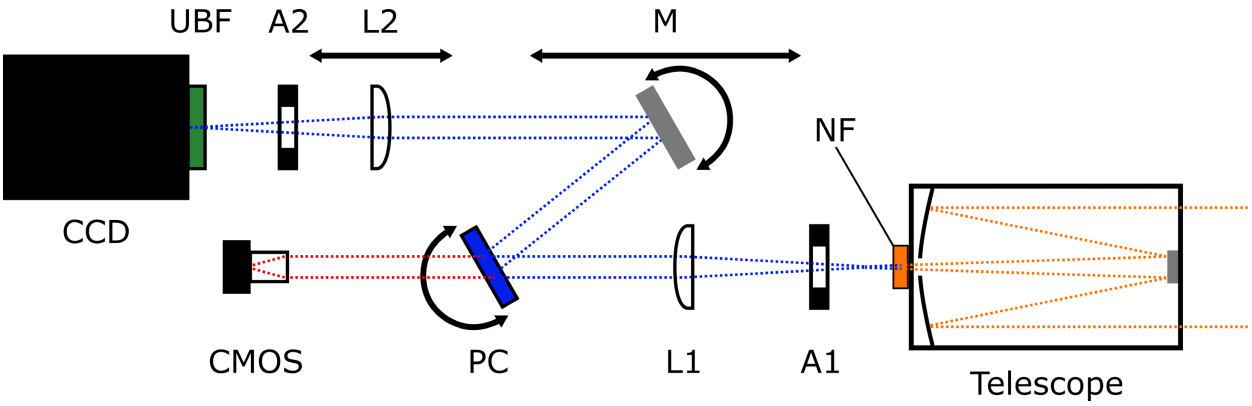

Figure 3.5 – Schematic of the standoff deep UV hyperspectral Raman imaging spectrometer. NF, 229 nm notch filter; A1, aperture; L1, plano-convex collimating lens; PC, UV diffracting photonic crystal mounted on a rotational stage, CMOS, color camera with 35 mm lens; M, planar mirror mounted on a rotational stage connected to a translational stage; L2, plano-convex focusing lens mounted on a translational stage; A2, aperture; UBF, UV bandpass filter; CCD, PIXIS detector. f_{L1} = 205 mm and f_{L2} = 95 mm at 229 nm.

A solar blind UV bandpass filter (UBF, Acton Optics FB240-B-2D) was mounted directly to the face of the CCD detector to reduce interference from ambient light and sample luminescence. The UBF has a peak transmission of 40% at 237 nm, a FWHM of 32 nm, and >2.5 OD from 350 nm – 1100 nm. A thermoelectrically cooled CCD detector (CCD, Princeton Instruments PIXIS 1024 BUV, 1024 x 1024, 13 x 13 μm pixels) was utilized to collect deep UV Raman images. The Raman image S/N was increased by sacrificing image resolution through hardware binning of adjacent CCD pixels into super-pixels prior to image readout. 8 x 8 and 6 x 6 pixel binning was utilized for the 30 sec and 2 min image accumulation times, respectively.

The imaging spectrometer was constructed inside a light-tight optical enclosure utilizing construction rails and black hardboard (Thor Labs). The spectrometer was mounted to a 4 x 2' breadboard (Melles Griot) attached to a wheeled cart (Thor Labs Optics a la Cart).

3.3.3 Raman Wide-Field Imaging

We utilized this deep UV wide-field imaging spectrometer to detect explosive films of AN and PETN. The drop-cast explosive samples (Figure 3.6), and the inkjet printed explosive samples (Figure 3.7 and Figure 3.8), were placed 2.3 m in front of the imaging spectrometer telescope. The samples were centered along the spectrometer's optical axis by using the imaging spectrometer CMOS camera. We then directed the ~1.2 x 1.2 cm expanded 229 nm beam to excite the explosive samples. The telescope collected the Raman scattered light, which was collimated and directed onto the PC. Prior to imaging, the PC was angle tuned to diffract a spectral region centered on the most intense Raman bands of each explosive.

A 16.5° PC rotational angle was utilized to diffract the spectral region centered about the intense AN 1044 cm^{-1} NO_3^- symmetric stretching band (Figure 6b). At this PC angle, the AN film shows a much larger Raman image intensity than does the PETN film (Figure 3.6c and Figure 3.6d) due to the large Raman solid state cross section of the 1044 cm^{-1} AN band, previously measured by Emmons *et al*. to be 3.4 x 10^{-26} cm^2/molc·sr.[27] The PETN film surprisingly shows a weak but significant Raman image intensity despite a lack of a PETN Raman band within the PC band FWHM diffraction spectral region. We expect small intensity contributions from the adjacent 1269 and 1289 cm^{-1} Raman bands because they will be diffracted by the PC diffraction tails (Figure 3.4a). We also expect a small broadening of the PC diffraction bandwidth due to imperfections in the collimation of Raman light within the imaging spectrometer. In addition,

there may also be contributions to the PETN image intensity due to the formation of PETN photoproducts. We recently discovered that PETN photolysis *in the presence of water* will produce NO_3^- which will give rise to PETN image intensity resulting from the NO_3^- symmetric stretching band.[30]

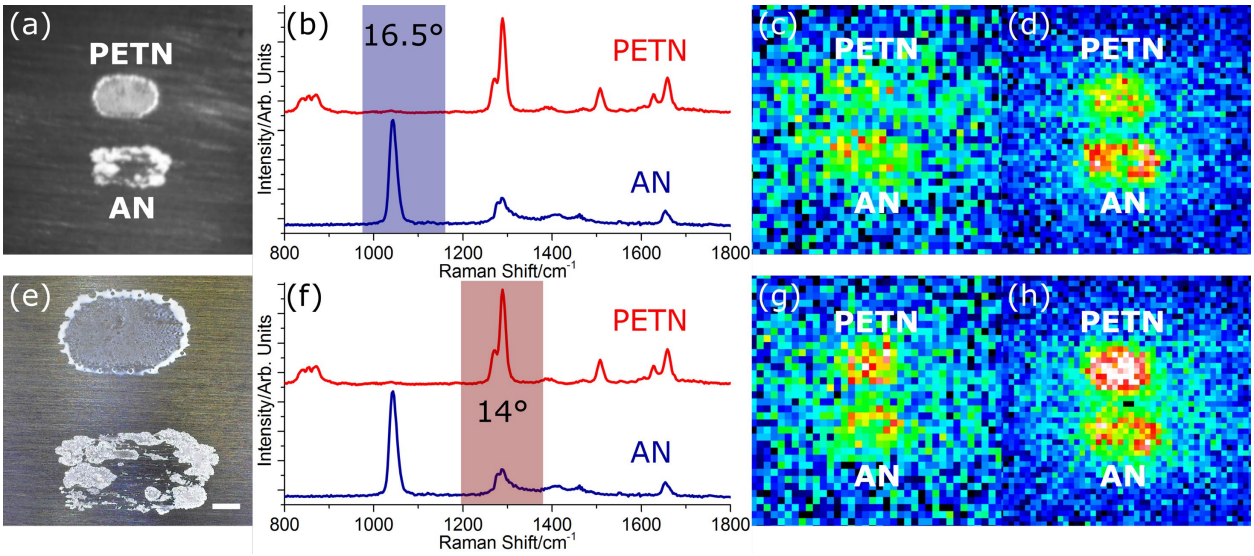

Figure 3.6 – (a) CMOS image of the 120 µg (920 µg/cm^2) PETN (top) and 120 µg (760 µg/cm^2) AN (bottom) drop-cast films on an aluminum plate at a 2.3 m standoff distance. (b) 229 nm Raman spectra of solid PETN (top, red) and solid AN (bottom, blue). A ~1 nm FWHM diffracted spectral bandwidth at a 16.5° PC angle is depicted by the blue shading. (c and d) Raman images of the trace explosive sample shown in (a) at a 16.5° PC angle after 30 sec and 2 min accumulations, respectively. (e) Expanded 30x microscope image of the sample in panel (a) before irradiation. Scale bar represents 1 mm. (f) 229 nm Raman spectra of solid PETN (top) and solid AN (bottom). A ~1 nm FWHM diffracted spectral bandwidth at a 14° PC angle is depicted by the red shading. (g and h) Raman images of the trace explosives shown in (a) at a 14° PC angle after 30 sec and 2 min accumulations, respectively. Both rotational angles of incidence are measured in air. 30 sec and 2 min accumulations utilize 8 x 8 and 6 x 6 pixel binning, respectively.

The image intensity (I_R) of each pure analyte film should scale with the Raman cross sections (σ) of the Raman bands diffracted by the PC and the number of molecules (N) involved in the Raman scattering (Equation 3.5).

Equation 3.5 $$I_R \sim \sigma * N$$

The number of analyte molecules involved in this Raman scattering depends upon the attenuation of the incident beam within the film due to absorption as well as due to elastic light scattering due to refractive index inhomogeneities (Equation 3.6).[253]

Equation 3.6 $$I_R \sim {\sigma * \rho}/{m(\varepsilon + \gamma)}$$

where ρ is the film density, *m* is the analyte molecular weight, ε is the molar absorptivity of the analyte at 229 nm, and γ is the effective attenuation factor due to elastic light scattering.

The image intensity may also depend upon film thickness. In the thick film limit where the beam is completely attenuated as it traverses the film, the number of Raman scattering molecules depends on the penetration depth of the beam through the film. The beam penetration depth is inversely proportional to the molar absorptivity of the sample and to elastic scattering due to refractive index inhomogeneities $(\varepsilon+\gamma)^{-1}$. In the thick film limit, the Raman intensity is independent of film thickness. In contrast, in the thin film limit the exciting beam is not completely attenuated before traversing the entire film thickness. In this case, the Raman image intensity is proportional to film thickness. The AN drop-cast sample is partially in the thin film limit since the exterior of the AN film shows higher Raman image intensity than the thinner center of the film (Figure 3.6d). Crystallite orientation within the films could also affect Raman image intensities. We are presently investigating the influence of film morphology on Raman image intensity.

In contrast, a 14° PC rotational angle was utilized to diffract the Raman spectral region centered about the intense PETN 1289 cm^{-1} NO_2 symmetric stretching band (Figure 3.6f).[229,254,255]

Emmons *et al.* measured an 3.2 x 10^{-26} cm^2/molc·str effective solid state Raman cross section sum for the PETN 1289 cm^{-1} band and the overlapping shoulder at 1269 cm^{-1}.[27] For solid AN, this region contains the NO_3^- anti-symmetric stretching Raman band at ~1288 cm^{-1}.[27,256,257] We estimate a solid state Raman cross section of 1.7 x 10^{-26} cm^2/molc·str for the AN 1288 cm^{-1} anti-symmetric stretching band. Thus, at the 14° PC angle the image intensity of PETN band should exceed that of AN (Figure 3.6g and Figure 3.6h). It should be noted that a different PC with different diffraction angles was utilized for imaging the inkjet printed explosive samples (Figure 3.7 and Figure 3.8).

We also measured deep UV Raman images of 250 μg/cm^2, 100 μg/cm^2, and 10 μg/cm^2 PETN and AN films deposited on smooth aluminum substrates via inkjet printing (Figure 3.7 and Figure 3.8). The sample surfaces illuminated by the 229 nm laser include a lower region covered with an explosive as well as an upper, expectedly bare, aluminum region. High S/N Raman images were collected for all PETN inkjet samples with short accumulation times and low surface coverages (Figure 3.7). PETN is easily detectable at 10 μg/cm^2 due to the uniform surface coverage. The mounds of PETN visible in the CMOS images of the 250 and 100 μg/cm^2 inkjet samples (Figure 3.7a and d) are not visible in the UV Raman images (Figure 3.7b, c, e, and f) because of the presence of optically thick PETN in the regions between the mounds. Since PETN is present between the large, visible mounds, we expect that the uninterrupted optically thick PETN film should produce roughly uniform Raman image intensity.

The similar Raman image intensities observed for all three PETN inkjet samples (Figure 3.7c, f, and i) also indicate that these samples are all optically thick. The observed Raman image intensity will decrease only when the PETN films become sufficiently thin such that the incident 229 nm laser beam is no longer fully attenuated before traversing the entire thickness of the film.

Given the high S/N images collected at a surface coverage of 10 μg/cm^2, we estimate a detection limit of ~1 μg/cm^2 for PETN under these experimental conditions and for films uniformly distributed across the substrate surface.

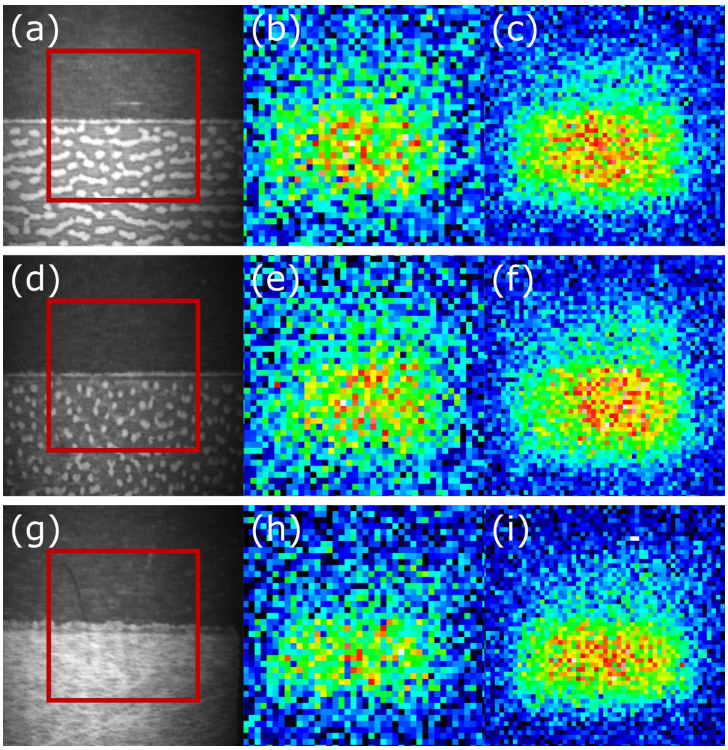

Figure 3.7 – (a, d, and g) CMOS images of 250 μg/cm^2, 100 μg/cm^2, and 10 μg/cm^2 of inkjet printed PETN on smooth aluminum substrates, respectively, at a 2.3 m standoff distance. Red outlines indicate the area illuminated with 229 nm excitation. (b, e, and h) Raman images of the trace explosives shown in panels (a, d, and g) at a 13° PC angle at 30 sec (8 × 8 binning) of accumulation. (c, f, and i) Raman images of the trace explosives shown in panels (a, d, and g), at a PC angle of 13° at 2 min (6 × 6 binning) of accumulation. The PC used here differs from that used in Figure 3.6. At a 13° PC angle, the PC diffracts a Raman spectral region centered at the 1289 cm^{-1} PETN NO_2 symmetric stretch.

AN is also easily detectable in high S/N Raman images for the 250 and 100 μg/cm^2 samples (Figure 3.8). However, for the 10 μg/cm^2 AN sample (Figure 3.8h and i), it becomes challenging

to differentiate the edge between deposited AN and the adjacent aluminum surface. During these measurements we observed that high lab humidity quickly lead to deliquescence (Figure 3.8d and g) of hygroscopic AN samples. We hypothesize that vaporization and re-deposition[258] or efflorescence-like migration[259,260] of AN may decrease the sharpness of the AN film/aluminum interface.

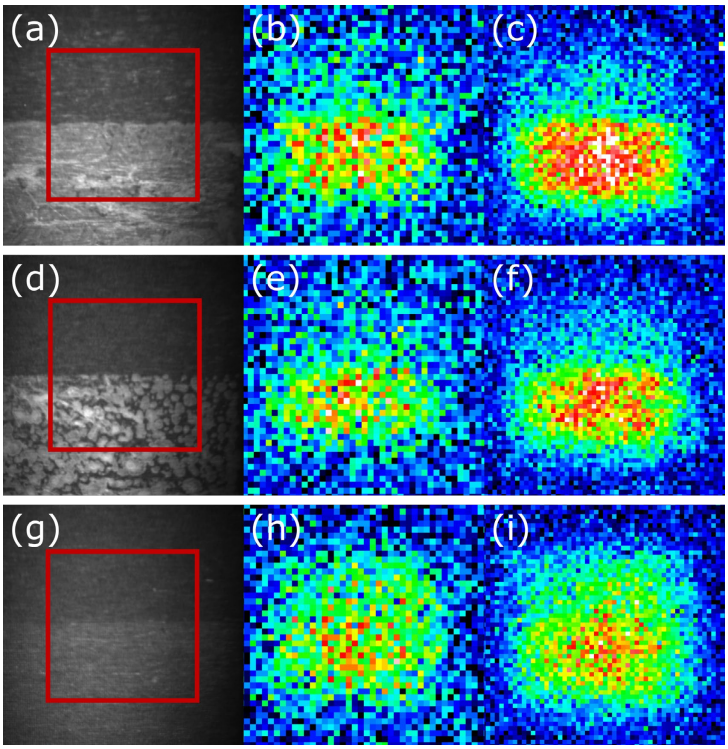

Figure 3.8 – (a, d, and g) CMOS images of 250 µg/cm^2, 100 µg/cm^2, and 10 µg/cm^2 of inkjet printed AN on smooth aluminum substrates, respectively, at a 2.3 m standoff distance. Red outlines indicate the areas illuminated with 229 nm excitation. (b, e, and h) Raman images of the trace explosives shown in panels (a, d, and g), at a 16° PC angle at 30 sec (8 × 8 binning) of accumulation. (c, f, and i) Raman images of the trace explosives shown in panels (a, d, and g), at a 16° PC angle at 2 min (6 × 6 binning) accumulations. At a 16° PC angle, the PC diffracts a Raman spectral region centered at the 1044 cm^{-1} AN NO_3^- symmetric stretch. The diffracting PC used here is identical to that used in Figure 3.7.

In contrast to the PETN inkjet samples, the AN Raman image intensity decreases with decreasing amounts of deposited AN (Figure 3.8c, f, and i). As the amount of deposited AN decreases, the film becomes less homogeneous and optically thin areas become evident in both the microscope and color CMOS images (Figure 3.8d and g), resulting in less Raman image intensity. We also estimate a detection limit of ~1 μg/cm^2 for AN under these experimental conditions and for films uniformly distributed across the substrate surface.

3.4 Conclusion

We demonstrated that our novel deep UV diffracting PCs enable the construction of the first wide-field UV imaging spectrometer for the standoff detection of trace explosives. We utilized our UV Raman wide-field imaging spectrometer to detect and image 10 - 1000 μg/cm^2 PETN and AN films on aluminum substrates at 2.3 m standoff distances with 229 nm excitation. We observed UV Raman images of sample surfaces that depict the deposition morphologies of these explosives and allow them to be chemically differentiated. We estimate a detection limit of ~1 μg/cm^2 for PETN and AN under these experimental conditions for films uniformly distributed across the substrate surface. The ~1 nm PC diffraction bandwidth demonstrated here is still relatively broad. We are presently optimizing our PCs to narrow the bandwidth of the diffracted spectral region in order to increase the spectral resolution of our UV imaging spectrometer. Increasing the PC nanoparticle size monodispersity and charge will improve the ordering of the PC, narrowing the diffracted spectral bandwidths. We are currently working to optimize and miniaturize our UV imaging spectrometer by improving our PC technology and miniaturizing our novel deep UV laser sources.

3.4.1 Acknowledgements

The authors thank the Pitt Chemistry Machine Shop for machining sample substrates and spectrometer adapter pieces as well as the US Army Research Lab for generously donating inkjet printed explosive samples. We acknowledge funding from the Office of Naval Research (ONR) N00014-12-1-0021 and N00014-16-1-2681 grants and the Department of Defense/Technology Commercialization Consortium/Innovation Works (DOD/TCC/IW) grant, DOD award number OEA ST 1429.14.01, Commonwealth of Pennsylvania contract number C000061864.

4.0 Chapter 4: Solid Deep Ultraviolet Diffracting Inverse Opal Photonic Crystals

This chapter was previously published in the journal *ACS Applied Nano Materials* as K. T. Hufziger, A. B. Zrimsek, and S. A. Asher, "Solid Deep Ultraviolet Diffracting Inverse Opal Photonic Crystals". ACS Appl. Nano Mater. 2018. 1(12): 7016-7024, and is reprinted with permission. K.T.H. collected and analyzed the data with the assistance of A.B.Z. This manuscript was prepared by K.T.H. with the assistance of A.B.Z and S.A.A.

4.1 Introduction

The development of spectroscopic techniques utilizing deep ultraviolet (UV) (<300 nm) light is significantly impeded by the scarcity of optics that operate in this spectral region. High performance optics, such as narrow and broadband dielectric mirrors, as well as Rayleigh rejection filters for Raman spectroscopy, are commercially available throughout the near-UV, visible, and near-IR spectral regions. However, the availability of such optics in the deep UV is extremely limited, especially for Rayleigh rejection optical devices at wavelengths of <250 nm. In addition, the performance of deep UV optics is generally challenged by the absorption of many materials in the deep UV.[15]

Limited deep UV optic availability greatly complicates construction of deep UV Raman instruments. The lack of Rayleigh rejection optics impedes development of deep UV Raman spectroscopy by necessitating the use of multiple monochromator stages to remove the intense Rayleigh scattered light. This drastically decreases light throughput and requires long

accumulation times during spectral collection.[21, 196, 247] In addition to the lack of deep UV rejection filters for Raman spectroscopy, the lack of optics that are capable of transmitting or diffracting narrow bandwidth spectral regions in the deep UV, such as liquid crystal tunable filters (LCTFs), acousto-optic tunable filters (AOTFs), and dielectric notch filters, strongly hinders the development of deep UV wide-field imaging spectroscopies that require these devices.[12] These devices are frequently utilized in the visible and near-IR spectral regions to select a narrow bandwidth spectral region to focus onto a detector and form a wide-field image. Unfortunately, to our knowledge these wavelength selection devices have not previously been manufactured in the deep UV spectral region.

Our group recently developed the first deep UV diffracting photonic crystals (PCs) that function as Rayleigh rejection filters for 229 nm excited Raman measurements and as the wavelength selection device in the first 229 nm wide-field Raman imaging spectrometer for standoff trace explosive detection.[15, 261] In our previous work, we synthesized highly charged, monodisperse silica nanoparticles via modified Stöber methods. After removal of electrolytes and other impurities that screen electrostatic interactions, these highly charged nanoparticles self-assemble via electrostatic repulsion to form aqueous non-close-packed face centered cubic (FCC) colloidal crystals that diffract narrow bandwidth spectral regions in the deep UV. Further development of deep UV diffracting PCs would enable their commercialization as Rayleigh rejection optics, optical filters, wide-field imaging optics, and dielectric-style or dichroic-style mirrors that reflect particular wavelengths only at certain angles.

The current challenge for the development of PCs for use in deep UV spectroscopic instrumentation is that the electrostatically stabilized colloidal crystals composed of silica nanoparticles in water are relatively fragile. Aqueous PCs can be transiently disordered by deep

UV laser-induced photochemistry that produces ions that screen interparticle repulsions. In addition, PC ordering can be disrupted by mechanical vibrations, temperature variations, and solvent evaporation.

Several strategies can be employed to improve PC stability and shelf life. For example, PC durability can be improved by polymerizing a matrix around the FCC nanoparticle array, embedding the nanoparticles in a polymer film that resists disorder.[61, 236, 262] Utilizing this approach to fabricate deep UV diffracting PCs is challenging since the nanoparticles and polymer matrix must be transparent in the deep UV.[263] Nanoparticles can also be self-assembled into 2D or 3D close-packed structures by using various evaporative techniques, producing solventless PCs on solid substrates.[62-64, 115, 264]

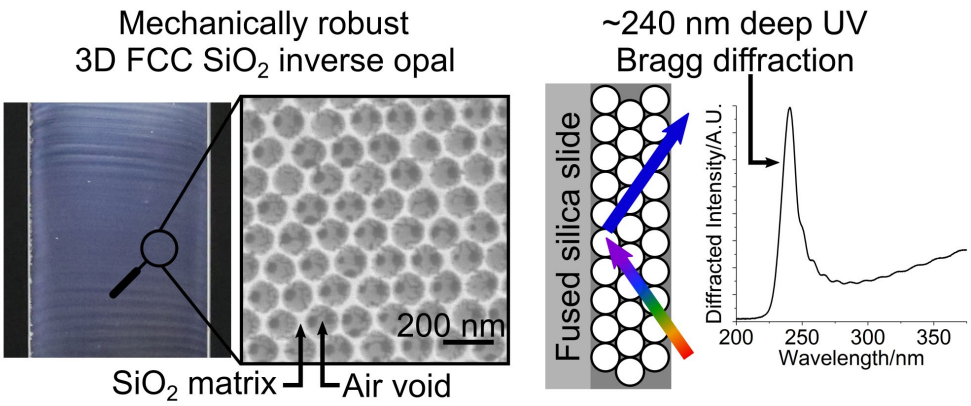

Figure 4.1 – Photograph, micrograph, and diffraction results obtained from a deep UV diffracting inverse opal photonic crystal.

Here, we explore the fabrication of inverse opals (IOs) that form solventless, indefinitely shelf stable deep UV diffracting PCs (Figure 4.1). IO PCs are typically fabricated by filling the interstices of a 3D nanoparticle PC with a liquid monomer, sol-gel precursor, or mineral precursor solution, which is then polymerized or crystallized, embedding the nanoparticles in a solid

matrix.[47, 53, 265-268] Removal of the nanoparticles by either dissolution or calcination while preserving the interstitial matrix yields the final IO PC. This IO PC structure consists of an ordered array of voids left after nanoparticle removal.

Recently, Hatton *et al*. developed a coassembly vertical deposition method wherein self-assembly of a 3D close-packed FCC array of polymer nanoparticles occurs on a vertical substrate in the presence of tetraethyl orthosilicate (TEOS), a sol-gel precursor that condenses during self-assembly to form an SiO_2 matrix within the nanoparticle interstices.[53] Calcination of the PCs in an oven at 500 °C removed the polymer nanoparticles while leaving the SiO_2 matrix mostly intact, yielding an IO PC structure.

In this work, we utilized the deep UV transparency and mechanical strength of SiO_2 to fabricate the first mechanically robust, solventless deep UV diffracting IO PCs by using a modified coassembly vertical deposition method. To create these IO PCs, we first vertically deposit 138.3 ± 3.1 nm diameter polystyrene nanoparticles (PSNPs) into a 3D close-packed FCC structure on a fused silica microscope slide in the presence of TEOS. This results in a PSNP FCC structure embedded in an SiO_2 matrix. We then react these PSNP/SiO_2 PCs with piranha solution to dissolve the PSNPs, forming IO PCs that Bragg diffract light in the deep UV. Importantly, these IO PCs are stable and show no diffraction degradation during handling or UV laser irradiation. We investigate the diffraction and morphology of these PCs to determine their ordering and utility as deep UV PC diffraction devices.

4.2 Experimental

4.2.1 3D Close-Packed PSNP/SiO_2 PC Self-Assembly and IO PC Formation

For terminology, "PSNP/SiO_2 PCs" shall be used when referring specifically to solid 3D close-packed FCC PCs containing PSNPs surrounded by an SiO_2 matrix formed by vertical deposition. "IO PCs" shall be used when referring specifically to PSNP/SiO_2 PCs after treatment with piranha to remove the PSNPs, yielding an FCC array of voids surrounded by an SiO_2 matrix.

We synthesized 138.3 ± 3.1 nm diameter monodisperse, highly charged PSNPs (Figure 4.8) via a modified[170] emulsion polymerization procedure[59] (see Supporting Information for synthesis details). We measured a ζ-potential of -49.5 mV at pH 5.0. These nanoparticles were self-assembled to form 3D close-packed PCs on fused silica substrates utilizing a modified vertical deposition procedure based on the method of Hatton *et al*.[53]

3 x 1" fused silica microscope slides (Technical Glass Products 80/50 scratch dig, 1 mm thick) were cut into ~50 x 12 mm pieces using a glass saw. Directly before use the 50 x 12 mm substrate was immersed in freshly prepared 3:1 v/v H_2SO_4/H_2O_2 (Fisher Scientific A300 96% w/w and Fisher Scientific H323 30%) piranha solution to remove surface contaminants and increase substrate hydrophilicity. *Safety warning: Piranha solution becomes extremely hot upon mixing, is a powerful oxidizer, reacts rapidly with organics, and produces gases. Make only in small quantities as needed and use appropriate protective equipment.* After several hours of soaking, the substrate was removed from piranha, immediately rinsed with nanopure H_2O (Thermo Scientific Barnstead), and stored in nanopure H_2O until use.

A dilute PSNP solution was prepared by first centrifuging an aliquot of stock colloid solution at 1000 relative centrifugal force (RCF) for 1 min to spin-down ion-exchange resin beads.

Following centrifugation, an aliquot of stock colloid solution was diluted with nanopure H_2O to produce a 21.00 mL solution, typically containing 0.18% v/v PSNPs, in a 20 mL (nominal volume) scintillation vial (Fisher Scientific 03-337-14 borosilicate, 61 × 28 mm height × outer diameter). Fresh 0.1 M HCl (Fisher Scientific A144S, 37% w/w) was prepared in nanopure H_2O. A *TEOS solution* was freshly prepared by mixing 800 µL of 0.1 M HCl solution, 1520 µL of ethanol (Decon Labs 200 proof), and 812 µL of tetraethyl orthosilicate (TEOS, Sigma Aldrich 86578, >99%). The *TEOS solution* was sealed and mixed for ~1 h until use to allow time for HCl catalyzed hydrolysis of TEOS.[269]

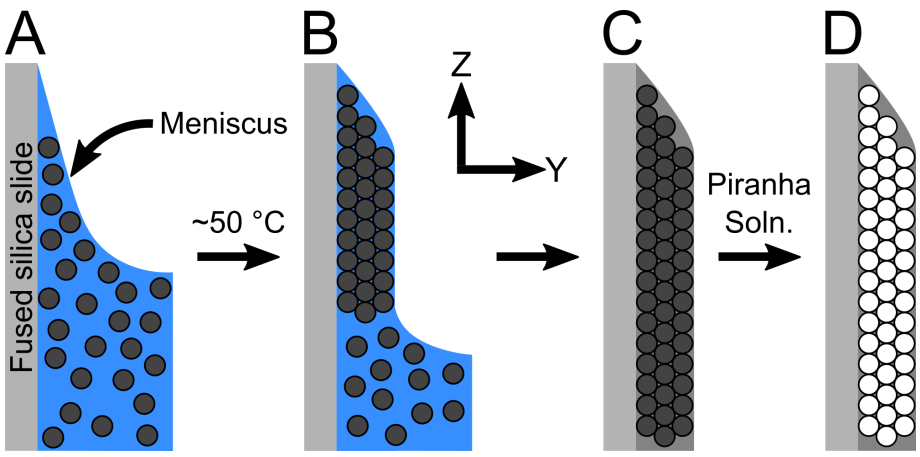

Figure 4.2 – Schematic of the deep UV diffracting IO PC fabrication method. (A) A clean, hydrophilic fused silica substrate is dipped into a solution, depicted in blue, containing PSNPs, TEOS, ethanol, HCl, and water in a 20 mL vial. The vial is then placed in a hot oven. (B) Self-assembly of the 3D close-packed FCC PSNP structure onto the fused silica substrate proceeds via evaporation driven vertical deposition over several days while TEOS condenses in the PSNP interstices to form an SiO_2 matrix. (C) After drying, the PSNPs are embedded in an SiO_2 matrix that is attached to the fused silica substrate. (D) Piranha solution is used to remove the PSNPs while leaving the SiO_2 intact, yielding an FCC array of voids in the SiO_2 matrix.

The vertical deposition setup was prepared as follows. An oven (Thermo Scientific Heratherm IMH-60) situated on a floated optical table (Kinetic Systems Vibraplane) was heated to ~48.3 °C. The temperature and humidity in the oven were recorded by using a hygrometer probe (Traceable Hygrometer 11-661-7B) situated next to the deposition vials on the top shelf of the oven. The oven fan was set at the lowest speed (20% setting) to gently circulate oven air. Oven air was slowly and continually refreshed during the experiment by purging the oven with 2.6 standard liters per minute (SLPM) dry N_2 gas. The N_2 line was run through the open oven accessory port on the top/back of the oven, with the line outlet situated on the bottom shelf of the oven.

A 225 μL aliquot of *TEOS solution* was added to the 21.00 mL of dilute PSNP solution and mixed. A piranha cleaned fused silica substrate stored in nanopure H_2O was rinsed with fresh nanopure H_2O and placed in the scintillation vial containing the PSNP solution and *TEOS solution*. The vial containing the fused silica substrate was then placed into the preheated oven. The oven was then closed, and self-assembly of the 3D close-packed FCC array was allowed to proceed undisturbed for 4 days. Typical oven humidity values ranged from ~11% relative humidity at the beginning of self-assembly to ~2% when the solution was nearly evaporated. The oven temperature was maintained within ±0.2 °C of its median value during self-assembly. After evaporation of most of the PSNP/TEOS solution, the fused silica substrates with attached close-packed PSNP/SiO_2 PCs were removed from the oven and placed into clean vials for storage.

To remove the PSNPs from the PSNP/SiO_2 PCs while leaving the surrounding SiO_2 matrix intact, we completely immersed the PSNP/SiO_2 PCs in freshly prepared 3:1 v/v piranha solution overnight. After soaking, the PCs were removed from piranha and immersed in a vial of nanopure H_2O. The H_2O was changed once to wash away remaining acid, and the PCs were then allowed

to air-dry before use, yielding the final IO PCs. A schematic of the fabrication method is depicted in Figure 4.2.

4.2.2 Nanoparticle and PC Characterization

PSNP diameters (Figure 4.8) were measured by evaporating a small aliquot of dilute colloidal dispersion onto a Formvar coated Cu grid (Ted Pella 01814-F) before imaging with a transmission electron microscope (FEI Morgagni 268). >100 nanoparticle diameters were measured via ImageJ (NIH) software to determine the size distribution of the particles. The ζ-potential of the PSNPs was measuring using a Malvern ZS-90 Zetasizer (Smoluchowski approximation).

IO PC ordering (Figure 4.3) was monitored using a scanning electron microscope (SEM) (Ziess Sigma 500 VP FE-SEM) in SEI mode at 3 kV accelerating voltage after sputter coating the PCs with Au (Pelco SC-7). The average IO PC void diameter was determined by measuring the distance between the centers of neighboring SiO_2 void walls in scanning electron micrographs (>100 voids measured).

Optical transmission in the near and deep UV (Figure 4.4) was measured using a Varian Cary 5000 UV-vis-NIR absorption spectrometer. The PCs were mounted on a rotational stage (Newport 481-A) placed within the spectrometer. The rotational stage was utilized to vary the incident angle of light on the PCs to monitor the Bragg diffraction wavelength as a function of angle. All spectra were baseline corrected where the blank was a clean fused silica microscope slide at normal incidence.

To measure Fabry-Perot interference fringes and determine IO PC thickness (Figure 4.5), 170 – 2100 nm white light from a laser driven light source (LDLS, Energetiq EQ-99X) was

collimated by an off-axis parabolic mirror (Thor Labs MPD249-F01) and directed through an aperture that reduced the beam diameter to 6 mm before illuminating the IO PC. The IO PC was mounted to a microscope slide holder attached to a rotational stage (Newport 481-A) to control the beam incident angle onto the IO PC. Light diffracted by the IO PC was collected by a reflective collimator (Thor Labs RC12SMA-F01), which is a 90° off-axis parabolic mirror. The reflective collimator was utilized to collect and focus the diffracted light into an optical fiber (Thor Labs M22L02). The optical fiber then directed the diffracted light into the slit of a deep UV optimized Ocean Optics QE Pro spectrometer. The IO PC diffraction spectrum shown in Figure 4.5 was produced by dividing the raw diffraction spectrum by the spectrum of the LDLS lamp light reflected from a clean fused silica slide to correct for the instrument throughput and the source spectral shape.

To directly measure the Bragg diffraction bandwidth of the IO PCs, we measured the angular dependence of 229 nm light diffraction (Figure 4.6). Collimated 229 nm light was generated by a continuous wave frequency doubled Ar ion laser (Coherent Innova 300c FreD). A fused silica slide was placed in the incident beam path at an oblique angle to pick off a small portion of the beam, which was measured by a photodiode power sensor (Thor Labs S120VC head attached to a PM200 meter) that continuously monitored the incident power. The beam was then directed through an aperture to produce a 3 mm diameter circular beam at the IO PC. The IO PC was mounted to a motorized rotational stage (Zaber X-RSW60A) to allow precise, reproducible rotation about the z-axis (Figure 4.3A) of the IO PC. The IO PC was rotated in 0.50° increments, and light diffracted at each incident angle was measured by a second photodiode power sensor (Thor Labs S120VC), positioned at each measurement angle to center the diffracted beam on the sensor head. At each IO PC angle the diffracted power and pick-off power were measured

simultaneously for several seconds (~50 data points per meter per angle, Thor Labs Multi Power Meter Utility) to average out any laser power variations. The measured pick-off power was utilized to calculate the incident power on the sample. The diffracted power was divided by the calculated incident power to determine the fraction of power diffracted by the IO PC at each incident angle.

IO PC surface roughness (Figure 4.7B) was quantified using an optical profilometer (Bruker Contour GT-I). Height maps collected using the profilometer were tilt corrected using the instrument software (Bruker Vision64).

4.3 Results and Fabrication

4.3.1 Fabrication Parameters and SEM Analysis

We fabricated the first solid deep UV diffracting IO PCs. To accomplish this, we modified previous vertical deposition methods to optimize the self-assembly of small diameter 138.3 ± 3.1 nm diameter PSNPs (Figure 4.8) into close-packed FCC PCs.[53] To improve the self-assembly of these close-packed PSNP/SiO_2 PCs and to improve the deep UV diffraction, we optimized the oven humidity and temperature, PSNP concentration, volume of *TEOS solution*, and vial/substrate size used during the vertical deposition. We found that the vial size is crucially important to produce IO PCs that efficiently diffract in the deep UV. We could reproducibly and easily fabricate IO PCs with strong deep UV diffraction by using 20 mL scintillation vials or smaller, 3-dram vials (using smaller substrates) under similar solution and oven conditions. However, it was difficult to obtain good deep UV diffraction for PCs fabricated using 3 x 1" fused silica substrates placed in larger 50 mL vials. A deep UV diffracting IO PC was fabricated on a 3 x 1" substrate at

a lower ~31 °C oven temperature; however the IO PC visually appeared very heterogeneous and showed broad diffraction peaks when measured using the absorption spectrometer, indicating that the nanoparticle ordering was generally poor.

The self-assembly mechanism of 3D close-packed structures on solid substrates via vertical deposition is still somewhat poorly understood.[101, 108, 114, 270] It is hypothesized that vertical deposition of 3D arrays occurs because the relative evaporation rate from the thin, top part of the solution meniscus near the substrate-air-solution contact line is faster than from the bulk solution (Figure 4.2).[114] Relatively rapid evaporation from the solution meniscus results in a convective solvent flow that continuously draws nanoparticles into the meniscus toward the contact line. It is hypothesized that interparticle capillary forces or convective steering due to solvent flow through nanoparticle interstices draws particles together into a close-packed array that grows as the contact line moves along the substrate z-axis due to continuous solvent evaporation.[108, 110, 111]

The rate of evaporation of the solution relative to the rate of particle influx into the meniscus must be carefully balanced to produce highly ordered 3D close-packed structures. For example, Kaplan *et al*. previously found that continuous, well-ordered vertically deposited arrays only formed when above a certain critical nanoparticle concentration.[114] We hypothesize that the relatively rapid solution evaporation caused by the wide aperture of the 50 mL vial confounds selection of appropriate deposition conditions to produce highly ordered IO PCs.

We utilized piranha solution to remove the PSNPs instead of tetrahydrofuran (THF) or toluene, which is generally used to dissolve PSNPs, because we found that the piranha solution more efficiently removes PSNPs from the SiO_2 matrix. Figure 4.10 depicts the absorbance spectra and photographs of a PSNP/SiO_2 PC sample before and after immersion for 2 days in THF. After THF treatment, the sample opacity visually increases and the FCC diffraction blueshifts slightly

while decreasing in intensity. These results indicate that THF partially and heterogeneously dissolves some of the PSNPs but does not completely remove PS from the SiO_2 matrix. We hypothesize that THF is inefficient at removing PS due to the small interpore "window" size that limits solvent and polymer diffusion into and out of the SiO_2 matrix, respectively. Piranha solution is an extremely strong oxidizer that efficiently destroys organics, such as PSNPs, while leaving the SiO_2 matrix intact. We chose to utilize piranha solution to remove the PSNPs rather than calcination in a 500 °C oven to avoid the partial collapse of the SiO_2 matrix, as previously observed by Phillips *et al.*[266]

Figure 4.3A shows a photograph of a representative deep UV diffracting IO PC after piranha treatment. This IO PC contains a visually homogeneous region indicated by an arrow that diffracts strongly in the deep UV. Parts B–E of Figure 4.3 show SEM micrographs of the visually homogeneous region of the IO PC indicated in Figure 4.3A. The surface of the strongly diffracting region of this IO PC shows a close-packed FCC (111) plane of voids surrounded by the SiO_2 matrix remaining after removal of the PSNPs via piranha treatment. At high magnification, up to three subvoid features are visible (Figure 4.3C) through windows formed in the SiO_2 matrix between the top two FCC planes. These windows are formed during self-assembly where direct sphere-to-sphere contact between two FCC planes excludes TEOS and prevents SiO_2 condensation. These subvoids indicate that either FCC or hexagonal close packing continues for at least one additional layer for this IO PC.

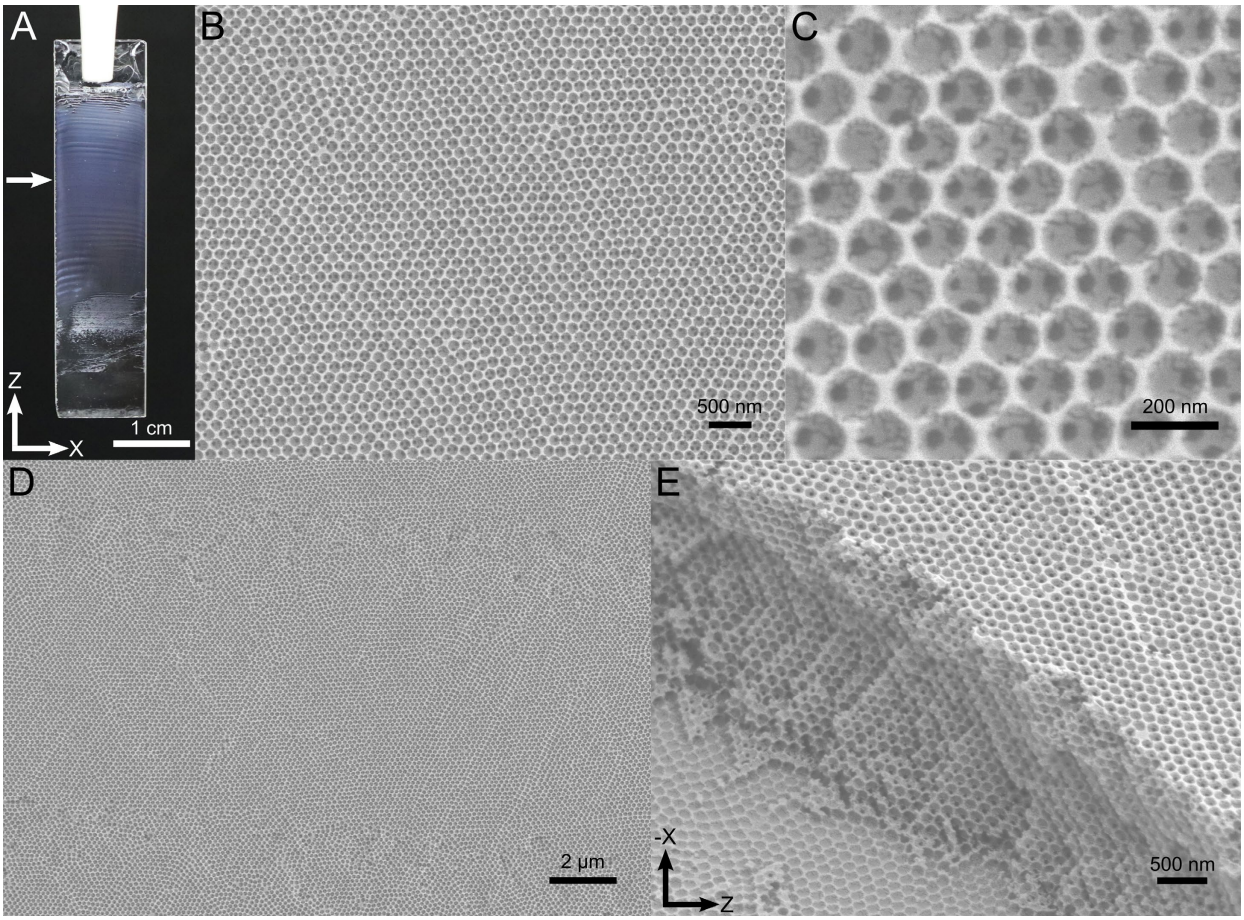

Figure 4.3 – Photograph and SEM micrographs all originating from the same IO PC. (A) Photograph of an IO PC after piranha solution treatment to remove PSNPs. Arrow indicates strongly diffracting region. (B–D) SEM micrographs of the strongly diffracting region of the IO PC shown in panel A. Each micrograph axis orientation is the same as shown in panel A. (E) SEM micrograph of the same IO PC sample tilted 45°, showing the inner structure of a delaminated region at the edge of the fused silica substrate. SEM micrographs of a similar PSNP/SiO_2 PC sample prior to sphere removal are shown in Figure 4.9.

As shown in Figure 4.3D at a lower magnification, the top layer of the visually homogeneous region of this IO PC comprises many well-ordered areas several μm^2 in area that are separated by grain boundaries and smaller, disordered regions. We observed negligible cracking throughout the visually homogeneous region of this sample. To study subsurface structure and relative ordering of the edges of subsurface layers of the IO PC, we imaged any

visible cracks and delaminated areas near the edge of the IO PC substrate (Figure 4.3E) after mounting the IO PC on a 45° tilt sample mount. The subsurface stacking of the FCC (111) layers parallel to the substrate surface appears excellent, with no evident transitions to body centered cubic (BCC) or hexagonally close packed (HCP) structures within this IO PC.

4.3.2 PC Diffraction via UV-Visible Spectroscopy

After self-assembly, the 3D close-packed PSNP/SiO_2 PCs diffract in the near UV according to Bragg's law (Equation 4.1),[170, 226]

$$\textbf{Equation 4.1} \quad m\lambda = 2n_{avg}d \times sin(\theta)$$

where m is the diffraction order, λ is the wavelength of light in vacuum, n_{avg} is the average refractive index of the PC, *d* is the FCC (hkl) spacing, and θ is the glancing angle within the PC.[126]

Before PSNP removal, the PSNP/SiO_2 PCs show an FCC (111) diffraction peak at ~336 nm at normal incidence that is accompanied by strong absorption below 275 nm due electronic transitions of the PSNPs (Figure 4.4A). After Piranha treatment to remove the PSNPs, IO PCs visually become almost transparent to visible light and the FCC (111) diffraction blue-shifts ~94 nm into the deep UV to ~242 nm at normal incidence (Figure 4.4B). The FCC Bragg diffraction wavelength can be precisely controlled by tuning the glancing angle of incident light. Entirely different spectral regions can also be selected for diffraction by utilizing different diameter PSNPs during vertical deposition. For example, we utilized smaller diameter PSNPs under identical vertical deposition conditions to produce IO PCs that diffract at 211 nm at normal incidence (Figure 4.11).

The blue-shifted diffraction upon PSNP removal is expected from Bragg's law due to the decrease in n_{avg} upon removal of the high refractive index PSNPs and their replacement with air.

We utilized the method described by Waterhouse *et al.* to calculate the d_{111} plane spacing and n_{avg} for the PSNP/SiO_2 PCs and IO PCs (Figure 4.4 insets; see Supporting Information for additional details).[115] The FCC d_{111} plane spacing and n_{avg} for six individual PSNP/SiO_2 PCs were calculated to be 101.8 ± 2.2 nm and 1.65 ± 0.04 at ~336 nm, respectively. Three of the six PSNP/SiO_2 PCs were then treated with Piranha to remove the PSNPs, and the measurements were repeated, yielding a calculated FCC d_{111} plane spacing and n_{avg} for the IO PCs of 107.5 ± 2.2 nm and 1.13 ± 0.02 at ~242 nm, respectively.

The ~105 nm d_{111} spacing experimentally determined from Figure 4.4 is slightly shorter than expected from theory. Assuming a totally close packed structure, a 138 nm particle diameter yields an expected d_{111} of ~113 nm.[126] This smaller than expected d_{111} spacing is likely due to slight shrinkage of the SiO_2 matrix along the substrate normal (y axis) due to silanol condensation during the PSNP/SiO_2 PC self-assembly, which was previously observed for a similar system by Phillips *et al*.[266] Using the micrograph shown in Figure 4.3C, we measure an average void diameter of 137.1 ± 7.2 nm in the zx plane, which is similar to the original PSNP diameter. This result indicates that the IO PC voids likely shrink heterogeneously and only along the substrate normal, in agreement with previously observed behavior.

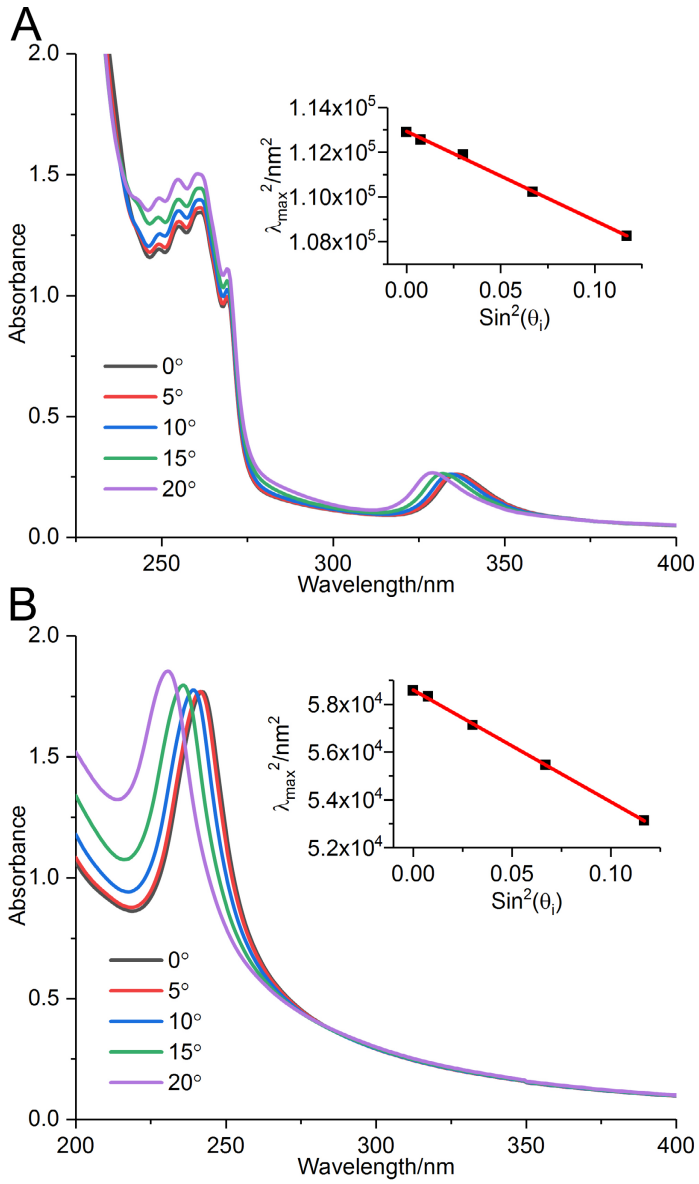

Figure 4.4 – Absorbance spectra measured using the absorption spectrometer of the PC shown in Figure 4.3. (A) PSNP/SiO_2 PC absorbance spectra measured at five incident angles, showing FCC (111) diffraction at ~336 nm and strong PSNP absorption below 275 nm. (B) Absorbance spectra of the same PC at the same incident angles after piranha treatment, yielding an IO PC. The linear fit of λ_{max}^2 versus $\sin^2(\theta_i)$ (inset plots) enables experimental determination of d_{111} and n_{avg}. Listed angles are the incident light angles in air measured from the PC surface normal (θ_i).

Although the calculated d_{111} FCC spacing remains approximately constant after piranha solution treatment, there is a sharp reduction in the measured average refractive index of the PC upon PSNP removal. The theoretical PC n_{avg} can be readily calculated by using a weighted average of the refractive indices of each PC material.[227, 261] Assuming a close-packed PSNP/SiO_2 FCC PC structure, 74% of the volume contains PSNPs, with a refractive index of 1.62 at 437 nm, the shortest wavelength refractive index we found tabulated for PS.[271] The remaining 26% volume contains an SiO_2 matrix with a refractive index of 1.47 at 437 nm and 1.51 at 240 nm,[248] yielding a theoretical n_{avg} for the PSNP/SiO_2 PC of 1.58 at 437 nm. Assuming complete removal of the PSNPs and replacement with air, with a refractive index of 1.00 at 240 nm, results in a calculated n_{avg} for the IO PC of 1.13 at 240 nm, a ~30% reduction upon PSNP removal. This calculated n_{avg} is in excellent agreement with the measured n_{avg} of 1.13 at ~240 nm. This reduction in the PC n_{avg} upon sphere removal results in a blue-shift of the diffraction wavelength according to Bragg's law.

In addition to the blue-shifted diffraction, the overall attenuation of the incident beam, as measured by the absorption spectrometer, also increases upon PSNP removal due to the increased refractive index contrast between the SiO_2 matrix and air, as expected. Scattering strength, and therefore the efficiency of PC diffraction, is related to the refractive index difference between the surrounding SiO_2 matrix and the PSNPs or air-voids.[272] Removal of the PSNPs and replacement with air increases the refractive index contrast within the PC, yielding much stronger diffraction from the IO PCs compared to the PSNP/SiO_2 PCs. This results in stronger attenuation of incident light at the Bragg condition (Figure 4.4B).

4.3.3 IO PC LDLS Diffraction

We utilized a LDLS and a deep UV spectrometer to measure the spectrum of Bragg diffracted light from our IO PCs (Figure 4.5). The LDLS utilizes a tightly focused laser to produce a Xe plasma that emits spectrally broad, bright white light from the far-UV through the near-IR spectral regions. Since plasma formation occurs in a spatially small, point-like area, the Xe plasma emission is easily collimated by using an off-axis parabolic mirror. The resulting output beam is spectrally broad but highly collimated, enabling IO PC diffraction measurements without degradation due to source beam divergence.

A diffraction spectrum of the above IO PC illuminated by the collimated LDLS light is depicted in Figure 4.5. The most intense peak at ~241 nm is due to FCC (111) diffraction. At longer wavelengths from the FCC (111) diffraction peak, several additional, regularly spaced peaks are visible due to Fabry-Perot interference. Fabry-Perot fringing (etaloning) arises from multiple beam interference by light reflected by the top and bottom faces of the IO PC film and is often visible in IO PC LDLS diffraction spectra.[39] Fabry-Perot fringes have been previously observed for 3D close-packed PCs of visibly diffracting silica nanospheres.[64] The λ_{max} of each Fabry-Perot fringe can be easily utilized to calculate the thickness of the self-assembled IO PC film (Figure 4.5 inset). We calculate a thickness of 3558 ± 13 nm, equal to the slope linear fit of the fitted fringe data, for the above IO PC, using the relationships described by Jiang *et al*.[64] Given a measured d_{111} spacing of 107.5 nm (Figure 4.4), we calculate that our inverse opal is ~33 layers thick in the center of the strongly diffracting region indicated by the arrow in Figure 4.3A.

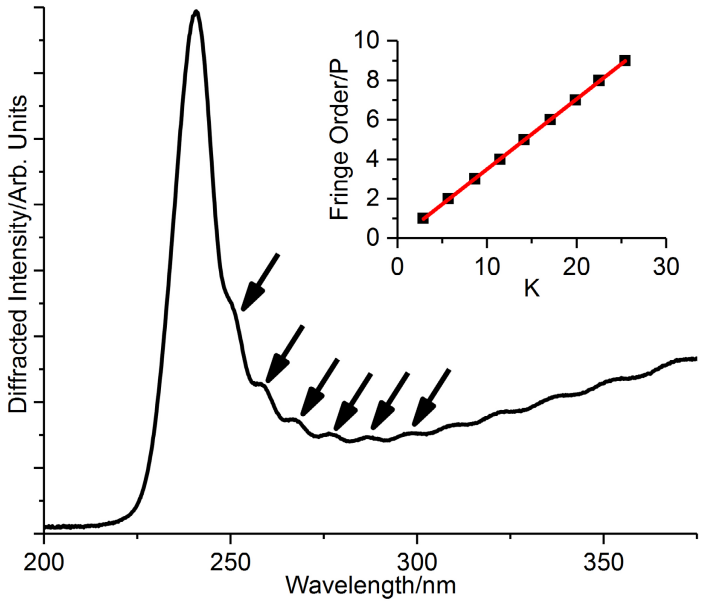

Figure 4.5 – LDLS diffraction spectrum of the IO PC shown in Figure 4.3 at a 15° incidence angle in air. The primary FCC (111) diffraction peak occurs at ~241 nm. Also evident are a number of Fabry-Perot interference fringes, labeled by arrows. Inset: Fabry-Perot fringe plot. $K = (2n_{avg}\cos(\theta_i)(\lambda_1-\lambda_P)/(\lambda_1\lambda_P))\times10^4$ where $n_{avg} = 1.13$, $\theta_i = 15°$, λ_1 is the wavelength of the longest wavelength interference fringe detectable, in this case at 370 nm, and λ_P is the wavelength of subsequent fringes at shorter wavelengths.

Although we rigorously controlled the light incident angle in both absorbance (Figure 4.4) and LDLS diffraction experiments (Figure 4.5), we observe a small ~5 nm difference in the Bragg peak wavelength between these two spectra at the same IO PC rotational angle. We hypothesize that this small difference in Bragg peak wavelength between these two experimental approaches is due to increasing baselines in these spectra that slightly shift the apparent Bragg peak positions. In the collected absorbance spectra, (Figure 4.4) diffuse scattering and slowly increasing absorption by the IO PC SiO_2 matrix cause the transmission to decrease at shorter wavelengths. In the LDLS diffraction spectrum (Figure 4.5), the baseline increases at longer wavelengths likely due to incomplete deconvolution of the lamp spectrum during spectral processing. We expect that the rising baselines in the absorbance spectra and the LDLS diffraction spectrum slightly blue-

shift and red-shift, respectively, the apparent Bragg peak positions. The small shift in the Bragg peak positions between these two techniques negligibly impacts PC parameters calculated using these spectra. For example, the IO PC d_{111} spacing calculated via the absorbance data (107.5 nm, Figure 4.4B) is in excellent agreement with the d_{111} spacing measured using 229 nm laser diffraction (109 nm, Figure 4.6); *vide infra*.

4.3.4 IO PC 229 nm Diffraction

The IO PC diffraction results collected via LDLS illumination provides a convenient way to quantitate the IO PC thickness and to qualitatively assess the FCC Bragg diffraction intensity and bandwidth. To quantitatively determine the IO PC diffraction bandwidth, we measured the intensity of 229 nm laser light diffracted by the IO PC as a function of incident angle, using a more accurate approach based on our previously reported method (Figure 4.6).[261]

To calculate the diffraction bandwidth, we illuminated an IO PC with collimated 229 nm light while tuning the IO PC rotational angle in 0.50° increments and measuring the power of the diffracted light at each angle with a power meter. After accounting for refraction by the IO PC, we calculate a glancing angle of maximum diffracted power of 67.8° and a Bragg diffraction full width at half max (FWHM) of 10.3° from the Gaussian fit of the 229 nm diffraction curve. Using our previously described method, we utilized Bragg's law to calculate the d_{111} plane spacing and the FWHM of the diffracted peak in units of wavelength to be 109 nm and 16.8 nm, respectively. Our 109 nm d_{111} spacing calculated from these 229 nm diffraction data is in excellent agreement with the value calculated for the IO PCs using our absorbance data (Figure 4.4B).

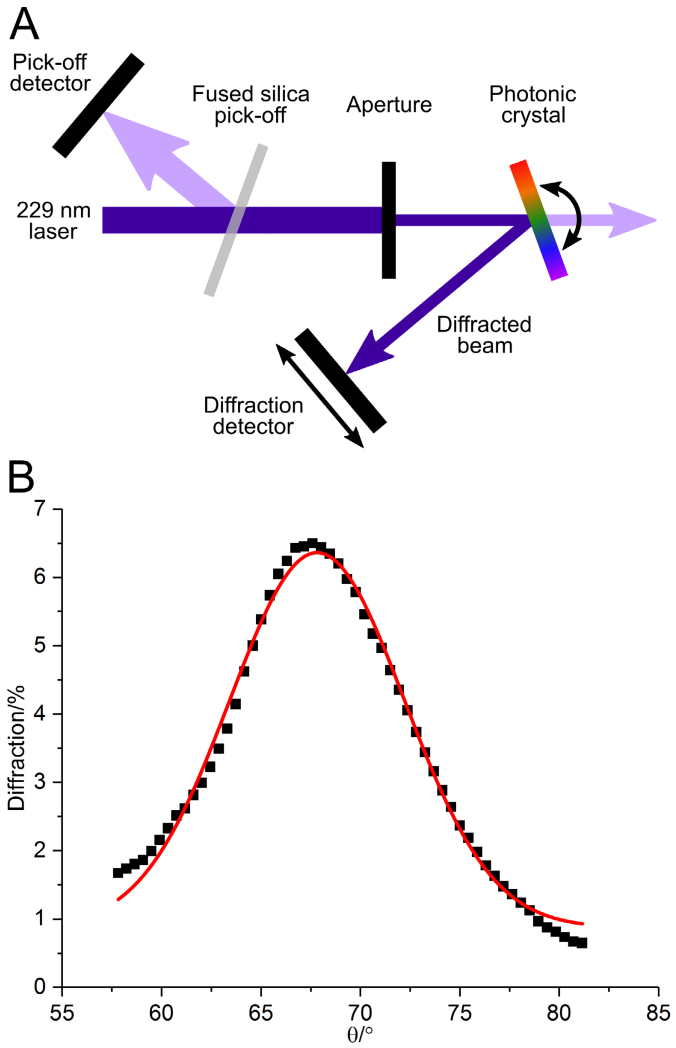

Figure 4.6 – (A) Schematic of the 229 nm diffraction experiment layout. (B) Intensity of 229 nm diffraction by the IO PC shown in Figure 4.3 as a function of Bragg glancing angle, θ, within the IO PC. A Gaussian fit is shown in red.

During these experiments, we observed the transmission and diffraction intensity of the 229 nm beam using fluorescent paper at angles near and far from the Bragg condition. At the Bragg condition, we observe near complete attenuation of the transmitted 229 nm light, indicating strong diffraction. However, we calculate a relatively low maximum diffraction efficiency based on the measured power of the diffracted beam. For the IO PC used to collect the data shown in

Figure 4.6, the diffracted beam appears as an extended line shape (Figure 4.7A). Much of the line shaped diffracted light missed the power meter head, resulting in a lowered calculated diffraction efficiency.

Rotating the IO PC about the laser beam incident axis (y-axis) rotates the line shaped diffracted beam. The sample orientation dependence of the diffraction likely results from the sample morphology. We studied the morphology of the IO PC shown in Figure 4.3A in greater detail using an optical profilometer. Optical profilometers measure surface topology via interferometry, producing images depicting the sample surface roughness a function of position. The strongly diffracting area of the sample (Figure 4.3A, region indicated by arrow) appears homogeneous when observed by eye and via normal incidence SEM. However, when examining the surface topology via optical profilometry, we observe microscopic striations in the sample surface (Figure 4.7B). The long axes of these semiregularly spaced striations in the sample surface run roughly parallel to the IO PC x-axis. These striations are also weakly visible in SEM micrographs taken when the IO PC is tilted 45° (Figure 4.12).

We hypothesize that these IO PC surface striations scatter light similarly to irregularly spaced grooves in a diffraction grating. In diffraction gratings, variations in groove spacing and depth are known to produce diffusely scattered light in the grating dispersion plane, perpendicular to the groove long axis.[273] We propose that the semiregularly spaced striations in our IO PC sample surface resemble irregularly ruled grooves in a diffraction grating, producing in-plane diffuse scattering whose long axis is perpendicular to the striation long axis.

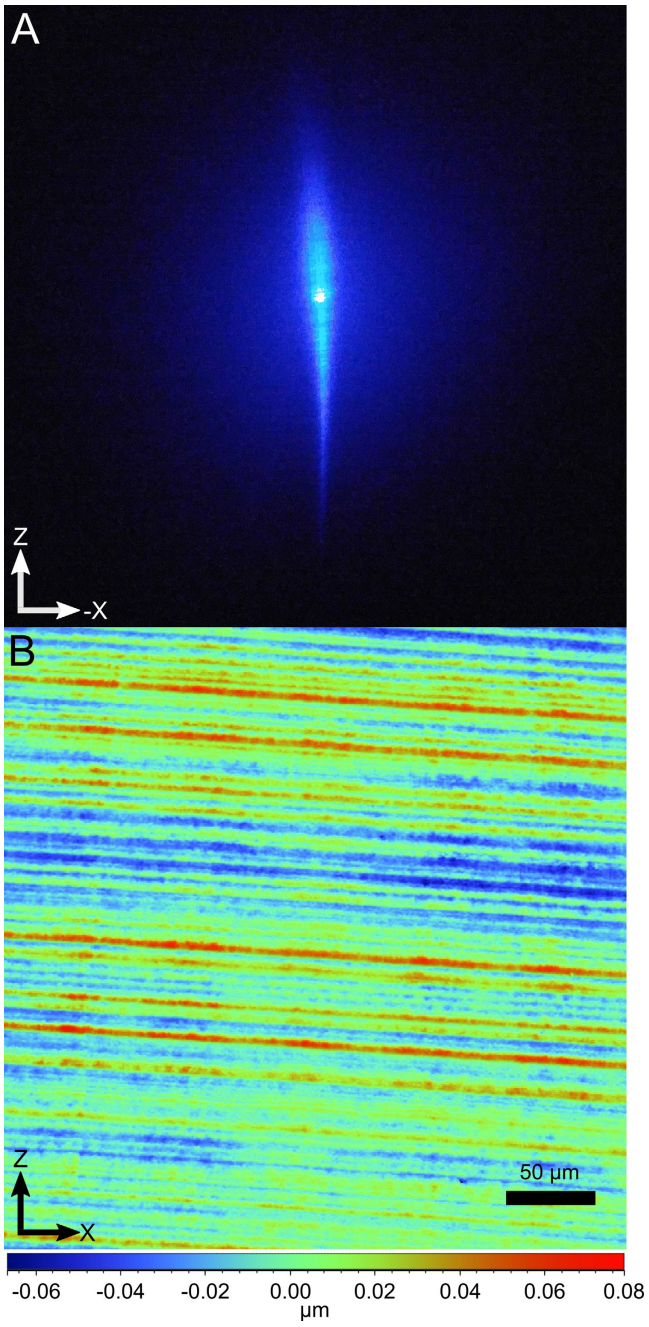

Figure 4.7 – (A) Picture of the 229 nm diffracted beam shape on a luminescent paper viewing screen for the IO PC at a 26.5° IO PC incident angle in air, corresponding to the Bragg condition for 229 nm light. (B) Height map of the strongly diffracting region of the IO PC shown in Figure 4.3 measured using an optical profilometer. The color-bar depicts the height of surface features, where red and blue map colors indicate raised features and depressions, respectively.

These IO PC surface striations lie parallel to the solution surface during vertical deposition. Previous studies have shown that the contact lines of solutions containing dissolved solids exhibit complicated deformation and pinning behaviors during evaporation.[104, 105] In the case of evaporating solutions of nanoparticles, several previous authors have observed the formation of regularly spaced bands of close packed nanoparticles on the substrate that are separated by bare regions containing no nanoparticles,[114, 274, 275] while others have observed continuous films that have periodic variations in thickness as a function of position.[276] We do not observe alternating areas of bare and nanoparticle covered substrate via SEM in the strongly diffracting region of our IO PC. However, we hypothesize that some meniscus deformation occurs during vertical deposition of the PSNPs onto the fused silica substrate, resulting in the semiregular IO PC surface striations observed using the profilometer and 45° tilt SEM. We are currently investigating methods to mitigate the formation of these surface striations during the vertical deposition self-assembly process to minimize their impact on IO PC diffraction.

The 16.8 nm FWHM diffraction bandwidth measured for this IO PC is relatively broad. We expected that the diffraction bandwidth for these IO PCs would be broader than that of our aqueous PCs due to the relatively large refractive index difference between the air voids and the SiO_2 matrix. Increasing the refractive index contrast within a PC increases the scattering strength of the FCC planes, reducing the number of planes taking part in Bragg diffraction. We previously showed that reducing the number of FCC diffraction planes taking part in PC diffraction broadens the diffraction bandwidth.[126] The diffraction bandwidth of these IO PCs can be reduced by infiltrating solvents or UV-transparent polymers into the air-voids to refractive-index-match the voids to the SiO_2 matrix. Disordered regions of the IO PC also broaden the diffracted bandwidth.

We are currently investigating methods to further optimize the modified vertical deposition method to improve IO PC order.

A significant advantage of these solid IO PCs compared to our previous aqueous deep UV diffracting PCs is that they do not depend upon easily disrupted electrostatic interactions between nanoparticles dispersed in solvent to maintain FCC ordering and Bragg diffraction. The solventless SiO_2 FCC structure affords these IO PCs mechanical durability and photochemical stability, enabling them to be repeatedly used and characterized, even under direct laser irradiation. In our previous work, we observed that upon ~2 mW/cm^2 229 nm laser irradiation, the diffraction intensity of our aqueous PCs decreased with time.[261] We illuminated this IO PC with the same 229 nm laser at a 20× higher irradiance of ~41 mW/cm^2 and observed no degradation of our IO PC diffraction intensity.

Furthermore, the mechanical durability of these IO PCs allows them to be easily transported and handled. For example, the IO PC depicted in Figure 4.3 was spectroscopically characterized >10 times and extensively handled for ~4 months prior to SEM imaging. IO PC absorbance spectra collected before and after this extensive handling are nearly identical (Figure 4.13), indicating that time, handling, and deep-UV/near-UV/visible irradiation negligibly impact IO PC diffraction.

These indefinitely shelf stable IO PCs enhance the potential utility of deep UV diffracting PC optical devices by enabling their long-term storage and use. Although further development and optimization of the fabrication procedure are necessary in order to improve their diffraction efficiency and to reduce their diffraction bandwidth, the mechanically robust IO PC fabrication method is extremely promising as an approach to develop deep UV diffracting PC optical devices.

4.4 Conclusion

We demonstrated the first solid IO PCs that diffract in the deep UV at <245 nm. To fabricate these deep UV diffracting IO PCs, we first self-assembled PSNP/SiO_2 3D close-packed FCC PCs by depositing PSNPs onto fused silica substrates in the presence of TEOS solution using a modified vertical deposition method. After studying the diffraction characteristics of the close-packed PSNP/SiO_2 PCs in the near UV, we removed the PSNPs using piranha solution, yielding IO PCs that diffracted at <245 nm. We characterized the diffraction of these IO PCs to determine their utility for use as deep UV optical devices, and found that they show large ~98% attenuations for light that meets the Bragg condition and a 17 nm FWHM diffraction bandwidth. These solid IO PCs show superior mechanical durability, shelf life, and photochemical stability under direct 229 nm laser irradiation compared to our previously demonstrated aqueous based PCs. Further optimization of the vertical deposition procedure is necessary, and we are currently investigating methods to improve IO PC self-assembled order to reduce the diffraction bandwidth, and to decrease the surface roughness to improve the shape and efficiency of the diffracted light.

4.4.1 Acknowledgements

The authors thank Pitt scientific glassblower Lori Neu for fabricating the fused silica substrates used in this work and the Pitt Machine Shop for help in waterproofing the oven. The authors thank Dr. Sergei Bykov and Ryan Jakubek for helpful discussions. The authors received funding from the Office of Naval Research (ONR N00014-16-1-2681 and N00014-18-1-2072).

4.5 Supporting Information

4.5.1 Polystyrene Nanosphere Synthesis

We utilized a modified version of the Reese *et al.*[59] emulsion polymerization procedure previously described by Hufziger *et al.*[170] to synthesize highly charged 138.3 ± 3.1 nm polystyrene nanoparticles (Figure 4.8). A custom 1 L jacketed cylindrical reactor (Ace Glass 6475-310, 4" ID with drain outlet) was fitted with a Teflon agitator (Ace Glass 8090-08 attached to a Teflon shaft) attached to an overhead stirrer (Caframo BDC6015), a reflux condenser, a foil wrapped addition funnel, a long needle to attached to an N_2 line, and a thermometer. The reactor temperature was controlled via an ethylene glycol bath recirculator (Thermo Neslab RTE 740).

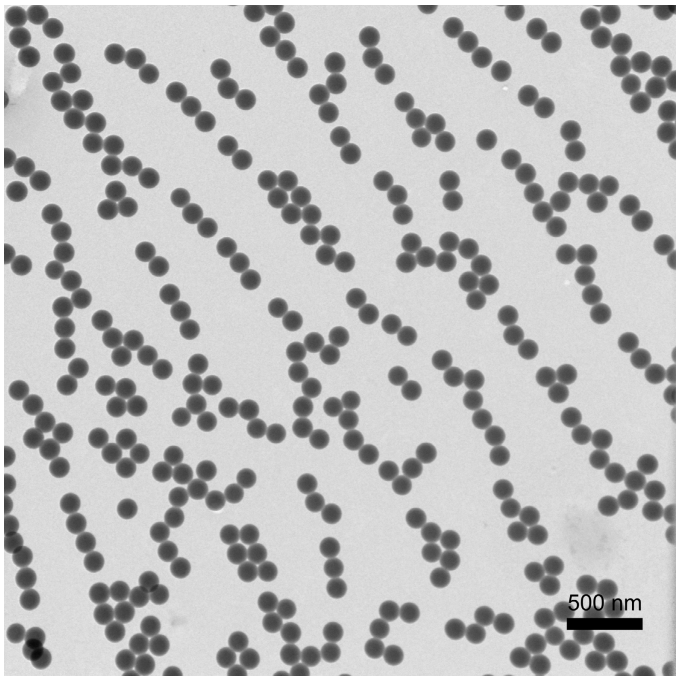

Figure 4.8 – Transmission electron micrograph of 138.3 ± 3.1 nm diameter polystyrene nanoparticles.

Styrene (Sigma Aldrich S4972, 99%) was passed through a column containing ~50 g aluminum oxide (Aldrich 19974) to remove the butylcatechol inhibitor. 275.2 mL ultrapure water (Barnstead Infinity) was added to the reactor, the stirring rate was set to 50 RPM, and then 0.3410 g $NaHCO_3$ (JT Baker 3506-01) was added to the reactor. The reactor contents were deoxygenated for 30 min with N_2. 3.0942 g dihexyl sulfosuccinate sodium salt (Aldrich 86146, ~80% in H_2O, surfactant) was dissolved in 5.00 mL ultrapure water and added to the reactor. The vial containing the surfactant was washed 3x with 5.00 mL aliquots (15 mL total) of ultrapure water, adding each wash into the reactor to maximize surfactant transfer. The reaction mixture was deoxygenated with N_2 for an additional 20 minutes. 115.0 mL deinhibited styrene was added to the addition funnel, and deoxygenated with N_2 for 25 minutes, followed by N_2 blanketing until the end of the reaction.

During styrene deoxygenation, the stirring rate was set to 125 RPM, and reactor heating by the recirculator was initiated. When the reactor temperature reached 45.0 °C, the stir rate was set to 350 RPM and styrene was added at a rate of ~4 drops/sec (22 min total). 5 min after the completion of styrene addition, 6.3030 g 3-allyloxy-2-hydroxy-1-propane sulfonic acid (Aldrich 409421, ~40% w/w in H_2O, co-monomer) was added to the reactor and the recirculator setpoint was increased. When the reactor temperature reached 69.0 °C, 1.5082 g $(NH_4)_2S_2O_8$ (Sigma Aldrich 248614, 98%, initiator) dissolved in 5.00 mL ultrapure water was added to the reactor to initiate the reaction. After allowing the reaction to proceed for 2.0 hrs, 1.0105 g additional co-monomer was added to the reactor, followed 2 min later by 1.0064 g additional $(NH_4)_2S_2O_8$ dissolved in 2.00 mL ultrapure water. The reaction was allowed to proceed for 1.0 hr before being cooled while stirring.

The cooled nanosphere dispersion was filtered through nylon mesh (Small Parts Inc., 40 μm). The dispersion was then poured into 14 kDa MWCO regenerated cellulose tubing (Sigma Aldrich D9402, soaked in ultrapure water before use) and dialyzed against ultrapure water for 5 weeks. The dispersion was then stored over mixed-bed ion-exchange resin (Bio-Rad AG-501-X8 (D), used as provided).

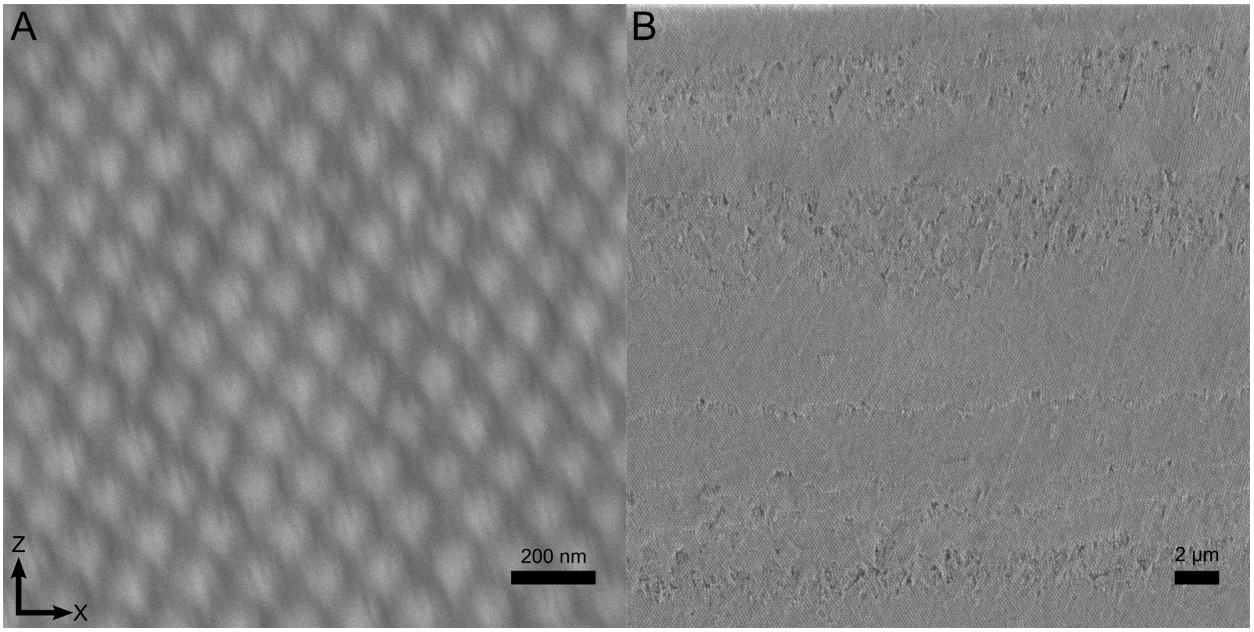

Figure 4.9 – Scanning electron micrographs of an as-fabricated PSNP/SiO_2 PC before nanoparticle removal at high (A) and low (B) magnification. This PC was fabricated under identical conditions to the IO PC depicted in Figure 4.3.

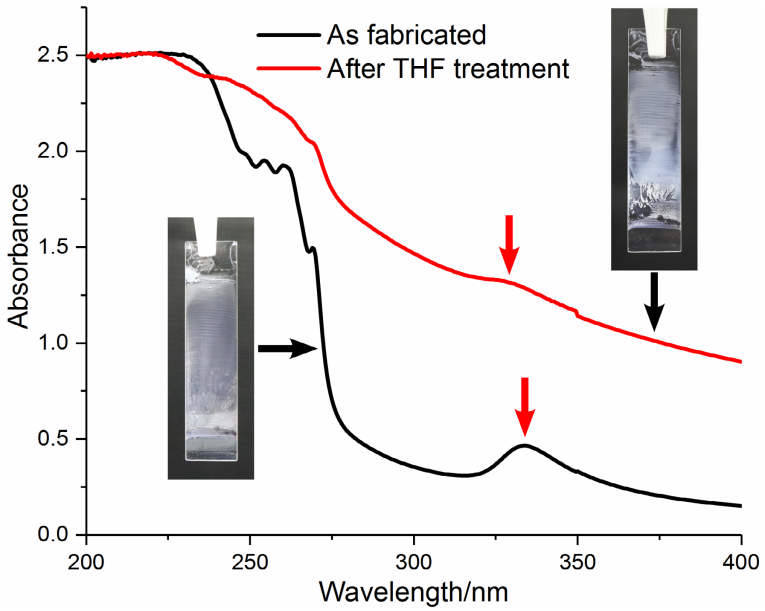

Figure 4.10 – Photographs and absorbance spectra measured using an absorption spectrometer of a PSNP/SiO_2 PC at normal incidence before (black) and after (red) THF treatment. This PC was fabricated under identical conditions to the IO PC depicted in Figure 4.3. This sample was fully immersed in 21.0 mL THF (Fisher Chemical T397) and placed on a mixer for 2 days, replacing the solvent after 1 day, before drying in air. After THF treatment, PC FCC (111) diffraction, indicated by the red arrows, blueshifts slightly but becomes extremely weak, likely due to heterogeneous and incomplete removal of PSNPs from the SiO_2 matrix by THF.

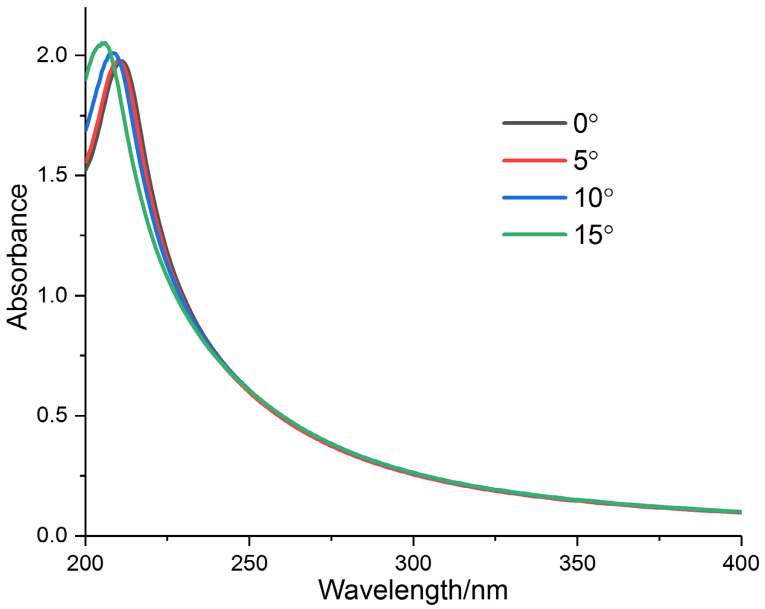

Figure 4.11 – Absorbance spectra of an IO PC fabricated using 114.9 ± 3.4 nm diameter polystyrene nanoparticles, showing strong FCC (111) diffraction at 211 nm at normal incidence. Listed angles are measured in air from the IO PC surface normal.

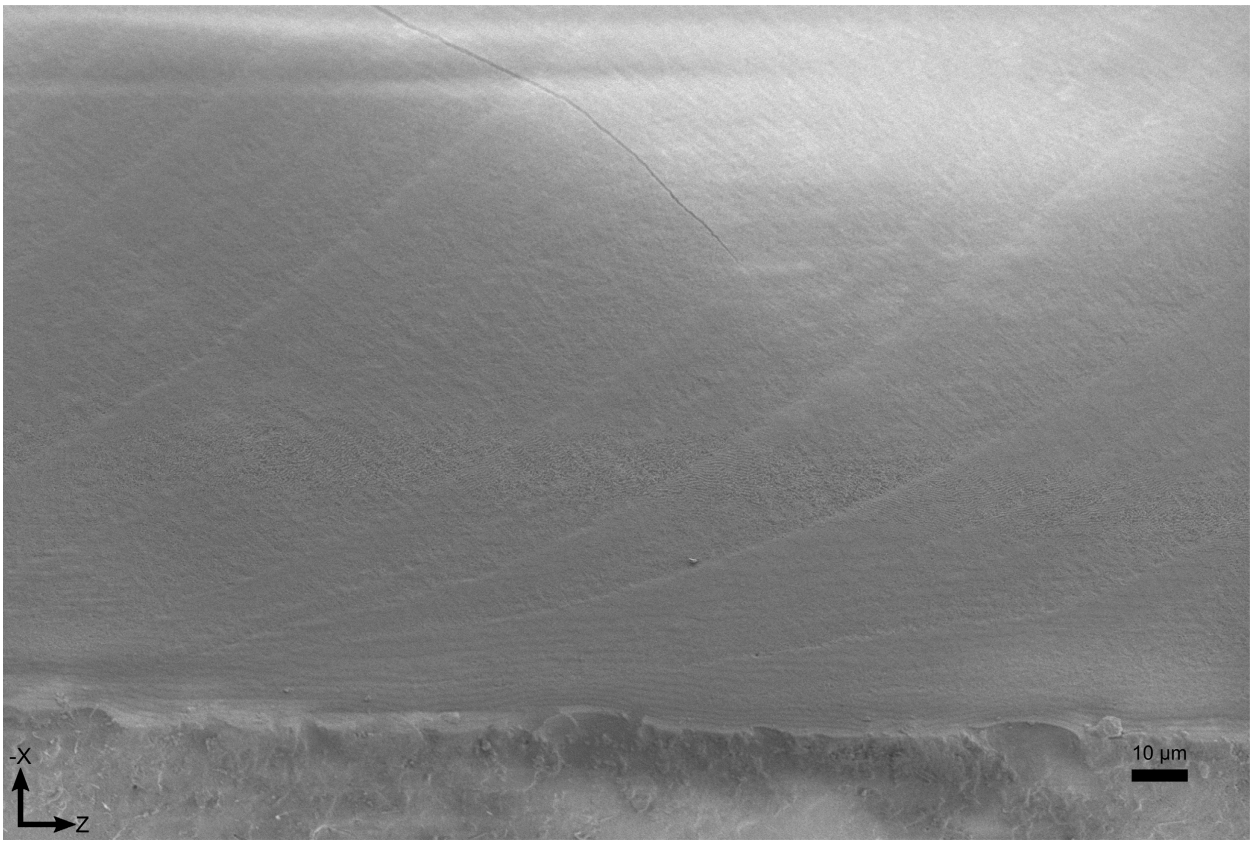

Figure 4.12 – Scanning electron micrograph of the right edge of the strongly diffracting region indicated by the arrow of the IO PC sample shown in Figure 4.3A, tilted at a 45° angle. The banding features near the slide edge are visible as sweeping curves which terminate at the microscope slide edge, visible at the bottom of the micrograph.

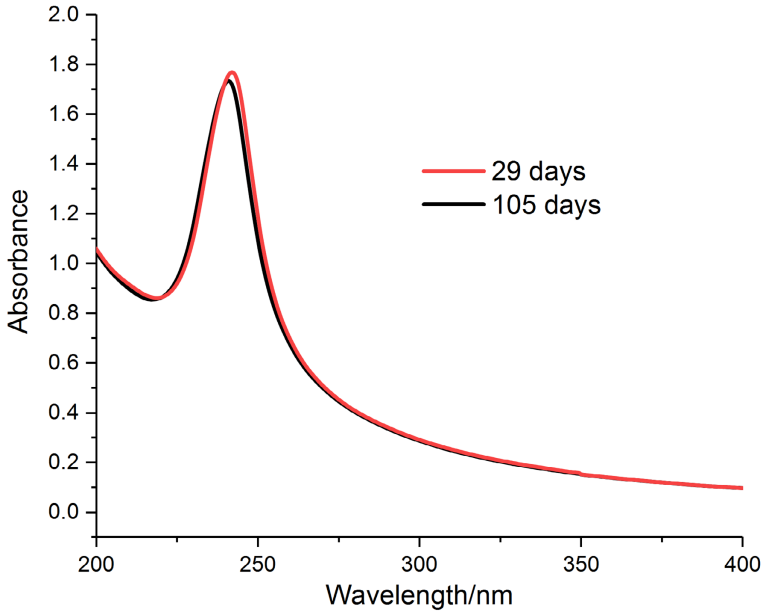

Figure 4.13 – Absorbance spectra of the IO PC depicted in Figure 4.3 at normal incidence shortly after inversion (red) and after the sample was extensively handled and characterized (black). The times listed in the figure denote the number of days that had elapsed between the end of fabrication and the day of spectral collection. The small differences in λ_{max} attenuations and peak positions between the two measurements are likely due to minute positioning and angle differences of the IO PC sample within the cavity of the absorption spectrometer.

4.5.2 Calculation of Photonic Crystal Parameters

To calculate d_{111} and n_{avg}, we measured the absorbance wavelength maxima (λ_{max}) due to FCC (111) diffraction at several different incidence angles using an absorption spectrometer (Figure 4.4, main text). As described by Waterhouse *et al.*,[115] the modified Bragg equation,

$$\textbf{Equation 4.2} \quad \lambda_{max} = \frac{2d_{hkl}}{m}\sqrt{n_{avg}^2 - \sin^2\theta_i}$$

where θ_i is the light incident angle in air measured from the surface normal, can be used to easily extract PC material parameters from the collected diffraction data. We plotted λ_{max}^2 versus $\sin^2(\theta_i)$,

and fit them with a linear fit (Figure 4.4, insets). The slope and y-axis intercept of the linear fit equal $-(2d_{hkl})^2$ and $(2d_{hkl})^2 n_{avg}^2$, respectively.

5.0 Chapter 5: Summary of the Development of Photonic Crystal Optics and Wide-field Raman Imaging Spectrometers for Trace Explosive Detection

In this dissertation work, we developed photonic crystal devices and wide-field Raman imaging spectrometers to advance the state of the art in deep UV optics and standoff explosive detection. In Chapter 2.0, we describe the development of the first wide-field Raman imaging spectrometer utilizing a photonic crystal as the wavelength selection device. In that work, we synthesized and utilized highly negatively charged 102.7 ± 4.1 nm diameter polystyrene nanospheres to form non-close-packed FCC photonic crystals. We demonstrated that the FCC (111) planes in these photonic crystals Bragg diffract a ~9 nm FWHM spectral region of visible light. We utilized these photonic crystals inside a novel, specially constructed wide-field Raman imaging spectrometer to diffract a Raman spectral region containing -CCC- bending, -CC- stretching, and $-CF_2$ antisymmetric stretching bands from a Teflon sample. We focused the diffracted light into a spectrometer to confirm the ability of the photonic crystal to select a particular Raman spectral region while rejecting other, nearby Raman bands.

We also focused this diffracted Raman light onto a CCD camera, forming a wide-field Raman image with a 5 sec accumulation time that allowed us to chemically differentiate between Teflon and an NaCl feature placed on the surface of the Teflon. These proof of concept studies involving this novel wide-field Raman imaging spectrometer confirmed the utility of photonic crystals as wide-field imaging optics and validated our hypothesized spectrometer design, enabling the construction of more sophisticated instrumentation in the much more difficult to access deep UV spectral region.

In Chapter 3.0 we described the development of the first deep UV wide-field Raman imaging spectrometer. In that work, we synthesized highly negatively charged 35.5 ± 2.9 nm diameter silica nanoparticles to fabricate non-close-packed FCC photonic crystals. We selected the small size and concentration of these nanoparticles such that they Bragg diffracted light in the deep UV spectral region at ~235 nm, which corresponds to the spectral region of Stokes scattered Raman light for samples excited by 229 nm laser light. We characterized the precise spectral bandwidth of the (111) Bragg diffraction using monochromatic 229 nm laser light. We determined that the spectral bandwidth measured using an absorption spectrometer, which utilizes uncollimated light, is ~4x broader than is measured when well collimated 229 nm laser light is used.

We then utilized these well characterized photonic crystals to construct a wide-field Raman imaging spectrometer that we utilized for standoff trace explosive detection. This spectrometer utilized a deep UV optimized Maksutov-Cassegrain telescope to collect Raman light scattered by samples 2.3 m distant that were excited by a 1.2 × 1.2 cm 229 nm laser beam. We demonstrated that 120 μg spots of PETN and AN drop cast onto an aluminum plate could be easily chemically differentiated using just two Raman images. We also demonstrated that 10 $\mu g/cm^2$ samples of PETN and AN that were inkjet deposited onto aluminum test panels could be imaged and detected in 30 sec. Given these results, we estimated that 1 $\mu g/cm^2$ detection limits are achievable using this instrument under these conditions. In summary, we demonstrated the feasibility of deep UV wide-field imaging for standoff trace explosive detection and the utility of deep UV diffracting photonic crystal optics.

In Chapter 4.0 we described the development of the first deep UV diffracting inverse opal photonic crystal. This goal of this project was to increase the mechanical durability of deep UV

diffracting photonic crystals. In our deep UV wide-field imaging work described in Chapter 3.0, we observed that direct irradiation of the aqueous photonic crystal with a deep UV laser resulted in a decrease in the Bragg diffraction efficiency with time, which we hypothesized was due to the production of impurity electrolytes that screened electrostatic interactions between nanoparticles and disordered the FCC array. To produce a photonic crystal with enhanced mechanical properties, we synthesized 138.3 ± 3.1 nm diameter polystyrene nanoparticles that we used to create solvent-free photonic crystals. We utilized a modified vertical deposition procedure to deposit these polystyrene nanoparticles into FCC arrays on fused silica substrates. The self-assembly occurred in the presence of the silica precursor TEOS, which condensed around the nanoparticles to embed them in a solid SiO_2 matrix. We then removed the polystyrene nanospheres with Piranha solution, which leaves the SiO_2 matrix intact, to form inverse opals that diffracted in the deep UV at ~240 nm.

We thoroughly characterized the optical behavior of a representative inverse opal photonic crystal using collimated white light and 229 nm laser light and found that this photonic crystal was ~3600 nm thick and showed a 17 nm FWHM diffraction bandwidth. We characterized the surface morphology of this sample via optical profilometry and found that it exhibited regularly repeating, linear surface striations that likely result in the spatial broadening of the diffracted 229 nm laser light, which was observed during diffraction bandwidth measurements. Importantly, we observed that these photonic crystals were extremely mechanically robust and showed nearly identical diffraction before and after they had been repeatedly characterized using deep UV light and extensively handled. In conclusion, in this work we invented and demonstrated the feasibility of long shelf-life, mechanically stable deep UV diffracting inverse opal photonic crystals.

In summary, in this work we developed novel deep UV diffracting photonic crystal optics and deep UV wide-field Raman imaging spectrometers for trace explosive detection. We demonstrated that these photonic crystals enable deep UV imaging spectroscopy that was not previously feasible due to the lack of commercially available optical devices in this spectral region. Furthermore, we developed a technique to enhance the mechanical characteristics and shelf life of these photonic crystals, which drastically increases their utility as deep UV optical devices.

Bibliography

1. C. K. Muro, K. C. Doty, J. Bueno, L. Halámková, and I. K. Lednev, "Vibrational Spectroscopy: Recent Developments to Revolutionize Forensic Science". Anal. Chem. 2015. 87(1): 306-327.

2. M. Marshall and J. C. Oxley, *Aspects of Explosives Detection*. Oxford: Elsevier, 2009.

3. National Consortium for the Study of Terrorism and Responses to Terrorism (START). (2016). Global Terrorism Database [Data file]. Retrieved from https://www.start.umd.edu/gtd

4. C. J. Cumming, C. Aker, M. Fisher, M. Fok, M. J. La Grone, D. Reust, M. G. Rockley, T. M. Swager, E. Towers, and V. Williams, "Using Novel Fluorescent Polymers as Sensory Materials for Above-Ground Sensing of Chemical Signature Compounds Emanating from Buried Landmines". IEEE T. Geosci. Remote. 2001. 39(6): 1119-1128.

5. E. D. Emmons, A. Tripathi, J. A. Guicheteau, S. D. Christesen, and A. W. Fountain, "Raman Chemical Imaging of Explosive-Contaminated Fingerprints". Appl. Spectrosc. 2009. 63(11): 1197-1203.

6. V. Nguyen, M. Papantonakis, R. Furstenberg, C. Kendziora, and R. A. McGill, "Real-World Particulate Explosives Test Coupons for Optical Detection Applications". SPIE Defense, Security, and Sensing. 2013. pp. 1-10.

7. D. S. Moore, "Recent Advances in Trace Explosives Detection Instrumentation". Sens. Imaging. 2007. 8(1): 9-38.

8. G. A. Eiceman, Z. Karpas, and H. H. Hill Jr, "Detection of Explosives by IMS", *Ion Mobility Spectrometry*. Boca Raton: CRC press, 2013. 12, pp. 269-287.

9. P. M. Pellegrino, E. L. Holthoff, and M. E. Farrell, *Laser-Based Optical Detection of Explosives*. Boca Raton, FL: CRC Press, 2015.

10. S. A. Asher, "UV Resonance Raman Spectroscopy for Analytical, Physical, and Biophysical Chemistry Part 1". Anal. Chem. 1993. 65(2): 59A-66A.

11. D. S. Moore and R. J. Scharff, "Portable Raman Explosives Detection". Anal. Bioanal. Chem. 2009. 393(6): 1571-1578.

12. M. P. Nelson and P. J. Treado, "Raman Imaging Instrumentation", In: S. Sasic and Y. Ozaki (eds) *Raman, Infrared, and Near-Infrared Chemical Imaging*. Hoboken: John Wiley & Sons, 2011. 2, pp. 23-51.

13. G. Puppels, M. Grond, and J. Greve, "Direct Imaging Raman Microscope Based on Tunable Wavelength Excitation and Narrow-band Emission Detection". Appl. Spectrosc. 1993. 47(8): 1256-1267.

14. H. Östmark, M. Nordberg, and T. E. Carlsson, "Stand-off Detection of Explosives Particles by Multispectral Imaging Raman Spectroscopy". Appl. Opt. 2011. 50(28): 5592-5599.

15. L. Wang, A. Tikhonov, and S. A. Asher, "Silica Crystalline Colloidal Array Deep Ultraviolet Narrow-band Diffraction Devices". Appl. Spectrosc. 2012. 66(4): 426-431.

16. S. A. Asher and P. Flaugh, "Crystalline Colloidal Bragg Diffraction Devices: The Basis for a New Generation of Raman Instrumentation". Spectroscopy. 1986. 1(12): 26-31.

17. J. Ferraro and K. Nakamoto, *Introductory Raman Spectroscopy*. Boston: Academic Press, Inc, 2003.

18. E. Smith and G. Dent, *Modern Raman Spectroscopy: A Practical Approach*. John Wiley & Sons, 2005.

19. D. A. Long, *The Raman Effect*. West Sussex, England: John Wiley & Sons, 2002.

20. S. A. Asher, "UV Resonance Raman Studies of Molecular Structure and Dynamics: Applications in Physical and Biophysical Chemistry". Annu. Rev. Phys. Chem. 1988. 39(1): 537-588.

21. S. A. Asher, "Ultraviolet Raman Spectrometry", In: J. M. Chalmers and P. R. Griffiths (eds) *Handbook of Vibrational Spectroscopy*. J. Wiley, 2002. pp. 1-15.

22. R. J. Clarke and A. Oprysa, "Fluorescence and Light Scattering". J. Chem. Educ. 2004. 81(5): 705-707.

23. S. A. Oladepo, K. Xiong, Z. Hong, S. A. Asher, J. Handen, and I. K. Lednev, "UV Resonance Raman Investigations of Peptide and Protein Structure and Dynamics". Chem. Rev. 2012. 112(5): 2604-2628.

24. A. K. Misra, S. K. Sharma, T. E. Acosta, J. N. Porter, and D. E. Bates, "Single-Pulse Standoff Raman Detection of Chemicals from 120 m Distance During Daytime". Appl. Spectrosc. 2012. 66(11): 1279-1285.

25. J. C. Carter, S. M. Angel, M. Lawrence-Snyder, J. Scaffidi, R. E. Whipple, and J. G. Reynolds, "Standoff Detection of High Explosive Materials at 50 Meters in Ambient Light Conditions Using a Small Raman Instrument". Appl. Spectrosc. 2005. 59(6): 769-775.

26. D. D. Tuschel, A. V. Mikhonin, B. E. Lemoff, and S. A. Asher, "Deep Ultraviolet Resonance Raman Excitation Enables Explosives Detection". Appl. Spectrosc. 2010. 64(4): 425-432.

27. E. D. Emmons, A. Tripathi, J. A. Guicheteau, A. W. Fountain III, and S. D. Christesen, "Ultraviolet Resonance Raman Spectroscopy of Explosives in Solution and the Solid State". J. Phys. Chem. A. 2013. 117(20): 4158-4166.

28. A. G. Marshall, "Chapter 13: The Driven, Damped Weight on a Spring: One of the Most Important Problems in Physical Science", *Biophysical Chemistry: Principles, Techniques, and Applications*. New York: John Wiley and Sons, 1978. pp. 361-383.

29. M. Ghosh, L. Wang, and S. A. Asher, "Deep-Ultraviolet Resonance Raman Excitation Profiles of NH_4NO_3, PETN, TNT, HMX, and RDX". Appl. Spectrosc. 2012. 66(9): 1013-1021.

30. K. L. Gares, S. V. Bykov, and S. A. Asher, "UV Resonance Raman Investigation of Pentaerythritol Tetranitrate Solution Photochemistry and Photoproduct Hydrolysis". J. Phys. Chem. A. 2017. 121(41): 7889-7894.

31. K. L. Gares, S. V. Bykov, B. Godugu, and S. A. Asher, "Solution and Solid Trinitrotoluene (TNT) Photochemistry: Persistence of TNT-like Ultraviolet (UV) Resonance Raman Bands". Appl. Spectrosc. 2013. 68(1): 49-56.

32. K. L. Gares, S. V. Bykov, T. Brinzer, and S. A. Asher, "Solution and Solid Hexahydro-1,3,5-trinitro-1,3,5-triazine (RDX) Ultraviolet (UV) 229 nm Photochemistry". Appl. Spectrosc. 2015. 69(5): 545-554.

33. A. W. Fountain, S. D. Christesen, R. P. Moon, J. A. Guicheteau, and E. D. Emmons, "Recent Advances and Remaining Challenges for the Spectroscopic Detection of Explosive Threats". Appl. Spectrosc. 2014. 68(8): 795-811.

34. H. R. Morris, C. C. Hoyt, P. Miller, and P. J. Treado, "Liquid Crystal Tunable Filter Raman Chemical Imaging". Appl. Spectrosc. 1996. 50(6): 805-811.

35. H. R. Morris, C. C. Hoyt, and P. J. Treado, "Imaging Spectrometers for Fluorescence and Raman Microscopy: Acousto-Optic and Liquid Crystal Tunable Filters". Appl. Spectrosc. 1994. 48(7): 857-866.

36. M. Iga, N. Kakuryu, T. Tanaami, J. Sajiki, K. Isozaki, and T. Itoh, "Development of Thin-film Tunable Band-pass Filters Based Hyper-Spectral Imaging System Applied for Both Surface Enhanced Raman Scattering and Plasmon Resonance Rayleigh Scattering". Rev. Sci. Instrum. 2012. 83(10): 103707.

37. J. D. Joannopoulos, S. G. Johnson, J. N. Winn, and R. D. Meade, *Photonic Crystals: Molding the Flow of Light*. Princeton: Princeton University Press, 2011.

38. H. C. Van De Hulst, *Light Scattering by Small Particles*. New York: Courier Dover Publications, 1957.

39. E. Hecht, *Optics*. Addison-Wesley, 1998.

40. Y. Chen, X. Zang, J. Gu, S. Zhu, H. Su, D. Zhang, X. Hu, Q. Liu, W. Zhang, and D. Liu, "ZnO Single Butterfly Wing Scales: Synthesis and Spatial Optical Anisotropy". J. Mater. Chem. 2011. 21(17): 6140-6143.

41. J. W. Galusha, L. R. Richey, J. S. Gardner, J. N. Cha, and M. H. Bartl, "Discovery of a Diamond-Based Photonic Crystal Structure in Beetle Scales". Phys. Rev. E. 2008. 77(5): 1-4.

42. S. H. Cole and E. Monroe, "Electron Microscope Studies of the Structure of Opal". J. Appl. Phys. 1967. 38(4): 1872-1873.

43. S.-H. Kim and G.-R. Yi, "Colloidal Photonic Crystals for Sensor Applications", In: J. M. Serpe, Y. Kang and M. Q. Zhang (eds) *Photonic Materials for Sensing, Biosensing and Display Devices*. Springer International Publishing, 2016. pp. 51-78.

44. P. Flaugh, S. O'Donnell, and S. A. Asher, "Development of a New Optical Wavelength Rejection Filter: Demonstration of Its Utility in Raman Spectroscopy". Appl. Spectrosc. 1984. 38(6): 847-850.

45. S. Takahashi, K. Suzuki, M. Okano, M. Imada, T. Nakamori, Y. Ota, K. Ishizaki, and S. Noda, "Direct Creation of Three-Dimensional Photonic Crystals by a Top-down Approach". Nat. Mater. 2009. 8: 721-725.

46. G. von Freymann, A. Ledermann, M. Thiel, I. Staude, S. Essig, K. Busch, and M. Wegener, "Three-Dimensional Nanostructures for Photonics". Adv. Funct. Mater. 2010. 20(7): 1038-1052.

47. G. von Freymann, V. Kitaev, B. V. Lotsch, and G. A. Ozin, "Bottom-up assembly of photonic crystals". Chem. Soc. Rev. 2013. 42(7): 2528-2554.

48. I. Freestone, N. Meeks, M. Sax, and C. Higgitt, "The Lycurgus Cup — A Roman Nanotechnology". Gold Bull. 2007. 40(4): 270-277.

49. C. E. Reese and S. A. Asher, "Emulsifier-Free Emulsion Polymerization Produces Highly Charged, Monodisperse Particles for Near Infrared Photonic Crystals". J. Colloid Interface Sci. 2002. 248(1): 41-46.

50. E. Redel, P. Mirtchev, C. Huai, S. Petrov, and G. A. Ozin, "Nanoparticle Films and Photonic Crystal Multilayers from Colloidally Stable, Size-Controllable Zinc and Iron Oxide Nanoparticles". ACS Nano. 2011. 5(4): 2861-2869.

51. T.-Y. Wu, A. B. Zrimsek, S. V. Bykov, R. S. Jakubek, and S. A. Asher, "Hydrophobic Collapse Initiates the Poly(N-isopropylacrylamide) Volume Phase Transition Reaction Coordinate". J. Phys. Chem. B. 2018. 122(11): 3008-3014.

52. A. S. Sinitskii, P. E. Khokhlov, V. V. Abramova, T. V. Laptinskaya, and Y. D. Tretyakov, "Optical Study of Photonic Crystal Films Made of Polystyrene Microspheres". Mendeleev Commun. 2007. 17(1): 4-6.

53. B. Hatton, L. Mishchenko, S. Davis, K. H. Sandhage, and J. Aizenberg, "Assembly of large-area, highly ordered, crack-free inverse opal films". Proc. Natl. Acad. Sci. U. S. A. 2010. 107(23): 10354-10359.

54. C. S. Chern, "Emulsion Polymerization Mechanisms and Kinetics". Prog. Polym. Sci. 2006. 31(5): 443-486.

55. C.-S. Chern, *Principles and Applications of Emulsion Polymerization*. Hoboken: John Wiley & Sons, 2008.

56. W. D. Harkins, "A General Theory of the Mechanism of Emulsion Polymerization". JACS. 1947. 69(6): 1428-1444.

57. W. V. Smith and R. H. Ewart, "Kinetics of Emulsion Polymerization". J. Chem. Phys. 1948. 16(6): 592-599.

58. S. C. Thickett and R. G. Gilbert, "Emulsion Polymerization: State of the Art in Kinetics and Mechanisms". Polymer. 2007. 48(24): 6965-6991.

59. C. Reese, C. Guerrero, J. Weissman, K. Lee, and S. Asher, "Synthesis of Highly Charged, Monodisperse Polystyrene Colloidal Particles for the Fabrication of Photonic Crystals". J. Colloid Interface Sci. 2000. 232(1): 76-80.

60. L. Bai, Z. Xie, W. Wang, C. Yuan, Y. Zhao, Z. Mu, Q. Zhong, and Z. Gu, "Bio-Inspired Vapor-Responsive Colloidal Photonic Crystal Patterns by Inkjet Printing". ACS Nano. 2014. 8(11): 11094-11100.

61. H. S. Lee, T. S. Shim, H. Hwang, S.-M. Yang, and S.-H. Kim, "Colloidal Photonic Crystals toward Structural Color Palettes for Security Materials". Chem. Mater. 2013. 25(13): 2684-2690.

62. P. Jiang and M. J. McFarland, "Large-scale Fabrication of Wafer-size Colloidal Crystals, Macroporous Polymers and Nanocomposites by Spin-Coating". JACS. 2004. 126(42): 13778-13786.

63. S. Wong, V. Kitaev, and G. A. Ozin, "Colloidal Crystal Films: Advances in Universality and Perfection". JACS. 2003. 125(50): 15589-15598.

64. P. Jiang, J. F. Bertone, K. S. Hwang, and V. L. Colvin, "Single-Crystal Colloidal Multilayers of Controlled Thickness". Chem. Mater. 1999. 11(8): 2132-2140.

65. W. Stöber, A. Fink, and E. Bohn, "Controlled Growth of Monodisperse Silica Spheres in the Micron Size Range". J. Colloid Interface Sci. 1968. 26(1): 62-69.

66. T. Yokoi, J. Wakabayashi, Y. Otsuka, W. Fan, M. Iwama, R. Watanabe, K. Aramaki, A. Shimojima, T. Tatsumi, and T. Okubo, "Mechanism of Formation of Uniform-Sized Silica Nanospheres Catalyzed by Basic Amino Acids". Chem. Mater. 2009. 21(15): 3719-3729.

67. K. D. Hartlen, A. P. T. Athanasopoulos, and V. Kitaev, "Facile Preparation of Highly Monodisperse Small Silica Spheres (15 to >200 nm) Suitable for Colloidal Templating and Formation of Ordered Arrays". Langmuir. 2008. 24(5): 1714-1720.

68. J. E. Lofgreen and G. A. Ozin, "Controlling Morphology and Porosity to Improve Performance of Molecularly Imprinted Sol-gel Silica". Chem. Soc. Rev. 2014. 43(3): 911-933.

69. T. Matsoukas and E. Gulari, "Dynamics of Growth of Silica Particles from Ammonia-Catalyzed Hydrolysis of Tetra-Ethyl-Orthosilicate". J. Colloid Interface Sci. 1988. 124(1): 252-261.

70. T. Matsoukas and E. Gulari, "Monomer-Addition Growth with a Slow Initiation Step: A Growth Model for Silica Particles from Alkoxides". J. Colloid Interface Sci. 1989. 132(1): 13-21.

71. A. Van Blaaderen, J. Van Geest, and A. Vrij, "Monodisperse Colloidal Silica Spheres from Tetraalkoxysilanes: Particle Formation and Growth Mechanism". J. Colloid Interface Sci. 1992. 154(2): 481-501.

72. V. K. LaMer and R. H. Dinegar, "Theory, Production and Mechanism of Formation of Monodispersed Hydrosols". JACS. 1950. 72(11): 4847-4854.

73. G. H. Bogush and C. F. Zukoski Iv, "Uniform Silica Particle Precipitation: An Aggregative Growth Model". J. Colloid Interface Sci. 1991. 142(1): 19-34.

74. G. Bogush, M. Tracy, and C. Zukoski Iv, "Preparation of Monodisperse Silica Particles: Control of Size and Mass Fraction". J. Non-Cryst. Solids. 1988. 104(1): 95-106.

75. C. C. Carcouët, M. W. van de Put, B. Mezari, P. C. Magusin, J. Laven, P. H. Bomans, H. Friedrich, A. C. C. Esteves, N. A. Sommerdijk, and R. A. van Benthem, "Nucleation and Growth of Monodisperse Silica Nanoparticles". Nano Lett. 2014. 14(3): 1433-1438.

76. H. Boukari, G. G. Long, and M. Harris, "Polydispersity During the Formation and Growth of the Stöber Silica Particles from Small-Angle X-ray Scattering Measurements". J. Colloid Interface Sci. 2000. 229(1): 129-139.

77. Y. Han, Z. Lu, Z. Teng, J. Liang, Z. Guo, D. Wang, M.-Y. Han, and W. Yang, "Unraveling the Growth Mechanism of Silica Particles in the Stöber Method: In Situ Seeded Growth Model". Langmuir. 2017. 33(23): 5879-5890.

78. I. D. Morrison and S. Ross, *Colloidal Dispersions: Suspensions, Emulsions, and Foams*. New York: John Wiley and Sons, 2002.

79. W. B. Russel, D. A. Saville, and W. R. Schowalter, *Colloidal Dispersions*. Cambridge: Cambridge University Press, 1992.

80. F. London, "The General Theory of Molecular Forces". T. Faraday. Soc. 1937. 33(0): 8-26.

81. V. A. Parsegian, *Van der Waals Forces: A Handbook for Biologists, Chemists, Engineers, and Physicists*. Cambridge: Cambridge University Press, 2005.

82. H. C. Hamaker, "The London—van der Waals Attraction Between Spherical Particles". Physica. 1937. 4(10): 1058-1072.

83. E. M. Lifshitz, "The Theory of Molecular Attractive Forces Between Solids". Soviet Physics. 1956. 2(1): 73-83.

84. D. F. Evans and H. Wennerstrom, *The Colloidal Domain: Where Physics, Chemistry, Biology, and Technology Meet*. New York: Wiley-VCH, 1999.

85. P. A. Hiltner and I. M. Krieger, "Diffraction of Light by Ordered Suspensions". J. Phys. Chem. 1969. 73(7): 2386-2389.

86. J. C. Zahorchak, R. Kesavamoorthy, R. D. Coalson, and S. A. Asher, "Melting of Colloidal Crystals: A Monte Carlo Study". J. Chem. Phys. 1992. 96(9): 6873-6879.

87. H.-J. Butt, K. Graf, and M. Kappl, "Charged Interfaces and the Electric Double Layer", *Physics and Chemistry of Interfaces*. Weinheim: John Wiley & Sons, 2013. pp. 57-98.

88. Q. Li, U. Jonas, X. S. Zhao, and M. Kappl, "The Forces at Work in Colloidal Self-Assembly: A Review on Fundamental Interactions Between Colloidal Particles". Asia-Pac. J. Chem. Eng. 2008. 3(3): 255-268.

89. S. Hachisu, Y. Kobayashi, and A. Kose, "Phase Separation in Monodisperse Latexes". J. Colloid Interface Sci. 1973. 42(2): 342-348.

90. W. Luck, M. Klier, and H. Wesslau, "Über Bragg-Reflexe mit Sichtbarem Licht an Monodispersen Kunststofflatices. I". Berichte der Bunsengesellschaft für physikalische Chemie. 1963. 67(1): 75-83.

91. D. Frenkel, "Entropy-Driven Phase Transitions". Phys. A (Amsterdam, Neth.). 1999. 263(1): 26-38.

92. V. N. Manoharan, "Colloidal Matter: Packing, Geometry, and Entropy". Science. 2015. 349(6251): 942-949.

93. D. Frenkel, "Introduction to Colloidal Systems", In: W. C. Poon and D. Andelman (eds) *Soft condensed matter physics in molecular and cell biology*. CRC Press, 2006.

94. T. C. Lubensky, "Soft Condensed Matter Physics". Solid State Commun. 1997. 102(2): 187-197.

95. H. Lekkerkerker, "Ordering in Supramolecular Fluids". Physica A. 1991. 176: 1-15.

96. P. A. Rundquist, P. Photinos, S. Jagannathan, and S. A. Asher, "Dynamical Bragg Diffraction from Crystalline Colloidal Arrays". J. Chem. Phys. 1989. 91(8): 4932-4941.

97. W. van Megen and I. Snook, "Ordered States in Systems of Macroscopic Particles". Nature. 1976. 262(5569): 571-572.

98. W. van Megen and I. Snook, "Structure and Ordering in Dilute Dispersions of Spherical Particles". J. Chem. Phys. 1977. 66(2): 813-817.

99. L. V. Woodcock, "Entropy Difference Between the Face-Centred Cubic and Hexagonal Close-Packed Crystal Structures". Nature. 1997. 385: 141-143.

100. N. Vogel, M. Retsch, C.-A. Fustin, A. del Campo, and U. Jonas, "Advances in Colloidal Assembly: The Design of Structure and Hierarchy in Two and Three Dimensions". Chem. Rev. 2015. 115(13): 6265-6311.

101. B. Prevo and O. Velev, "Materials Deposition in Evaporating Menisci—Fundamentals and Engineering Applications of the Convective Assembly Process", *Evaporative Self-Assembly Of Ordered Complex Structures*. World Scientific, 2012. pp. 109-155.

102. P.-G. De Gennes, F. Brochard-Wyart, and D. Quéré, *Capillarity and Wetting Phenomena: Drops, Bubbles, Pearls, Waves*. New York: Springer Science & Business Media, 2003.

103. P. Born, S. Blum, A. Munoz, and T. Kraus, "Role of the Meniscus Shape in Large-Area Convective Particle Assembly". Langmuir. 2011. 27(14): 8621-8633.

104. R. D. Deegan, O. Bakajin, T. F. Dupont, G. Huber, S. R. Nagel, and T. A. Witten, "Contact Line Deposits in an Evaporating Drop". Phys. Rev. E: Stat. Phys., Plasmas, Fluids, Relat. Interdiscip. Top. 2000. 62(1): 756-765.

105. E. Adachi, A. S. Dimitrov, and K. Nagayama, "Stripe Patterns Formed on a Glass Surface During Droplet Evaporation". Langmuir. 1995. 11(4): 1057-1060.

106. N. Denkov, O. Velev, P. Kralchevski, I. Ivanov, H. Yoshimura, and K. Nagayama, "Mechanism of Formation of Two-Dimensional Crystals from Latex Particles on Substrates". Langmuir. 1992. 8(12): 3183-3190.

107. K. T. Hufziger, A. B. Zrimsek, and S. A. Asher, "Solid Deep Ultraviolet Diffracting Inverse Opal Photonic Crystals". ACS Appl. Nano Mater. 2018. 1(12): 7016-7024.

108. P. Born, A. Munoz, C. Cavelius, and T. Kraus, "Crystallization Mechanisms in Convective Particle Assembly". Langmuir. 2012. 28(22): 8300-8308.

109. P. A. Kralchevsky and K. Nagayama, "Capillary Forces Between Colloidal Particles". Langmuir. 1994. 10(1): 23-36.

110. L. Meng, H. Wei, A. Nagel, B. J. Wiley, L. E. Scriven, and D. J. Norris, "The Role of Thickness Transitions in Convective Assembly". Nano Lett. 2006. 6(10): 2249-2253.

111. L. Yang, K. Gao, Y. Luo, J. Luo, D. Li, and Q. Meng, "In Situ Observation and Measurement of Evaporation-Induced Self-Assembly Under Controlled Pressure and Temperature". Langmuir. 2011. 27(5): 1700-1706.

112. D. D. Brewer, J. Allen, M. R. Miller, J. M. de Santos, S. Kumar, D. J. Norris, M. Tsapatsis, and L. E. Scriven, "Mechanistic Principles of Colloidal Crystal Growth by Evaporation-Induced Convective Steering". Langmuir. 2008. 24(23): 13683-13693.

113. D. J. Norris, E. G. Arlinghaus, L. Meng, R. Heiny, and L. Scriven, "Opaline Photonic Crystals: How Does Self-Assembly Work?". Adv. Mater. 2004. 16(16): 1393-1399.

114. C. N. Kaplan, N. Wu, S. Mandre, J. Aizenberg, and L. Mahadevan, "Dynamics of Evaporative Colloidal Patterning". Phys. Fluids. 2015. 27(9): 1-17.

115. G. I. N. Waterhouse and M. R. Waterland, "Opal and inverse opal photonic crystals: Fabrication and characterization". Polyhedron. 2007. 26(2): 356-368.

116. A. Arsenault, F. Fleischhaker, G. von Freymann, V. Kitaev, H. Miguez, A. Mihi, N. Tétreault, E. Vekris, I. Manners, S. Aitchison, D. Perovic, and G. A. Ozin, "Perfecting Imperfection—Designer Defects in Colloidal Photonic Crystals". Adv. Mater. 2006. 18(20): 2779-2785.

117. F. Marlow, P. Sharifi, R. Brinkmann, and C. Mendive, "Opals: Status and Prospects". Angew. Chem. Int. Ed. 2009. 48(34): 6212-6233.

118. S.-Y. Lin, E. Chow, V. Hietala, P. R. Villeneuve, and J. Joannopoulos, "Experimental Demonstration of Guiding and Bending of Electromagnetic Waves in a Photonic Crystal". Science. 1998. 282(5387): 274-276.

119. S. A. Rinne, F. García-Santamaría, and P. V. Braun, "Embedded Cavities and Waveguides in Three-Dimensional Silicon Photonic Crystals". Nat. Photonics. 2007. 2: 52-56.

120. T. A. Birks, J. C. Knight, and P. S. J. Russell, "Endlessly Single-Mode Photonic Crystal Fiber". Opt. Lett. 1997. 22(13): 961-963.

121. H. Inan, M. Poyraz, F. Inci, M. A. Lifson, M. Baday, B. T. Cunningham, and U. Demirci, "Photonic Crystals: Emerging Biosensors and Their Promise for Point-of-Care Applications". Chem. Soc. Rev. 2017. 46(2): 366-388.

122. N. L. Smith, Z. Hong, and S. A. Asher, "Responsive Ionic Liquid-Polymer 2D Photonic Crystal Gas Sensors". Analyst. 2014. 139: 6379-6386.

123. M. De Graef and M. E. McHenry, *Structure of Materials: An Introduction to Crystallography, Diffraction, and Symmetry*. New York: Cambridge University Press, 2007.

124. A. Tikhonov, R. D. Coalson, and S. A. Asher, "Light Diffraction from Colloidal Crystals with Low Dielectric Constant Modulation: Simulations Using Single-Scattering Theory". Physical review. B, Condensed matter and materials physics. 2008. 77(23): 235404.

125. W. L. Bragg, "The Diffraction of Short Electromagnetic Waves by a Crystal". Proc. Cambridge Philos. Soc. 1913. 17(43): 43-58.

126. S. A. Asher, J. M. Weissman, A. Tikhonov, R. D. Coalson, and R. Kesavamoorthy, "Diffraction in Crystalline Colloidal-Array Photonic Crystals". Phys. Rev. E. 2004. 69(6): 1-14.

127. C. Kittel, *Introduction to Solid State Physics*. New York: John Wiley and Sons, 1996.

128. A. G. Marshall and J. C. Oxley, "The Detection Problem", In: A. G. Marshall and J. C. Oxley (eds) *Aspects of Explosive Detection*. Oxford: Elsevier, 2009. pp. 1-10.

129. K. G. Furton and L. J. Myers, "The Scientific Foundation and Efficacy of the Use of Canines as Chemical Detectors for Explosives". Talanta. 2001. 54(3): 487-500.

130. J. C. Oxley and L. P. Waggoner, "Detection of Explosives by Dogs", In: A. G. Marshall and J. C. Oxley (eds) *Aspects of Explosive Detection*. Oxford: Elsevier, 2009. pp. 27-40.

131. K. J. Garner, L. Busbee, P. Cornwell, J. Edmonds, K. Mullins, K. Rader, J. Johnston, and J. Williams, Eds., *Duty Cycle of the Detector Dog: A Baseline Study* (Institute for Biological Detection Systems, Auburn University, 2001).

132. I. Gazit and J. Terkel, "Explosives Detection by Sniffer Dogs Following Strenuous Physical Activity". Applied Animal Behaviour Science. 2003. 81(2): 149-161.

133. L. Lit, J. Schweitzer, and A. Oberbauer, "Handler Beliefs Affect Scent Detection Dog Outcomes". Anim. Cogn. 2011. 14(3): 387-394.

134. J. Yinon, "Peer Reviewed: Detection of Explosives by Electronic Noses". Anal. Chem. 2003. 75(5): 98-105.

135. D. S. Moore, "Instrumentation for Trace Detection of High Explosives". Rev. Sci. Instrum. 2004. 75(8): 2499-2512.

136. R. J. Harper and K. G. Furton, "Biological Detection of Explosives", In: J. Yinon (ed) *Counterterrorist Detection Techniques of Explosives*. Oxford: Elsevier, 2007. pp. 395-432.

137. R. G. Ewing and C. J. Miller, "Detection of Volatile Vapors Emitted from Explosives with a Handheld Ion Mobility Spectrometer". Field Anal. Chem. Technol. 2001. 5(5): 215-221.

138. R. G. Ewing, D. A. Atkinson, G. A. Eiceman, and G. J. Ewing, "A Critical Review of Ion Mobility Spectrometry for the Detection of Explosives and Explosive Related Compounds". Talanta. 2001. 54(3): 515-529.

139. G. A. Eiceman, Z. Karpas, and H. H. Hill Jr, *Ion Mobility Spectrometry*. Boca Raton: CRC press, 2013.

140. H. Borsdorf, T. Mayer, M. Zarejousheghani, and G. A. Eiceman, "Recent Developments in Ion Mobility Spectrometry". Appl. Spectrosc. Rev. 2011. 46(6): 472-521.

141. G. Eiceman, "Ion-Mobility Spectrometry as a Fast Monitor of Chemical Composition". TrAC, Trends Anal. Chem. 2002. 21(4): 259-275.

142. D. Collins and M. Lee, "Developments in Ion Mobility Spectrometry–Mass Spectrometry". Anal. Bioanal. Chem. 2002. 372(1): 66-73.

143. J. S. Caygill, F. Davis, and S. P. J. Higson, "Current Trends in Explosive Detection Techniques". Talanta. 2012. 88(0): 14-29.

144. G. Eiceman and J. Stone, "Peer Reviewed: Ion Mobility Spectrometers in National Defense". Anal. Chem. 2004. 76(21): 390-397.

145. C. K. Hilton, C. A. Krueger, A. J. Midey, M. Osgood, J. Wu, and C. Wu, "Improved Analysis of Explosives Samples with Electrospray Ionization-High Resolution Ion Mobility Spectrometry (ESI-HRIMS)". Int. J. Mass spectrom. 2010. 298(1): 64-71.

146. M. E. Germain and M. J. Knapp, "Optical Explosives Detection: From Color Changes to Fluorescence Turn-on". Chem. Soc. Rev. 2009. 38(9): 2543-2555.

147. S. J. Toal and W. C. Trogler, "Polymer Sensors for Nitroaromatic Explosives Detection". J. Mater. Chem. 2006. 16(28): 2871-2883.

148. J. Almog and S. Zitrin, "Colorimetric Detection of Explosives", In: A. G. Marshall and J. C. Oxley (eds) *Aspects of Explosive Detection*. Oxford: Elsevier, 2009. pp. 41-58.

149. V. K. Pamula, V. Srinivasan, H. Chakrapani, R. B. Fair, and E. J. Toone, "A Droplet-Based Lab-on-a-chip for Colorimetric Detection of Nitroaromatic Explosives", in *Micro Electro Mechanical Systems, 2005. MEMS 2005. 18th IEEE International Conference* (IEEE, 2005), p. 722-725.

150. K. L. Bjella, "Pre-Screening for Explosives Residues in Soil Prior to HPLC Analysis Utilizing Expray". Cold Regions Research and Engineering Laboratory ERDC/CRREL TN-05-2. 2005.

151. Q. Zhou and T. M. Swager, "Method for Enhancing the Sensitivity of Fluorescent Chemosensors: Energy Migration in Conjugated Polymers". JACS. 1995. 117(26): 7017-7018.

152. Q. Zhou and T. M. Swager, "Fluorescent Chemosensors Based on Energy Migration in Conjugated Polymers: The Molecular Wire Approach to Increased Sensitivity". JACS. 1995. 117(50): 12593-12602.

153. T. M. Swager, "The Molecular Wire Approach to Sensory Signal Amplification". Acc. Chem. Res. 1998. 31(5): 201-207.

154. T. Naddo, Y. Che, W. Zhang, K. Balakrishnan, X. Yang, M. Yen, J. Zhao, J. S. Moore, and L. Zang, "Detection of Explosives with a Fluorescent Nanofibril Film". JACS. 2007. 129(22): 6978-6979.

155. Y. Liu, R. C. Mills, J. M. Boncella, and K. S. Schanze, "Fluorescent Polyacetylene Thin Film Sensor for Nitroaromatics". Langmuir. 2001. 17(24): 7452-7455.

156. C.-P. Chang, C.-Y. Chao, J. H. Huang, A.-K. Li, C.-S. Hsu, M.-S. Lin, B. R. Hsieh, and A.-C. Su, "Fluorescent Conjugated Polymer Films as TNT Chemosensors". Synth. Met. 2004. 144(3): 297-301.

157. J.-S. Yang and T. M. Swager, "Porous Shape Persistent Fluorescent Polymer Films: An Approach to TNT Sensory Materials". JACS. 1998. 120(21): 5321-5322.

158. T. M. Swager and J. H. Wosnick, "Self-Amplifying Semiconducting Polymers for Chemical Sensors". MRS Bull. 2002. 27(6): 446-450.

159. T. L. Andrew and T. M. Swager, "A Fluorescence Turn-On Mechanism to Detect High Explosives RDX and PETN". JACS. 2007. 129(23): 7254-7255.

160. M. E. Germain and M. J. Knapp, "Turn-on Fluorescence Detection of H_2O_2 and TATP". Inorg. Chem. 2008. 47(21): 9748-9750.

161. Y. Xia, L. Song, and C. Zhu, "Turn-On and Near-Infrared Fluorescent Sensing for 2,4,6-Trinitrotoluene Based on Hybrid (Gold Nanorod)−(Quantum Dots) Assembly". Anal. Chem. 2011. 83(4): 1401-1407.

162. Z. Takáts, I. Cotte-Rodriguez, N. Talaty, H. Chen, and R. G. Cooks, "Direct, Trace Level Detection of Explosives on Ambient Surfaces by Desorption Electrospray Ionization Mass Spectrometry". Chem. Commun. 2005. (15): 1950-1952.

163. N. Na, C. Zhang, M. Zhao, S. Zhang, C. Yang, X. Fang, and X. Zhang, "Direct Detection of Explosives on Solid Surfaces by Mass Spectrometry with an Ambient Ion Source Based on Dielectric Barrier Discharge". J. Mass Spectrom. 2007. 42(8): 1079-1085.

164. D. R. Justes, N. Talaty, I. Cotte-Rodriguez, and R. G. Cooks, "Detection of Explosives on Skin Using Ambient Ionization Mass Spectrometry". Chem. Commun. 2007. (21): 2142-2144.

165. A. Buffler, "Contraband Detection with Fast Neutrons". Radiat. Phys. Chem. 2004. 71(3): 853-861.

166. R. F. Eilbert, "X-Ray Technologies", In: A. G. Marshall and J. C. Oxley (eds) *Aspects of Explosive Detection*. Oxford: Elsevier, 2009. pp. 89-130.

167. S. K. Sharma, P. G. Lucey, M. Ghosh, H. W. Hubble, and K. A. Horton, "Stand-off Raman Spectroscopic Detection of Minerals on Planetary Surfaces". Spectrochim. Acta, Part A. 2003. 59(10): 2391-2407.

168. F. J. Fortes and J. J. Laserna, "The Development of Fieldable Laser-Induced Breakdown Spectrometer: No Limits on the Horizon". Spectrochim. Acta B. 2010. 65(12): 975-990.

169. G. Steiner, "Infrared and Raman Spectroscopic Imaging", In: R. Salzer (ed) *Biomedical Imaging: Principles and Applications*. Hoboken: John Wiley & Sons, 2010. 9, pp. 275-303.

170. K. T. Hufziger, S. V. Bykov, and S. A. Asher, "Raman Hyperspectral Imaging Spectrometer Utilizing Crystalline Colloidal Array Photonic Crystal Diffraction". Appl. Spectrosc. 2014. 68(11): 1219-1223.

171. C. Lopez-Moreno, S. Palanco, J. J. Laserna, F. C. De Lucia, A. W. Miziolek, J. Rose, R. A. Walters, and A. I. Whitehouse, "Test of a Stand-off Laser-Induced Breakdown Spectroscopy Sensor for the Detection of Explosive Residues on Solid Surfaces". J. Anal. At. Spectrom. 2006. 21(1): 55-60.

172. J. J. Brady, S. D. Roberson, M. E. Farrell, E. L. Holthoff, D. N. Stratis-Cullum, and P. M. Pellegrino, "Laser-Induced Breakdown Spectroscopy: A Review of Applied Explosive Detection". Army Research Laboratory ARL-TR-6649. 2013.

173. J. L. Gottfried, F. C. De Lucia Jr, C. A. Munson, and A. W. Miziolek, "Laser-Induced Breakdown Spectroscopy for Detection of Explosives Residues: A Review of Recent Advances, Challenges, and Future Prospects". Anal. Bioanal. Chem. 2009. 395(2): 283-300.

174. D. W. Hahn and N. Omenetto, "Laser-Induced Breakdown Spectroscopy (LIBS), Part I: Review of Basic Diagnostics and Plasma–Particle Interactions: Still-Challenging Issues Within the Analytical Plasma Community". Appl. Spectrosc. 2010. 64(12): 335-366.

175. D. W. Hahn and N. Omenetto, "Laser-Induced Breakdown Spectroscopy (LIBS), Part II: Review of Instrumental and Methodological Approaches to Material Analysis and Applications to Different Fields". Appl. Spectrosc. 2012. 66(4): 347-419.

176. J. L. Gottfried, F. C. De Lucia, C. A. Munson, and A. W. Miziolek, "Strategies for Residue Explosives Detection Using Laser-Induced Breakdown Spectroscopy". J. Anal. At. Spectrom. 2008. 23(2): 205-216.

177. J. L. Gottfried and F. C. De Lucia, "Laser-Induced Breakdown Spectroscopy for the Standoff Detection of Explosive Residues", in *Imaging and Applied Optics Technical Papers* (Optical Society of America Technical Digest, 2012).

178. J. L. Gottfried, "Influence of Metal Substrates on the Detection of Explosive Residues with Laser-Induced Breakdown Spectroscopy". Appl. Opt. 2013. 52(4): 10-19.

179. P. Lucena, I. Gaona, J. Moros, and J. J. Laserna, "Location and Detection of Explosive-Contaminated Human Fingerprints on Distant Targets Using Standoff Laser-Induced Breakdown Spectroscopy". Spectrochim. Acta B. 2013. 85: 71-77.

180. R. González, P. Lucena, L. Tobaria, and J. Laserna, "Standoff LIBS Detection of Explosive Residues Behind a Barrier". J. Anal. At. Spectrom. 2009. 24(8): 1123-1126.

181. J. Moros, J. Lorenzo, and J. Laserna, "Standoff Detection of Explosives: Critical Comparison for Ensuing Options on Raman Spectroscopy–LIBS Sensor Fusion". Anal. Bioanal. Chem. 2011. 400(10): 3353-3365.

182. S. Angel, T. J. Kulp, and T. M. Vess, "Remote-Raman Spectroscopy at Intermediate Ranges Using Low-Power CW Lasers". Appl. Spectrosc. 1992. 46(7): 1085-1091.

183. S. K. Sharma, A. K. Misra, and B. Sharma, "Portable Remote Raman System for Monitoring Hydrocarbon, Gas Hydrates and Explosives in the Environment". Spectrochim. Acta, Part A. 2005. 61(10): 2404-2412.

184. A. Pettersson, I. Johansson, S. Wallin, M. Nordberg, and H. Östmark, "Near Real-Time Standoff Detection of Explosives in a Realistic Outdoor Environment at 55 m Distance". Propell. Explos. Pyrot. 2009. 34(4): 297-306.

185. B. Zachhuber, C. Gasser, E. T. H. Chrysostom, and B. Lendl, "Stand-off Spatial Offset Raman Spectroscopy for the Detection of Concealed Content in Distant Objects". Anal. Chem. 2011. 83(24): 9438-9442.

186. P. Matousek, I. Clark, E. Draper, M. Morris, A. Goodship, N. Everall, M. Towrie, W. Finney, and A. Parker, "Subsurface Probing in Diffusely Scattering Media Using Spatially Offset Raman Spectroscopy". Appl. Spectrosc. 2005. 59(4): 393-400.

187. B. Zachhuber, H. Östmark, and T. Carlsson, "Spatially Offset Hyperspectral Stand-off Raman Imaging for Explosive Detection Inside Containers". Proc. SPIE 9073, Chemical, Biological, Radiological, Nuclear, and Explosives (CBRNE) Sensing XV. 2014. pp. 90730-90735.

188. S. A. Asher and C. Johnson, "Raman Spectroscopy of a Coal Liquid Shows that Fluorescence Interference is Minimized with Ultraviolet Excitation". Science. 1984. 225(4659): 311.

189. J. A. Carroll, E. L. Izake, B. Cletus, and E. Jaatinen, "Eye-Safe UV Stand-off Raman Spectroscopy for the Ranged Detection of Explosives in the Field". J. Raman Spectrosc. 2015. 46(3): 333-338.

190. R. Bhartia, W. F. Hug, and R. D. Reid, "Improved Sensing Using Simultaneous Deep UV Raman and Fluorescence Detection". Proc. SPIE 8358, Chemical, Biological, Radiological, Nuclear, and Explosives (CBRNE) Sensing XIII. 2012. 8358: pp. 1-9.

191. W. F. Hug, R. Bhartia, K. Sijapati, L. Beegle, and R. Reid, "Improved Sensing Using Simultaneous Deep-UV Raman and Fluorescence Detection-II". Proc. SPIE 9073, Chemical, Biological, Radiological, Nuclear, and Explosives (CBRNE) Sensing XV. 2014. pp. 1-11.

192. R. Bhartia, W. F. Hug, R. D. Reid, and L. W. Beegle, "Explosives Detection and Analysis by Fusing Deep Ultraviolet Native Fluorescence and Resonance Raman Spectroscopy", In: K. Iniewski (ed) *Laser-Based Optical Detection of Explosives*. Boca Raton: Taylor & Francis, 2015. 4, pp. 67-98.

193. R. Waterbury, J. Rose, D. Vunck, T. Blank, K. Pohl, A. Ford, T. McVay, and E. Dottery, "Fabrication and Testing of a Standoff Trace Explosives Detection System". Proc. SPIE 8018 Chemical, Biological, Radiological, Nuclear, and Explosives (CBRNE) Sensing XIII. 2011. 8018: 1-6.

194. A. Ehlerding, I. Johansson, S. Wallin, and H. Östmark, "Resonance-Enhanced Raman Spectroscopy on Explosives Vapor at Standoff Distances". Int. J. Spectrosc. 2012. 2012: 1-9.

195. T. A. Reichardt, S. E. Bisson, and T. J. Kulp, "Standoff Ultraviolet Raman Scattering Detection of Trace Levels of Explosives". Sandia National Labs SAND2011-7955. 2011. 7955: 1-27.

196. S. V. Bykov, B. Sharma, and S. A. Asher, "High-Throughput, High-Resolution Echelle Deep-UV Raman Spectrometer". Appl. Spectrosc. 2013. 67(8): 873-883.

197. S. V. Bykov, M. Mao, K. L. Gares, and S. A. Asher, "Compact Solid-State 213 nm Laser Enables Standoff Deep Ultraviolet Raman Spectrometer: Measurements of Nitrate Photochemistry". Appl. Spectrosc. 2015. 69(8): 895-901.

198. S. V. Bykov, I. Lednev, A. Ianoul, A. Mikhonin, C. Munro, and S. A. Asher, "Steady-State and Transient Ultraviolet Resonance Raman Spectrometer for the 193-270 nm Spectral Region". Appl. Spectrosc. 2005. 59(12): 1541-1552.

199. S. Schlücker, M. D. Schaeberle, S. W. Huffman, and I. W. Levin, "Raman Microspectroscopy: A Comparison of Point, Line, and Wide-Field Imaging Methodologies". Anal. Chem. 2003. 75(16): 4312-4318.

200. S. E. Bohndiek, A. Wagadarikar, C. L. Zavaleta, D. Van de Sompel, E. Garai, J. V. Jokerst, S. Yazdanfar, and S. S. Gambhir, "A Small Animal Raman Instrument for Rapid, Wide-Area, Spectroscopic Imaging". Proc. Natl. Acad. Sci. U. S. A. 2013. 110(30): 12408.

201. M. Nelson, P. Treado, and R. Priore. Spatially and Spectrally Parallelized Fiber Array Spectral Translator System and Method of Use. US8098373B2. Filed 2010. Issued 2010.

202. J. Ma and D. Ben-Amotz, "Rapid Micro-Raman Imaging Using Fiber-Bundle Image Compression". Appl. Spectrosc. 1997. 51(12): 1845-1848.

203. S. A. Asher, L. Wang, and D. Tuschel. Crystalline Colloidal Array Deep UV Narrow Band Radiation Filter. US2012/0062883 A1. Filed 2011.

204. J. M. Amigo, "Practical Issues of Hyperspectral Imaging Analysis of Solid Dosage Forms". Anal. Bioanal. Chem. 2010. 398(1): 93-109.

205. C.-I. Chang, *Hyperspectral Imaging : Techniques for Spectral Detection and Classification*. New York: Kluwer Academic/Plenum, 2003. 1-16.

206. Y. Roggo, A. Edmond, P. Chalus, and M. Ulmschneider, "Infrared Hyperspectral Imaging for Qualitative Analysis of Pharmaceutical Solid Forms". Anal. Chim. Acta. 2005. 535(1): 79-87.

207. P. M. Mehl, Y.-R. Chen, M. S. Kim, and D. E. Chan, "Development of Hyperspectral Imaging Technique for the Detection of Apple Surface Defects and Contaminations". J. Food Eng. 2004. 61(1): 67-81.

208. H. Huang, L. Liu, M. O. Ngadi, C. Gariépy, and S. O. Prasher, "Near-Infrared Spectral Image Analysis of Pork Marbling Based on Gabor Filter and Wide Line Detector Techniques". Appl. Spectrosc. 2014. 68(3): 332-339.

209. R. O. Green, M. L. Eastwood, C. M. Sarture, T. G. Chrien, M. Aronsson, B. J. Chippendale, J. A. Faust, B. E. Pavri, C. J. Chovit, M. Solis, M. R. Olah, and O. Williams, "Imaging Spectroscopy and the Airborne Visible/Infrared Imaging Spectrometer (AVIRIS)". Remote Sens. Environ. 1998. 65(3): 227-248.

210. M. T. Bremer, P. J. Wrzesinski, N. Butcher, V. V. Lozovoy, and M. Dantus, "Highly Selective Standoff Detection and Imaging of Trace Chemicals in a Complex Background Using Single-beam Coherent Anti-Stokes Raman Scattering". Appl. Phys. Lett. 2011. 99(10): 1-3.

211. B. Guo, Y. Wang, C. Peng, H. Zhang, G. Luo, H. Le, C. Gmachl, D. Sivco, M. Peabody, and A. Cho, "Laser-Based Mid-Infrared Reflectance Imaging of Biological Tissues". Opt. Express. 2004. 12(1): 208-219.

212. F. Pinaud, X. Michalet, L. A. Bentolila, J. M. Tsay, S. Doose, J. J. Li, G. Iyer, and S. Weiss, "Advances in Fluorescence Imaging with Quantum Dot Bio-probes". Biomaterials. 2006. 27(9): 1679-1687.

213. L. H. Kidder, V. F. Kalasinsky, J. L. Luke, I. W. Levin, and E. N. Lewis, "Visualization of Silicone Gel in Human Breast Tissue Using New Infrared Imaging Spectroscopy". Nat. Med. (N. Y., NY, U. S.). 1997. 3(2): 235-237.

214. S. Keren, C. Zavaleta, Z. Cheng, A. de la Zerda, O. Gheysens, and S. S. Gambhir, "Noninvasive Molecular Imaging of Small Living Subjects Using Raman Spectroscopy". Proc. Natl. Acad. Sci. U. S. A. 2008. 105(15): 5844-5849.

215. C. Krafft, T. Knetschke, A. Siegner, R. H. W. Funk, and R. Salzer, "Mapping of Single Cells by Near Infrared Raman Microspectroscopy". Vib. Spectrosc. 2003. 32(1): 75-83.

216. K. A. Christensen, N. L. Bradley, M. D. Morris, and R. V. Morrison, "Raman Imaging Using a Tunable Dual-Stage Liquid Crystal Fabry-Perot Interferometer". Appl. Spectrosc. 1995. 49(8): 1120-1125.

217. S. A. Asher. Crystalline Colloidal Narrow Band Radiation Filter. US4632517. Filed 1984. Issued 1986.

218. S. A. Asher, G. Haacke, L. G. Magliocco, and H. P. Panzer. Narrow Band Radiation Filter Films. US5266238. Filed 1990. Issued 1993.

219. L. Giovanni and H. P. Panzer. Narrow Band Radiation Filter Films. US5330685. Filed 1991. Issued 1994.

220. S.-H. Kim, H. S. Park, J. H. Choi, J. W. Shim, and S.-M. Yang, "Integration of Colloidal Photonic Crystals toward Miniaturized Spectrometers". Adv. Mater. 2010. 22(9): 946-950.

221. H. Ding, C. Liu, H. Gu, Y. Zhao, B. Wang, and Z. Gu, "Responsive Colloidal Crystal for Spectrometer Grating". ACS Photonics. 2014. 1(2): 121-126.

222. M. M. Ward Muscatello, L. E. Stunja, and S. A. Asher, "Polymerized Crystalline Colloidal Array Sensing of High Glucose Concentrations". Anal. Chem. 2009. 81(12): 4978-4986.

223. H. J. Van Den Hul and J. W. Vanderhoff, "The Characterization of Latex Particle Surfaces by Ion Exchange and Conductometric Titration". J. Electroanal. Chem. Interfacial Electrochem. 1972. 37(1): 161-182.

224. L. Liu, P. Li, and S. A. Asher, "Fortuitously Superimposed Lattice Plane Secondary Diffraction from Crystalline Colloidal Arrays". JACS. 1997. 119(11): 2729-2732.

225. C. Kittel, *Introduction to Solid State Physics*. New York: John Wiley and Sons, 1971. 1-76.

226. R. J. Carlson and S. A. Asher, "Characterization of Optical Diffraction and Crystal Structure in Monodisperse Polystyrene Colloids". Appl. Spectrosc. 1984. 38(3): 297-304.

227. G. Pan, A. K. Sood, and S. A. Asher, "Polarization Dependence of Crystalline Colloidal Array Diffraction". J. Appl. Phys. 1998. 84(1): 83-86.

228. R. J. Spry and D. J. Kosan, "Theoretical Analysis of the Crystalline Colloidal Array Filter". Appl. Spectrosc. 1986. 40(6): 782-784.

229. K. L. Gares, K. T. Hufziger, S. V. Bykov, and S. A. Asher, "Review of Explosive Detection Methodologies and the Emergence of Standoff Deep UV Resonance Raman". J. Raman Spectrosc. 2016. 47(1): 124-141.

230. H. Östmark, S. Wallin, and H. G. Ang, "Vapor Pressure of Explosives: A Critical Review". Propell. Explos. Pyrot. 2012. 37(1): 12-23.

231. T. L. Andrew and T. M. Swager, "Detection of Explosives via Photolytic Cleavage of Nitroesters and Nitramines". J. Org. Chem. 2011. 76(9): 2976-2993.

232. R. R. Kunz, K. E. Gregory, M. J. Aernecke, M. L. Clark, A. Ostrinskaya, and A. W. Fountain, "Fate Dynamics of Environmentally Exposed Explosive Traces". J. Phys. Chem. A. 2012. 116(14): 3611-3624.

233. S. A. Asher, "UV Resonance Raman Spectroscopy for Analytical, Physical, and Biophysical Chemistry Part 2". Anal. Chem. 1993. 65(4): 201A-210A.

234. Y. Kumamoto, A. Taguchi, N. I. Smith, and S. Kawata, "Deep Ultraviolet Resonant Raman Imaging of a Cell". J. Biomed. Opt. 2012. 17(7): 0760011-0760014.

235. S. A. Asher. Crystalline Colloidal Narrow Band Radiation Filter. US4627689. Filed 1983. Issued 1986.

236. S. A. Asher, J. Holtz, L. Liu, and Z. Wu, "Self-Assembly Motif for Creating Submicron Periodic Materials. Polymerized Crystalline Colloidal Arrays". JACS. 1994. 116(11): 4997-4998.

237. M. Ben-Moshe, V. L. Alexeev, and S. A. Asher, "Fast Responsive Crystalline Colloidal Array Photonic Crystal Glucose Sensors". Anal. Chem. 2006. 78(14): 5149-5157.

238. J.-T. Zhang, Z. Cai, D. H. Kwak, X. Liu, and S. A. Asher, "Two-Dimensional Photonic Crystal Sensors for Visual Detection of Lectin Concanavalin A". Anal. Chem. 2014. 86(18): 9036-9041.

239. Z. Cai, D. H. Kwak, D. Punihaole, Z. Hong, S. S. Velankar, X. Liu, and S. A. Asher, "A Photonic Crystal Protein Hydrogel Sensor for Candida Albicans". Angew. Chem. Int. Ed. 2015. 54(44): 13036-13040.

240. B. Zachhuber, G. Ramer, A. Hobro, and B. Lendl, "Stand-off Raman Spectroscopy: A Powerful Technique for Qualitative and Quantitative Analysis of Inorganic and Organic Compounds Including Explosives". Anal. Bioanal. Chem. 2011. 400(8): 2439-2447.

241. A. J. Hopkins, J. L. Cooper, L. T. M. Profeta, and A. R. Ford, "Portable Deep-Ultraviolet (DUV) Raman for Standoff Detection". Appl. Spectrosc. 2016. 70(5): 861-873.

242. American National Standards Institute, "American National Standard for Safe Use of Lasers", ANSI Z136.1, Laser Institute of America, Orlando, FL, 2014.

243. NIH, ImageJ, https://imagej.nih.gov/ij/index.html [accessed August 2016]

244. S. A. Asher, R. W. Bormett, X. Chen, D. H. Lemmon, N. Cho, P. Peterson, M. Arrigoni, L. Spinelli, and J. Cannon, "UV Resonance Raman Spectroscopy Using a New CW Laser Source: Convenience and Experimental Simplicity". Appl. Spectrosc. 1993. 47(5): 628-633.

245. G. Gillen and J. R. Verkouteren, "Standards for Standoff Optical-Based Explosives Detection", In: K. Iniewski (ed) *Laser-Based Optical Detection of Explosives*. Boca Raton: Taylor & Francis, 2015. pp. 41-63.

246. E. L. Holthoff, M. E. Farrell, and P. M. Pellegrino, "Standardized Sample Preparation Using a Drop-on-Demand Printing Platform". Sensors. 2013. 13(5): 5814-5825.

247. S. A. Asher, C. R. Johnson, and J. Murtaugh, "Development of a new UV resonance Raman spectrometer for the 217–400-nm spectral region". Rev. Sci. Instrum. 1983. 54(12): 1657-1662.

248. I. H. Malitson, "Interspecimen Comparison of the Refractive Index of Fused Silica". J. Opt. Soc. Am. 1965. 55(10): 1205-1209.

249. M. Daimon and A. Masumura, "Measurement of the Refractive Index of Distilled Water from the Near-Infrared Region to the Ultraviolet Region". Appl. Opt. 2007. 46(18): 3811-3820.

250. W. H. Zachariasen, *Theory of X-ray Diffraction in Crystals*. London: John Wiley, 1945.

251. P. A. Rundquist, S. Jagannathan, R. Kesavamoorthy, C. Brnardic, S. Xu, and S. A. Asher, "Photothermal Compression of Colloidal Crystals". J. Chem. Phys. 1991. 94(1): 711-717.

252. R. Kesavamoorthy, S. Jagannathan, P. A. Rundquist, and S. A. Asher, "Colloidal Crystal Photothermal Dynamics". J. Chem. Phys. 1991. 94(7): 5172-5179.

253. Z. Hong and S. A. Asher, "Dependence of Raman and Resonance Raman Intensities on Sample Self-Absorption". Appl. Spectrosc. 2015. 69(1): 75-83.

254. Y. A. Gruzdkov and Y. M. Gupta, "Vibrational Properties and Structure of Pentaerythritol Tetranitrate". J. Phys. Chem. A. 2001. 105(25): 6197-6202.

255. W. Perger, J. Zhao, J. Winey, and Y. Gupta, "First-Principles Study of Pentaerythritol Tetranitrate Single Crystals Under High Pressure: Vibrational Properties". Chem. Phys. Lett. 2006. 428(4): 394-399.

256. H. Tang and B. Torrie, "Raman Study of NH_4NO_3 and ND_4NO_3-250-420K". J. Phys. Chem. Solids. 1977. 38(2): 125-138.

257. M. R. Waterland, D. Stockwell, and A. M. Kelley, "Symmetry Breaking Effects in NO_3^-: Raman Spectra of Nitrate Salts and ab initio Resonance Raman Spectra of Nitrate–Water Complexes". J. Chem. Phys. 2001. 114(14): 6249-6258.

258. J. M. Lightstone, T. B. Onasch, D. Imre, and S. Oatis, "Deliquescence, Efflorescence, and Water Activity in Ammonium Nitrate and Mixed Ammonium Nitrate/Succinic Acid Microparticles". J. Phys. Chem. A. 2000. 104(41): 9337-9346.

259. C. Rodriguez-Nevarro and E. Doehne, "Salt Weathering: Influence of Evaporation Rate, Supersaturation and Crystallization Pattern". Earth Surf. Proc. Land. 1999. 24: 191-209.

260. W. J. P. van Enckevort and J. H. Los, "On the Creeping of Saturated Salt Solutions". Cryst. Growth Des. 2013. 13(5): 1838-1848.

261. K. T. Hufziger, S. Bykov, and S. A. Asher, "Ultraviolet Raman Wide-field Hyperspectral Imaging Spectrometer for Standoff Trace Explosive Detection". Appl. Spectrosc. 2017. 71(2): 173-185.

262. S. A. Asher, K. W. Kimble, and J. P. Walker, "Enabling Thermoreversible Physically Cross-Linked Polymerized Colloidal Array Photonic Crystals". Chem. Mater. 2008. 20(24): 7501-7509.

263. J. Wang, J. Liang, H. Wu, W. Yuan, Y. Wen, Y. Song, and L. Jiang, "A Facile Method of Shielding from UV Damage by Polymer Photonic Crystals". Polym. Int. 2008. 57(3): 509-514.

264. X. Ye and L. Qi, "Two-Dimensionally Patterned Nanostructures Based on Monolayer Colloidal Crystals: Controllable Fabrication, Assembly, and Applications". Nano Today. 2011. 6(6): 608-631.

265. J. J. Bohn, M. Ben-Moshe, A. Tikhonov, D. Qu, D. N. Lamont, and S. A. Asher, "Charge Stabilized Crystalline Colloidal Arrays as Templates for Fabrication of Non-close-packed Inverted Photonic Crystals". J. Colloid Interface Sci. 2010. 344(2): 298-307.

266. K. R. Phillips, N. Vogel, Y. Hu, M. Kolle, C. C. Perry, and J. Aizenberg, "Tunable Anisotropy in Inverse Opals and Emerging Optical Properties". Chem. Mater. 2014. 26(4): 1622-1628.

267. A. Stein, B. E. Wilson, and S. G. Rudisill, "Design and Functionality of Colloidal-Crystal-Templated Materials—Chemical Applications of Inverse Opals". Chem. Soc. Rev. 2013. 42(7): 2763-2803.

268. C. Li and L. Qi, "Bioinspired Fabrication of 3D Ordered Macroporous Single Crystals of Calcite from a Transient Amorphous Phase". Angew. Chem. Int. Ed. 2008. 47(13): 2388-2393.

269. L. Wang and X. Zhao, "Fabrication of Crack-Free Colloidal Crystals Using a Modified Vertical Deposition Method". J. Phys. Chem. C. 2007. 111(24): 8538-8542.

270. R. G. Shimmin, A. J. DiMauro, and P. V. Braun, "Slow Vertical Deposition of Colloidal Crystals: A Langmuir−Blodgett Process?". Langmuir. 2006. 22(15): 6507-6513.

271. N. Sultanova, S. Kasarova, and I. Nikolov, "Dispersion Properties of Optical Polymers". Acta Physica Polonica-Series A General Physics. 2009. 116(4): 585.

272. J. F. Bertone, P. Jiang, K. S. Hwang, D. M. Mittleman, and V. L. Colvin, "Thickness Dependence of the Optical Properties of Ordered Silica-air and Air-polymer Photonic Crystals". Phys. Rev. Lett. 1999. 83(2): 300.

273. C. A. Palmer and E. G. Loewen, *Diffraction Grating Handbook*. Newport Corporation, 2005.

274. M. Abkarian, J. Nunes, and H. A. Stone, "Colloidal Crystallization and Banding in a Cylindrical Geometry". JACS. 2004. 126(19): 5978-5979.

275. S. Watanabe, K. Inukai, S. Mizuta, and M. T. Miyahara, "Mechanism for Stripe Pattern Formation on Hydrophilic Surfaces by Using Convective Self-Assembly". Langmuir. 2009. 25(13): 7287-7295.

276. G. Lozano and H. Míguez, "Growth Dynamics of Self-Assembled Colloidal Crystal Thin Films". Langmuir. 2007. 23(20): 9933-9938.